Title
Calcium channels and GABAA receptors shape action potential generation at the axon initial segment

Permalink
https://escholarship.org/uc/item/97v2q0dd

Author
Lipkin, Anna Marie

Publication Date
2023

Peer reviewed|Thesis/dissertation

Calcium channels and GABA-A receptors shape action potential generation at the axon initial segment

by
Anna Marie Lipkin

DISSERTATION
Submitted in partial satisfaction of the requirements for degree of
DOCTOR OF PHILOSOPHY

in

Neuroscience

in the

GRADUATE DIVISION
of the
UNIVERSITY OF CALIFORNIA, SAN FRANCISCO

Approved:

Dorit Ron
_____
8E86D47106E5485...
Dorit Ron
Chair

Kevin Bender
_____
Kevin Bender

AB Nelson
_____
Alexandra Nelson

Massimo Scanziani
_____
4AF406E430B7472...
Massimo Scanziani

_____
Committee Members

Dedication

To my parents, Rebecca and Seth, for showing me how to be thoughtful, careful, creative, and curious.

Acknowledgments

It is simply overwhelming to think of all the support I have received on the way to this point. Mentors, peers, and friends have shown me a generosity and gentleness throughout my PhD journey that has consistently surprised me, and to which I am deeply indebted. While a few words on a page cannot fully express my gratitude, I hope that they can serve as a record.

First and foremost, it was an honor to have Kevin Bender as my mentor and guide through graduate school. He has been the most welcoming, supportive, and motivating PI a PhD student could ask for. Always quick to praise, he never let me forget my value in the lab, in the program, and in science. Kevin is a wonderful role model: a careful and thoughtful scientist whose work is infused with an enthusiastic love of his subject matter. If I have a lab someday, I hope to emulate both his scientific rigor and his ability to build a lab environment shaped on mutual respect and joy.

My thesis committee has given me exceptional scientific and personal support over the past six years. From the beginning of my projects, Dorit Ron, Alexandra Nelson, and Massimo Scanziani have asked incisive questions that have shaped the direction of my research and my career. They have also provided emotional support during some of the most difficult moments of the journey. I hope their influence is apparent in the work that follows. I would also like to thank Roger Nicoll, who sat down with me for several hours when I asked him to serve on my qualifying exam committee. The questions he asked during that meeting have reverberated throughout my thesis work.

The Bender Lab, in its many iterations, has been a steadfast home to me during my PhD. Each member of the lab has profoundly shaped my development as a scientist. I'd like to thank the old guard, those who were in the lab when I joined: first the postdocs, Gina Rinetti-Vargas, without whose technical expertise, scientific curiosity, and generous teaching my project simply would not exist, and Roy Ben-Shalom, who made my brain tick with his complex neuron modeling projects and who provided much-needed encouragement during scary career steps. Next the graduate students: Becky Clarkson, Kenneth Burke Jr., Jiggy Geronimo, and Perry Spratt. These four imparted enormous amounts of wisdom to me,

Author Contributions

Chapter 1 was written by Anna Lipkin

Chapter 2 was reproduced in its entirety with permission from:

Lipkin, A. M., Cunniff, M.M., Spratt, P.W.E., Lemke, S.M., and Bender, K.J. (2021). Functional microstructure of Ca$_V$-mediated calcium signaling in the axon initial segment. Journal of Neuroscience 41, 3764-3776.

Conceptualization: AML, MMC, PWES, SLM, KJB. Data curation: AML, KJB. Formal Analysis: AML, KJB. Funding acquisition: AML, PWES, MMC, SLM, KJB. Investigation: AML, MMC, PWES, SLM, KJB. Methodology: AML, KJB. Software: AML, PWES, SLM, KJB. Supervision: KJB. Writing — original draft: AML. Writing — review & editing: AML, MMC, PWES, SLM, KJB.

Chapter 3 was written by Anna Lipkin, with sections reproduced with permission from:

Lipkin, A. M., Cunniff, M.M., Spratt, P.W.E., Lemke, S.M., and Bender, K.J. (2021). Functional microstructure of Ca$_V$-mediated calcium signaling in the axon initial segment. Journal of Neuroscience 41, 3764-3776.

and

Echevarria-Cooper, D. M., Hawkins, N.A., Misra, S.N., Huffman, A.M., Thaxton, T., Thompson, C.H., Ben-Shalom, R., Nelson, A.D., Lipkin, A.M., George, A.L., Bender, K.J., and Kearney, J.A. (2022). Cellular and behavioral effects of altered Na$_V$1.2 sodium channel ion permeability in *Scn2a*^{K1422E} mice. Human Molecular Genetics 00, 1-25.

Conceptualization: DMEC, ALG, AML, JAK, KJB. Data curation: AML, KJB. Formal Analysis: AML, KJB. Funding acquisition: KJB. Investigation: AML, CHT, KJB. Methodology: AML, KJB. Software: AML, PWES, SLM, KJB. Supervision: ALG, JAK, KJB.

Chapter 4 was written by Anna Lipkin.

Conceptualization: AML, KJB. Data curation: AML, KJB. Formal Analysis: AML, KJB. Funding acquisition: AML, KJB. Investigation: AML. Methodology: AML, KJB. Supervision: KJB.

Chapter 5 was written by Anna Lipkin.

Conceptualization: AML, Gina Rinetti-Vargas, KJB. Data curation: AML, KJB. Formal Analysis: AML, KJB. Funding acquisition: AML, KJB. Investigation: AML, Yann Ehinger, Zach Hoisington, Kimberly Derderian, KJB. Methodology: AML, KJB. Supervision: KJB.

Abstract

Calcium channels and GABA$_A$ receptors shape action potential generation at the

axon initial segment

Anna Marie Lipkin

The axon initial segment is a specialized region of most neurons where action potentials are initiated. The function of this compartment is derived from its dense collection of ion channels and scaffolding proteins, ranging from voltage-gated sodium channels and the ankyrin proteins that tether them to GABA receptors and the calcium stores that show tight colocalization with voltage-gated potassium channels. While careful work has illuminated how structure supports function in this complex compartment, several mysteries remain: (1) how are calcium channels organized at the axon initial segment, and how does this organization elucidate their function? and (2) how do chandelier cells, the GABAergic interneurons that exclusively and selectively target the axon initial segment, affect the function and output of their pyramidal neuron targets?

Here, using whole-cell patch-clamp electrophysiology, calcium imaging, and two-photon laser-scanning microscopy, I show that a mixture of calcium channels are found in the axon initial segment of layer 5 pyramidal neurons, where their differential organization hints at different functional roles. Additionally, I show that the complement of calcium channels present at the initial segment is a mixture of channels typically found in the dendrites or axon terminals exclusively. I go on to identify the mechanism by which chandelier cells inhibit pyramidal neuron output, despite a shift in the reversal potential of GABA that occurs in the middle of adolescent development that occurs only at the initial segment. These data support the idea that the axon initial segment is a specialized intermediate zone that incorporates properties of both somatodendritic and axonal regions.

Table of Contents

List of Figures

List of Tables

Chapter 1   Introduction

1.1   Structure and function of the axon initial segment

Neurons rely on a property called polarity for their function; that is, neurons have a top and a bottom. This polar organization reflects and shapes the physical separation integral to a neuron's function: inputs are received at the "top" of the neuron, the somatodendritic region, and outputs are sent from the "bottom," the axon. In between these two spatial and functional zones lies the boundary zone, the axon initial segment (Leterrier, 2018).

Physically, the axon initial segment is proposed to act as a barrier between the somatodendritic and axonal compartments, preventing cargo that doesn't belong in the axon from entering based on its dense meshwork of cytoskeletal elements (Hedstrom et al., 2008). The question of how cargo is recognized as axonal or somatodendritic is more complex than this, but the concept of the axon initial segment as a boundary or intermediate zone is an intriguing one. In my dissertation, I will show that the axon initial segment has a blend of calcium channels that would typically be found either in the dendrites or in the axon exclusively. Likewise, the development of inhibitory signaling onto the AIS, via the neurotransmitter GABA (γ-aminobutryic acid) released from AIS-targeting chandelier cells, shows an intermediate phenotype between that seen at the dendrite (always hyperpolarizing) and that at the distant axon terminals (always depolarizing). I will explore this concept, and its functional consequences, in this dissertation.

But beyond the physical role as intermediate zone, the axon initial segment plays an integral functional role in most neurons: that of action potential generation (Bender and Trussell, 2012). Action potentials are generated in two main cases: when synaptic input into the cell drives the membrane potential to threshold or when intrinsic conductances depolarize the membrane sufficiently to reach threshold, as in pacemaking cells (Bean, 2007). Briefly, membrane depolarization leads to the opening of voltage-gated sodium channels, typically in the AIS, which leads to a cascade effect of other voltage-gated sodium channels opening as the membrane rapidly depolarizes. These sodium channels quickly inactivate, which drives the

membrane potential downward. This downward deflection is aided by the activation of voltage-dependent potassium channels, which activate slightly more slowly than sodium channels. Together, sodium channel inactivation and potassium channel activation drive the membrane potential first to and then past the resting membrane potential before the AP, a feature known as the afterhyperpolarization. Calcium channels are also activated during an action potential, though they rarely drive the AP alone. Low voltage-activated calcium channels open around the same time as sodium channels, but the driving force on calcium is relatively low at this point. High voltage-activated calcium channels activate later, near the peak of the action potential, and the rapid repolarization of the membrane causes a massive increase in driving force, causing a rapid and transient influx of calcium into the membrane (McCobb and Beam, 1991). The duration of calcium influx during the action potential is exquisitely sensitive to the shape of the action potential: the peak voltage reached, the speed of the AP, and the duration of the repolarization phase can all affect peak calcium influx. While the general template of AP generation is well-established, nuances in the specific AIS channels that shape them creates a breathtaking diversity of AP shapes and powerfully expands the computational power of neurons and networks (Bean, 2007; Burke and Bender, 2019).

1.2   Ion channel scaffolding and organization at the axon initial segment

The organization of ion channels at the AIS is specified by a collection of cytoskeletal and scaffolding proteins and helps shape the function of this specialized neuronal compartment. The main ion channels involved in action potential generation, as described above, are voltage-gated sodium, calcium, and potassium channels. The high density of sodium channels anchored at the AIS, as well as their comparably low activation threshold, leads the AIS to be the site where membrane voltage first crosses the action potential threshold and generates a full-blown, all-or-nothing action potential. These voltage-gated sodium channels (Na_Vs) are stabilized in the AIS membrane by the scaffolding protein ankyrinG (AnkG), which also serves as the master regulator of the AIS (Davis and Bennett, 1994). Early in development, one class of Na_Vs, Na_V1.2, are expressed throughout the AIS and are solely responsible for AP generation in pyramidal neurons. Over time, however, lower-threshold Na_V1.6 channels begin to occupy the distal axonal

domain, adopting the role of AP generation while $Na_V1.2$ channels serve to backpropagate action potentials into the somatodendritic region (Hu et al., 2009; Spratt et al., 2019).

A variety of voltage-gated potassium channels (K_V) are expressed at the AIS, where they orchestrate AP repolarization, contribute to resting membrane potential regulation, and may perform non-conducting, scaffolding functions. K_V1 channels show differential distribution along the proximal vs distal AIS in some cell types, with higher expression at the distal region (Rowan et al., 2014; Van Wart et al., 2006). Here, their specific expression at the AIS but not the bouton controls AP duration locally (Kole et al., 2007; Rowan et al., 2014). K_V7 channels at the AIS regulate the resting membrane potential in the axon and may provide control over AP threshold (Hu and Bean, 2018; Martinello et al., 2015). These channels are very stable in the membrane, show an increase in density from the proximal to distal AIS, and, like Na_Vs, are anchored by AnkG (Battefeld et al., 2014; Benned-Jensen et al., 2016; Ogawa and Rasband, 2008). By contrast, while K_V2 channels appear to be present at the AIS, their function seems to differ dramatically from other K_V channels. Here as well as in the somatodendritic compartment, clusters of K_V2 channels perform a noncanonical role. Rather than conducting potassium ions, these clusters tether the plasma membrane to the endoplasmic reticulum and promote Ca_V clustering (King et al., 2014; Vierra et al., 2019).

The structural AIS domain defined by K_V2 clustering is also occupied by $GABA_A$ receptors and ryanodine receptors, but it lacks AnkG. This results in a patchwork across the AIS membrane: Na_V and K_V7 channels tethered by AnkG across a large portion of the AIS, with K_V2 channels, $GABA_A$ receptors, and cisternal organelles in the gaps in AnkG staining. The fine-scale organization of K_V, Na_V, and other AIS players has been well-established mostly through immunohistochemistry and other molecular approaches. However, these approaches have yielded far less information about the organization and even the presence of Ca_Vs in the AIS. Fortunately, electrophysiological approaches, combined with calcium imaging techniques, have led to an expanded understanding of which Ca_Vs are expressed in the AIS across different cell types. Low voltage-activated Ca_V3s are expressed most widely across neuron types and brain regions, contributing to AIS calcium influx in auditory brainstem, cerebellum, hippocampus, and cortex in rodent

and avian species (Bender and Trussell, 2009; Bender et al., 2012; Clarkson et al., 2017; Dumenieu et al., 2018; Fukaya et al., 2018; Hu and Bean, 2018; Jing et al., 2018; Martinello et al., 2015; Wang et al., 2016). In cortical neurons in particular, Ca_V3 channels are expressed alongside other channel classes, including Ca_V1 and Ca_V2 (Hanemaaijer et al., 2020; Yu et al., 2010). However, calcium imaging's poorer spatial resolution relative to immunohistochemistry has limited our understanding of how Ca_Vs fit into the fine-scale meshwork of ion channel organization at the AIS. In Chapter 2, I use a high-speed, high-resolution imaging technique combined with pharmacological tools to begin to answer this question.

1.3   Diversity and function of calcium channels: Theme and variations

Voltage-gated calcium channels form a remarkably diverse protein family, varying in their function, voltage-dependence, and localization in different tissues throughout the body. Even within a single neuron, different types of calcium channels achieve disparate functions by their localization in distinct neuronal compartments. Calcium channels are divided into two large classes based on their voltage-dependence of activation: low-voltage activated (LVA, encompassing Ca_V3 channels) and high-voltage activated channels (HVA, containing Ca_V1, $Ca_V2.1$, and $Ca_V2.2$). $Ca_V2.3$ channels, also known as R-type channels for their "residual" current under blockade are variably sorted into each category due to their intermediate voltage of activation (Sochivko et al., 2002). Structurally, each member of the Ca_V family follows a template similar to Na_V channels: an α subunit with six transmembrane segments form a pore domain and a voltage sensor (Catterall et al., 2005). As in sodium channels, the S4 domain is the voltage sensor. The S5 and S6 domain form the pore loop and determine ion selectivity for calcium. In fact, a single amino acid change in $Na_V1.2$ can make this sodium channel permeable to calcium (see Chapter 3). Ca_V1 and Ca_V2 are almost invariably associated with a β subunit, which can regulate the gating kinetics, sensitivity, and single-channel conductance of the channel as well as shaping the channel's localization within the cell (Arikkath and Campbell, 2003). The association of β subunits to different α subunits massively expands the functional diversity of HVA. Ca_V3 channels, by contrast, do not associate with any auxiliary subunits, prompting interesting questions about how its regulation may differ from HVAs (Simms and Zamponi, 2014).

Ca$_V$ channels were originally defined based on their physiology and pharmacological sensitivity. Accordingly, selective pharmacology has been the technical mainstay of understanding Ca$_V$ localization and function in the central nervous system. For example, Ca$_V$1 channels are defined by their selective antagonism to dihydropyridines like nifedipine and nimodipine. Ca$_V$1 channels require strong depolarization to activate and have long-lasting currents (Catterall et al., 2005). They are most commonly involved in muscle contraction, including via their direct activation of ryanodine receptors in the heart (Bers, 2002), as well as regulation of gene expression. While Ca$_V$2 channels also require strong depolarization to activate, they are insensitive to dihydropyridines but instead susceptible to blockade by peptide toxins like ω-conotoxins, agatoxin, and SNX-482 (Bourinet and Zamponi, 2017; McDonough et al., 1996; Newcomb et al., 1998). Ca$_V$2 channels underlie the calcium influx into axon terminals that triggers synaptic vesicle fusion and fast neurotransmitter release across brain regions (Catterall et al., 2005; Li et al., 2007). Ca$_V$3 channels differ from Ca$_V$2 and Ca$_V$1 not only by their need for only weak depolarization to activate, but also for the transient nature of the current they generate (Catterall et al., 2005). Functionally, these properties lead Ca$_V$3 channels to underlie low-threshold calcium spikes and bursts which often occur in dendrites following hyperpolarizing input and allow pacemaking activity in certain cell classes (Coulter et al., 1989; Ulrich and Huguenard, 1997). While Ca$_V$3 channels are commonly associated with dendritic localization, they are also capable of underlying burst generation when localized to the AIS (Bender and Trussell, 2009; Clarkson et al., 2017). Ca$_V$3 channels have been difficult to target pharmacologically, as antagonists for Ca$_V$3 channels often have some potency at other Ca$_V$s as well (Kraus et al., 2010; Zamponi et al., 1996). However, newly-developed antagonists TTA-A2 and TTA-P2 show much higher affinity for Ca$_V$3 over other Ca$_V$ channels and will expand our understanding of the localization and function of these channels (Kraus et al., 2010).

Voltage-gated calcium channels also perform the crucial function of translating changes in neuronal membrane potential into calcium influx, allowing calcium to act as a second messenger within the cell to initiate a wide variety of intracellular signaling cascades (Catterall, 2011). Because calcium is a ubiquitous signaling molecule but is needed to perform specific and often localized functions, the localization of Ca$_V$

channels shapes function through its proximity to downstream, calcium-senstive effectors. In the heart, the close proximity of Ca_V1 and ryanodine receptors enables excitation-contraction coupling (Bers, 2002). Ca_Vs are commonly found in close proximity to calcium-activated potassium channels in somatodendritic compartments, allowing for the regulation of EPSP amplitude and summation as well as AP dynamics and calcium influx (Bock and Stuart, 2016; Chen-Engerer et al., 2019; Irie and Trussell, 2017; Jones and Stuart, 2013; Wang et al., 2014). In axon terminals, similar spatial organization schemes affect neurotransmitter release, including but not limited to the modulation of short-term plasticity and release probability (Bucurenciu et al., 2008; Burke et al., 2018; Rebola et al., 2019; Scimemi and Diamond, 2012; Vyleta and Jonas, 2014). As with auxiliary subunits, tight spatial coupling of Ca_Vs to distinct calcium-sensitive signaling pathways massively expands the functional repertoire of calcium channels.

The concepts of the innate functional diversity of CaVs as well as the importance of understanding their spatial localization and signaling partners shaped the experiments detailed in Chapter 2 of this dissertation. Based on the identity of Ca_Vs present at the AIS of prefrontal pyramidal neurons, as well as their proximity to calcium-sensitive signaling molecules, we can begin to predict the functional consequences of each Ca_V's presence in this important structure.

1.4   AIS plasticity across timescales

The axon initial segment is a highly plastic structure, showing different forms of plasticity across a range of timescales and across a range of brain regions. Plasticity can occur very quickly, as in the case of K_V1 inactivation after subthreshold somatic depolarization (Kole et al., 2007), or over extended periods, like the plasticity that governs the tuning-frequency-dependent length of auditory brainstem neurons (Kuba et al., 2014). Because of the importance of the AIS in generating APs, plasticity changes in this structure can often be measured as changes in excitability ranging from threshold, AP shape, and downstream neurotransmitter release. In the shortest-term forms of plasticity, changes in the availability of ion channels like Na_V and K_V can alter AP shape and probability (Grubb et al., 2011; Hu et al., 2009; Kole et al., 2007). In the medium-term, modulatory input from dopaminergic and cholinergic input can alter the availability

of Ca_V3 and K_V7 channels, respectively, with consequences for AP bursting and threshold (Bender et al., 2010; Martinello et al., 2015; Schamiloglu et al., 2022). And at the longer term, remarkable changes in AIS length and position have been observed following artificial and physiological increases in neuronal excitability (Grubb and Burrone, 2010; Grubb et al., 2011; Kuba et al., 2014). When cultured hippocampal neurons were chronically depolarized via high extracellular potassium or channelrhodopsin stimulation, they showed a reversible movement of the AIS away from the soma, as measured by AnkG and Na_V fluorescence (Grubb and Burrone, 2010). In avian nuclear laminaris neurons, AIS length shortens after hearing onset in neurons tuned to higher characteristic frequencies. This plasticity was activity-dependent as well, as AIS shortening was prevented by ablation of the inner ears (Kuba et al., 2014). Both of these changes appear to be largely homeostatic in nature, serving to reduce neuronal excitability. These experiments highlight that physical changes in AIS structure and location are often reflected in alterations in neuronal excitability. While the exact mechanism of this homeostatic plasticity are still being elucidated, it appears that calcium influx via Ca_V1 channels allows for reorganization of the AIS (Grubb and Burrone, 2010; Jahan et al., 2023).

Intriguingly, not all elements of the AIS move in concert during changes in AIS position, suggesting that AIS plasticity may occur through multiple distinct mechanisms. In rat organotypic hippocampal slices, chronic stimulation of CA1 pyramidal neurons with channelrhodopsin resulted in an outward shift in AIS position and a concomitant decrease in pyramidal neuron excitability. Surprisingly, while AnkG and Na_V moved distally after this manipulation, the location of AIS GABAergic synapses were stable, a configuration that may be ideal for reducing neuronal excitability (Wefelmeyer et al., 2015). However, it is not the case that chandelier cell synapses are permanent and unchanging after their formation. These synapses follow homeostatic rules of plasticity after increases in network activity, and the direction of this plasticity flips with developmental shifts in chandelier cell polarity in somatosensory cortex (Pan-Vazquez et al., 2020). When chandelier cell synapses provide depolarizing input in early adolescence, chemogenetic increases in network activity are accompanied by a reduction in chandelier cell synapse numbers, consistent with the idea that chandelier cells are providing excitatory drive to pyramidal neurons at this age. However,

the same manipulation has opposite effects on synapse number when performed in adulthood, showing increasing chandelier cell input to the AIS following increases in activity. This correlates with a periadolescent shift in chandelier synapse polarity and reflects that chandelier cells in adulthood are now able to provide inhibitory input to their postsynaptic targets (Pan-Vazquez et al., 2020; Rinetti-Vargas et al., 2017). Chapters 4 and 5 of this dissertation will focus on the functional consequences of this long time-scale plasticity of GABA synapse polarity at the AIS.

1.5   Chandelier cell morphology and proposed function

Chandelier cells, so named for the candle-like strings of boutons they form on pyramidal neurons, are a class of fast-spiking interneurons in the cortex, hippocampus, and amygdala. Originally described in 1978 (Szentágothai, 1975), their exclusive targeting of the axon initial segment (Somogyi et al., 1982) has inspired a growing body of research into their function. While chandelier cells are relatively sparse compared to other cortical interneuron types, individual chandelier cells can synapse onto a large number of pyramidal neurons, with reports of a single chandelier cell forming contacts with upwards of 100 initial segments (Somogyi et al., 1982), or 30-50% of all pyramidal neurons within their axonal arbor (Inan et al., 2013). Additionally, chandelier cells are electrically-coupled to other chandelier cells through gap junctions (Woodruff et al., 2011), providing a means of synchronizing activity across chandelier cells in close proximity. Finally, the exquisitely specific targeting of chandelier cells to the AIS has led to the hypothesis that far-reaching, interconnected chandelier cells could provide a "veto" over spiking activity in a wide swath of cortex at once. Regardless of this theory's appeal, however, data confirming this privileged role of chandelier cells over other interneuron types has been unsatisfying so far.

In the early 2000s, interest in chandelier cell function took a winding detour through the world of chloride regulation. Data from rat somatosensory cortex suggested an excitatory rather than inhibitory role of chandelier cells, with the observation that APs in chandelier cells could elicit disynaptic, NBQX-sensitive EPSPs in nearby interneurons and occasionally even the recorded chandelier cell itself (Szabadics et al., 2006). This stemmed from low expression of the chloride transporter KCC2 in the axonal membrane

and a resulting depolarization in the reversal potential of GABA in the AIS. This observation set of a frenzy of research into the postsynaptic actions of chandelier cells. If a neuron so strategically positioned to halt activity throughout a network were in fact excitatory, what would that mean about the organization of cortical circuits?

Discrepancies abounded across brain regions, model organisms, and measurement techniques. In mouse amygdala, parvalbumin-positive interneurons were shown to form excitatory feedforward and feedback loops through their depolarizing inputs onto intermediate pyramidal neurons (Woodruff et al., 2006). By contrast, extracellular recordings of subthreshold membrane responses showed that both dendrite-targeting and AIS-targeting interneurons hyperpolarize hippocampal pyramidal neurons, and while occasional disynaptic EPSPs were observed, they tended to be the exception rather than the rule (Glickfield et al., 2009). Disynaptic EPSPs following chandelier cell activation were also observed in mouse motor and somatosensory cortex (Woodruff et al., 2009, 2011) and a state-dependent model of chandelier cell function, where chandelier cells excite relatively quiescent pyramidal neurons while inhibiting highly active neurons, emerged (Woodruff et al., 2011).

While this excitatory versus inhibitory debate raged on, several other theories of chandelier cell function were proposed. In the hippocampus, axo-axonic chandelier cells were shown to fire during the descending phase of theta oscillations, when pyramidal neurons are maximally suppressed and gamma power is highest (Klausberger et al., 2003). Intriguingly, chandelier cells also fire at the start of sharp-wave ripples, a stereotyped pattern of oscillatory activity that is important for memory consolidation (Jadhav, Shantanu et al., 2015). Inhibition of hippocampal chandelier cells *in vivo* was recently shown to lead to remapping of pyramidal cell places fields, consistent with the proposed role of these interneurons in hippocampal memory (Dudok et al., 2021). Together, this suggested a role of chandelier cells in organizing oscillatory activity in networks of principal cells. A similar possible role of chandelier cells in cortical circuits is the entrainment and synchronization of pyramidal cells (Cobb et al., 1995). This may occur through hyperpolarizing GABA that resets or initiates intrinsic subthreshold oscillations in hippocampal pyramidal neurons. While intriguing, it has been difficult to separate the unique roles of basket cell and

chandelier cells in this model of cortical interneuron function. Additionally, while hippocampal pyramidal neurons have intrinsic oscillatory activity that can be encouraged by chandelier cell input, it is unclear if cortical pyramidal cells have this same property. A further proposed function of chandelier cells is to control backpropagation of action potentials into the somatodendritic tree (Inda et al., 2006). A strong shunting input at the AIS, where concerted GABA$_A$ receptor opening leads to a sudden decrease in membrane resistance, could effectively decouple the axonal and somatodendritic domains of a neuron. In one example, during gamma oscillations generated *in vitro*, ectopic action potentials are generated in the distal axon but are prevented from entering the soma by the activation of chandelier cells (Dugladze et al., 2012). This allows the soma and axon of the same neuron to maintain different firing rates during gamma oscillations, an intriguing state that may expand the computational possibilities of a single neuron.

Finally, some features of chandelier cell's specific targeting of initial segments provide tantalizing clues into their function. Electron microscopy of L2/3 chandelier cells in mouse visual cortex has shown that these interneurons do not target the entire AIS equally; instead, chandelier cell synapses preferentially form synapses near cisternal organelles (Schneider-Mizell et al., 2021). As shown in Chapter 2, these cisternal organelles play a role in AP-evoked calcium dynamics in the AIS and define a clustering domain in the AIS that is distinct from Na$_V$-dense, AnkG-organized regions (King et al., 2014). The functional consequences and importance of this clustering region and its specific targeting by chandelier cells remain to be explored in more detail.

1.6   GABAergic development

GABA is the main source of inhibitory input across the brain in adulthood. However, in early development, GABA-mediated depolarization of neurons is crucial for proper brain organization (Ben-Ari, 2002). GABA is uniformly excitatory across the developing brain due to a high intracellular concentration of chloride, the main ion fluxed by GABA$_A$ receptors (Takeuchi and Takeuchi, 1967). This high intracellular chloride concentration drives the reversal potential of chloride above the resting membrane potential of the cell. As a result, GABA drives large events called giant depolarizing potentials, which encourage calcium entry and

may serve to help neurons migrate to the correct locations and form the right connections in development (Ben-Ari, 2002). By the end of prenatal development in humans, and in early postnatal development in rodents, increased expression and function of the chloride exporter KCC2 reduces intracellular chloride concentration and brings the GABA reversal potential to near or just below resting membrane potential. However, GABA maintains a depolarizing effect into adulthood in some cellular compartments of some neurons, most notably axon terminals (Price and Trussell, 2006; Ruiz et al., 2010; Turecek and Trussell, 2001; Zorrilla de San Martin et al., 2017). As discussed above, the postsynaptic action of chandelier synapses on the AIS has been a topic of debate. Does the AIS follow the same rule as the axon, maintaining excitatory GABA throughout life? Or does it display a phenotype more similar to other perisomatic regions, with hyperpolarizing GABA synapses?

A thorough study of GABA reversal potential at the AIS across development performed in our lab has shown that the AIS experiences a delayed shift in GABA reversal potential, a shift that occurs over the course of adolescent development rather than the more typical perinatal switch (Rinetti-Vargas et al., 2017). Briefly, slices containing prefrontal cortex were collected from animals ranging from two weeks to three months old and perforated-patch recordings, which maintain intracellular chloride gradients, were performed to test how the reversal potential of GABA (E_{GABA}) changed over this developmental period. GABA was applied via an iontophoresis pipette to either the AIS or a dendrite, and the cell was held at a range of holding potentials to determine where the GABAergic postsynaptic potential reversed at each location. While GABA applied to the dendrite led to hyperpolarizing responses from postnatal day 10 onwards, E_{GABA} at the AIS remained depolarized above resting membrane potential, and occasionally above AP threshold potential, through adolescent development (P35-55, (Kumar et al., 2009)). This shift in E_{GABA} results from changes in the phosphorylation state and activity of the chloride transporters NKCC1 and KCC2. When revisiting the debate over the excitatory versus inhibitory roles of chandelier cells from the mid-2000s, the varied findings of depolarized and hyperpolarized E_{GABA} across different cell types in fact correlate quite well to the age of the experimental subjects.

Now that the developmental time course of the GABAergic polarity switch at the AIS has been established in our lab and others (Pan-Vazquez et al., 2020; Rinetti-Vargas et al., 2017), the question of the functional consequences of this delayed switch remains. On first glance, it seems that a depolarized E_{GABA} would translate to GABA having excitatory effects on its postsynaptic target. This has been observed in immature amygdala and hippocampal neurons, where GABAergic excitation by chandelier cells is proposed to set off stereotyped patterns of network activity (Szabadics et al., 2006; Woodruff and Yuste, 2008). This conclusion has also been reached in multiple compartmental modeling study investigating how E_{GABA} affects AP generation and EPSP summation (Rojas et al., 2011; Shang et al., 2022; Szabadics et al., 2006). However, depolarized and hyperpolarized EGABA do not map cleanly onto excitatory and inhibitory GABA. Instead, the true relationship is more complicated, dependent on synapse location, ion channels present nearby, the relative timing of synaptic inputs, and other elements of cellular context.

The effects of GABA are highly dependent on context. As discussed above, chloride transporter activity and expression actively regulate the reversal potential of GABA throughout life. The relationship between a neuron's resting membrane potential, its AP threshold, and E_{GABA} at the site of active GABA synapses shape the cell's response (Gulledge and Stuart, 2003). If E_{GABA} is higher than AP threshold, it is likely that the depolarization from a GABAergic PSP will drive the cell to spike. By contrast, an E_{GABA} between resting and threshold potentials may depolarize the cell, but not enough to generate a spike independent of ongoing excitatory synaptic input. However, GABAergic input, in addition to driving the membrane potential towards E_{GABA}, also opens a "shunt" in the membrane surrounding the synapse. Briefly, the concerted opening of $GABA_A$ receptors leads to an overall reduction in membrane resistance, making incoming current less effective at changing the membrane potential (according to Ohm's Law). A GABA synapse whose E_{GABA} rests below threshold and above resting potential may have a dominant effect of shunting the local membrane when activated.

This local shunting effect means that knowing both the position and the timing of GABA synapses relative to other synaptic inputs is necessary to predict the effects of GABA. Excitatory synaptic inputs that arrive near the site of active GABA conductance are likely to be rendered less effective by local shunting,

12

while those that arrive far from GABAergic synapses are less sensitive to the shunt. In a compartmental modeling study exploring the influence of synapse location on GABAergic effects, depolarizing GABA had a stronger excitatory effect when excitatory synapses were located between the GABA synapse and the soma (Lombardi et al., 2021). Distal GABAergic synapses can also drive excitation when they are electrotonically isolated from other depolarizing inputs, as seen in cortical pyramidal neurons (Gulledge and Stuart, 2003). By the same token, temporal overlap between excitatory and "inhibitory" inputs also plays a role in determining the consequences of GABAergic input. Gulledge and Stuart also showed that GABA applied to the soma was excitatory when it preceded an EPSP, but inhibitory when closely linked in time to the same EPSP, likely due to shunting inhibition (Gulledge and Stuart, 2003). This conclusion was supported via compartmental modeling, where excitatory inputs that follow GABAergic input, occurring after the conductance change has ended but while membrane depolarization persists, have a much stronger excitatory effect (Lombardi et al., 2021).

Finally, the ion channels that are present near GABAergic synapses are crucial in determining the effects of GABA on a neuron's excitability. Ion channels ranging from Na_Vs to Ca_V3 to K_Vs have activation and inactivation curves that cross near resting membrane potential, meaning that a small GABA-mediated change in membrane potential could have drastic consequences for channel availability and thus neuronal excitability. Several examples of counterintuitive effects of GABA result from situations like this. For example, in CA1 pyramidal neurons, activation of GABAergic interneurons led to a hyperpolarization of the membrane potential (Cobb et al., 1995). However, as the membrane recovered from this hyperpolarization, rebound APs occurred. When the pyramidal neuron was held at progressively lower membrane potentials before the GABAergic stimulation, this rebound activity decreased in amplitude before disappearing entirely, suggesting that GABA-mediated hyperpolarization from rest was de-inactivating an intrinsic oscillatory mechanism (Cobb et al., 1995). In a set of later experiments, theta-frequency stimulation was fed into CA1 pyramidal neurons to elicit precisely-timed APs. At the same time, electrically-stimulated IPSPs were generated at various phases of the oscillatory cycle. While IPSPs that closely preceded the peak of the theta oscillation tended to delay the upcoming spike, IPSPs that happened

earlier in the cycle instead *advanced* the timing of the next AP. This occurred through recruitment of the hyperpolarization-activated cyclic-nucleotide gated (HCN) channel, as application of the HCN channel blocker ZD7288 prevented spike advancement but not delay (Kwag and Paulsen, 2009). While interneuron input *hyperpolarizes* CA1 pyramidal cells, their overall effect at times *excitatory*, driving rebound APs that allow pyramidal neurons to advance the timing of their action potentials relative to ongoing phasic oscillations.

The converse is true in at least two cases of *depolarizing* GABAergic inputs that have a net *inhibitory* effect on neuronal activity. The first example occurs in dopaminergic axons arising from the substantia nigra pars compacta (Kramer et al., 2020). E_{GABA} is depolarized relative to the inter-spike resting membrane potential in these axons and activation of $GABA_A$ receptors accordingly leads to a depolarization of the axonal membrane potential. However, rather than leading to an increase in AP output, activation of $GABA_A$ receptors instead reduces the amplitude and the speed of tonically-firing APs, with the downstream effect of reducing dopamine release. This counterintuitive inhibitory response to depolarizing GABA arises from depolarization-induced reduction in Na_V availability as well as shunting inhibition (Kramer et al., 2020). A similar pattern helps finely tune tonotopic coding in avian nucleus magnocellularis neurons (Al-Yaari et al., 2021). Neurons that are responsive to a low characteristic frequency (CF) display E_{GABA} that is close the resting membrane potential, and GABAergic input serves mostly as reliable shunting inhibition. By contrast, neurons that are responsive to a high CF have highly depolarizing GABA current. However, these neurons also express K_V1 channels at a higher level than low CF neurons. Computational modeling suggests that strongly depolarizing GABA currents in fact recruit K_V1 channels, leading to a net membrane hyperpolarization and reduction in AP probability (Al-Yaari et al., 2021). This tonotopic regulation of GABA reversal potential as well as K_V1 expression provides a beautiful example of how GABA interacts with intrinsic mechanisms to finely tune AP output and precision.

A multitude of factors make it surprisingly difficult to predict if GABA will have an excitatory or inhibitory effect on the postsynaptic neuron, even if the target region's reversal potential is known. In this dissertation, I explore the consequences of the periadolescent shift in chandelier cell polarity on AP

generation in the AIS. While exploring only a narrow snippet of the function of chandelier cells, this work provides mechanistic insight into how chandelier cells affect their downstream targets that has been largely lacking in the field.

With this body of work, I explore how the physiology of the AIS is affected by the molecular players present there over space and over time. This work clarifies the collection of Ca_Vs found at the AIS and breaks new ground in understanding how these channels are embedded into functional compartments of the AIS (**Chapter 2**). Relatedly, it examines the temporal and spatial dynamics of AIS sodium influx in typical neurons as well as in the case of a unique Na_V mutation (**Chapter 3**). **Chapter 4** uncovers the mechanistic underpinnings of the enigmatic function of chandelier cells. Finally, **Chapter 5** tests the hypothesis that altered chandelier cell function is a key driver of substance use disorders that emerge over the course of adolescence. Taken together, this dissertation provides a greater depth of understanding into the functions of ion channels and synaptic receptors found at the AIS and contributes to the growing appreciation of AIS biology and physiology.

1.7 1.7 References

Al-Yaari, M., Onogi, C., Yamada, R., Adachi, R., Kondo, D., and Kuba, H. (2021). Tonotopic specializations in number, size, and reversal potential of GABAergic inputs fine-tune temporal coding at avian cochlear nucleus.

Arikkath, J., and Campbell, K.P. (2003). Auxiliary subunits: Essential components of the voltage-gated calcium channel complex. Current Opinion in Neurobiology *13*, 298–307.

Battefeld, A., Tran, B.T., Gavrilis, J., Cooper, E.C., and Kole, M.H.P. (2014). Heteromeric Kv7.2/7.3 channels differentially regulate action potential initiation and conduction in neocortical myelinated axons. The Journal of Neuroscience : The Official Journal of the Society for Neuroscience *34*, 3719–3732.

Bean, B.P. (2007). The action potential in mammalian central neurons. Nature Reviews Neuroscience 2007 8:6 *8*, 451–465.

Ben-Ari, Y. (2002). Excitatory actions of GABA during development: The nature of the nurture. Nature Reviews Neuroscience *3*, 728–739.

Bender, K.J., and Trussell, L.O. (2009). Axon initial segment Ca2+ channels influence action potential generation and timing. Neuron *61*, 259–271.

Bender, K.J., and Trussell, L.O. (2012). The physiology of the axon initial segment. Annu Rev Neurosci *35*, 249–265.

Bender, K.J., Ford, C.P., and Trussell, L.O. (2010). Dopaminergic modulation of axon initial segment calcium channels regulates action potential initiation. Neuron *68*, 500–511.

Bender, K.J., Uebele, V.N., Renger, J.J., and Trussell, L.O. (2012). Control of firing patterns through modulation of axon initial segment T-type calcium channels. Journal of Physiology *590*, 109–118.

Benned-Jensen, T., Christensen, R.K., Denti, F., Perrier, J.F., Rasmussen, H.B., and Olesen, S.P. (2016). Live imaging of kv7.2/7.3 cell surface dynamics at the axon initial segment: High steady-state stability and calpain-dependent excitotoxic downregulation revealed. Journal of Neuroscience *36*, 2261–2266.

Bers, D.M. (2002). Cardiac excitation-contraction coupling.

Bock, T., and Stuart, G.J. (2016). The impact of BK channels on cellular excitability depends on their subcellular location. Frontiers in Cellular Neuroscience *10*.

Bourinet, E., and Zamponi, G.W. (2017). Block of voltage-gated calcium channels by peptide toxins. Neuropharmacology *127*, 109–115.

Bucurenciu, I., Kulik, A., Schwaller, B., Frotscher, M., and Jonas, P. (2008). Nanodomain coupling between Ca2+ channels and Ca2+ sensors promotes fast and efficient transmitter release at a cortical GABAergic synapse. Neuron *57*, 536–545.

Burke, K.J., and Bender, K.J. (2019). Modulation of Ion channels in the Axon: Mechanisms and function. Frontiers in Cellular Neuroscience *13*.

Burke, K.J., Keeshen, C.M., and Bender, K.J. (2018). Two Forms of Synaptic Depression Produced by Differential Neuromodulation of Presynaptic Calcium Channels. Neuron *99*, 969-984.e7.

Catterall, W.A. (2011). Voltage-gated calcium channels. Cold Spring Harbor Perspectives in Biology *3*, a003947.

Catterall, W.A., Perez-Reyes, E., Snutch, T.P., and Striessnig, J. (2005). International Union of Pharmacology. XLVIII. Nomenclature and structure-function relationships of voltage-gated calcium channels. Pharmacological Reviews *57*, 411–425.

Chen-Engerer, H.-J., Hartmann, J., Karl, R.M., Yang, J., Feske, S., and Konnerth, A. (2019). Two types of functionally distinct Ca2+ stores in hippocampal neurons. Nature Communications *10*, 3223.

Clarkson, R.L., Liptak, A.T., Gee, S.M., Sohal, X.V.S., and Bender, X.K.J. (2017). D3 receptors regulate excitability in a unique class of prefrontal pyramidal cells. Journal of Neuroscience *37*, 5846–5860.

Cobb, S.R., Buhl, E.H., Halasy, K., Paulsen, O., and Somogyi, P. (1995). Synchronization of neuronal activity in hippocampus by individual GABAergic interneurons. Nature *378*, 75–78.

Coulter, D.A., Huguenard, J.R., and Prince, D.A. (1989). Calcium currents in rat thalamocortical relay neurones: kinetic properties of the transient, low-threshold current. The Journal of Physiology *414*, 587–604.

Davis, J.Q., and Bennett, V. (1994). Ankyrin binding activity shared by the neurofascin/Ll/NrCAM family of nervous system cell adhesion molecules. *269*, 27163–27166.

Dudok, B., Szoboszlay, M., Paul, A., Klein, P.M., Liao, Z., Hwaun, E., Szabo, G.G., Geiller, T., Vancura, B., Wang, B.-S., et al. (2021). Recruitment and inhibitory action of hippocampal axo-axonic cells during behavior. Neuron.

Dugladze, T., Schmitz, D., Whittington, M.A., Vida, I., and Gloveli, T. (2012). Segregation of axonal and network oscillations. Science (1979) *336*, 1458–1462.

Dumenieu, M., Senkov, O., Mironov, A., Bourinet, E., Kreutz, M.R., Dityatev, A., Heine, M., Bikbaev, A., and Lopez-Rojas, J. (2018). The low-threshold calcium channel Cav3.2 mediates burst firing of mature dentate granule cells. Cerebral Cortex *28*, 2594–2609.

Fukaya, R., Yamada, R., and Kuba, H. (2018). Tonotopic variation of the T-Type Ca2+ current in avian auditory coincidence detector neurons. Journal of Neuroscience *38*, 335–346.

Glickfield, L., Roberts, J.D., Somogyi, P., and Scanziani, M. (2009). Interneurons hyperpolarize pyramidal cells along their entire somatodendritic axis. Nat Neurosci *12*, 21–23.

Grubb, M.S., and Burrone, J. (2010). Activity-dependent relocation of the axon initial segment fine-tunes neuronal excitability. Nature 2010 465:7301 *465*, 1070–1074.

Grubb, M.S., Shu, Y., Kuba, H., Rasband, M.N., Wimmer, V.C., and Bender, K.J. (2011). Short- and long-term plasticity at the axon initial segment. Journal of Neuroscience *31*, 16049–16055.

Gulledge, A.T., and Stuart, G.J. (2003). Excitatory actions of GABA in the cortex. Neuron *37*, 299–309.

Hanemaaijer, N.A.K., Popovic, M.A., Wilders, X., and Grasman, S. (2020). Ca2+ entry through NaV channels generates submillisecond axonal Ca2+ signaling. ELife *9*.

Hedstrom, K.L., Ogawa, Y., and Rasband, M.N. (2008). AnkyrinG is required for maintenance of the axon initial segment and neuronal polarity. J Cell Biol *183*, 635–640.

Hu, W., and Bean, B.P. (2018). Differential control of axonal and somatic resting potential by voltage-dependent conductances in cortical Layer 5 pyramidal neurons. Neuron *97*, 1315-1326.e3.

Hu, W., Tian, C., Li, T., Yang, M., Hou, H., and Shu, Y. (2009). Distinct contributions of Na(v)1.6 and Na(v)1.2 in action potential initiation and backpropagation. Nat Neurosci *12*, 996–1002.

Inan, M., Blázquez-llorca, L., Merchán-perez, A., Anderson, S.A., DeFelipe, J., and Yuste, R. (2013). Dense and overlapping innervation of pyramidal neurons by neocortical chandelier cells. Journal of Neuroscience *33*, 1907–1914.

Inda, M.C., Defelipe, J., and Mun, A. (2006). Voltage-gated ion channels in the axon initial segment of human cortical pyramidal cells and their relationship with chandelier cells. PNAS.

Irie, T., and Trussell, L.O. (2017). Double-nanodomain coupling of calcium channels, ryanodine receptors, and BK channels controls the generation of burst firing. Neuron *96*, 856-870.e4.

Jadhav, Shantanu, P., Kemere, C., German, P.W., and Frank, L.M. (2015). Awake Hippocampal Sharp-Wave Ripples Support Spatial Memory. Science *336*, 1454–1458.

Jahan, I., Adachi, R., Egawa, R., Nomura, H., and Kuba, H. (2023). Development/Plasticity/Repair CDK5/p35-Dependent Microtubule Reorganization Contributes to Homeostatic Shortening of the Axon Initial Segment.

Jing, M., Zhang, P., Wang, G., Feng, J., Mesik, L., Zeng, J., Jiang, H., Wang, S., Looby, J.C., Guagliardo, N.A., et al. (2018). A genetically encoded fluorescent acetylcholine indicator for in vitro and in vivo studies. Nature Biotechnology *36*, 726.

Jones, S.L., and Stuart, G.J. (2013). Different calcium sources control somatic versus dendritic SK channel activation during action potentials. Journal of Neuroscience *33*, 19396–19405.

King, A.N., Manning, C.F., and Trimmer, J.S. (2014). A unique ion channel clustering domain on the axon initial segment of mammalian neurons. Journal of Comparative Neurology *522*, 2594–2608.

Klausberger, T., Magill, P.J., Marton, L.F., Roberts, J.D.B., Cobden, P.M., Buzsaki, G., and Somogyi, P. (2003). Brain-state- and cell-type-specific firing of hippocampal interneurons in vivo. Nature *421*, 844–848.

Kole, M.H.P., Letzkus, J.J., and Stuart, G.J. (2007). Axon initial segment Kv1 channels control axonal action potential waveform and synaptic efficacy. Neuron *55*, 633–647.

Kramer, P.F., Twedell, E.L., Shin, J.H., Zhang, R., and Khaliq, Z.M. (2020). Axonal mechanisms mediating g-aminobutyric acid receptor type a (GABA-A) inhibition of striatal dopamine release. Elife *9*, 1–24.

Kraus, R.L., Li, Y., Gregan, Y., Gotter, A.L., Uebele, V.N., Fox, S. V., Doran, S.M., Barrow, J.C., Yang, Z.-Q., Reger, T.S., et al. (2010). In Vitro Characterization of T-Type Calcium Channel Antagonist TTA-A2 and In Vivo Effects on Arousal in Mice. Journal of Pharmacology and Experimental Therapeutics *335*, 409–417.

Kuba, H., Adachi, R., and Ohmori, H. (2014). Activity-dependent and activity-independent development of the axon initial segment. The Journal of Neuroscience *34*, 3443.

Kumar, S., Porcu, P., Werner, D.F., Matthews, D.B., Diaz-granados, J.L., Helfand, R.S., and Morrow, A.L. (2009). The role of GABA A receptors in the acute and chronic effects of ethanol : a decade of progress. Psychopharmacology *205*, 529–564.

Kwag, J., and Paulsen, O. (2009). Bidirectional control of spike timing by GABAA receptor-mediated inhibition during theta oscillation in CA1 pyramidal neurons. Neuroreport *20*, 1209–1213.

Leterrier, C. (2018). The axon initial segment: an updated viewpoint. The Journal of Neuroscience *38*, 1922–17.

Li, L., Bischofberger, J., and Jonas, P. (2007). Differential gating and recruitment of P/Q-, N-, and R-Type Ca2+ channels in hippocampal mossy fiber boutons. Journal of Neuroscience *27*, 13420–13429.

Lombardi, A., Luhmann, H.J., and Kilb, W. (2021). Modelling the spatial and temporal constrains of the GABAergic influence on neuronal excitability. PLoS Comput Biol *17*, e1009199.

Martinello, K., Huang, Z., Lujan, R., Tran, B., Watanabe, M., Cooper, E.C., Brown, D.A., and Shah, M.M. (2015). Cholinergic afferent stimulation induces axonal function plasticity in adult hippocampal granule cells. Neuron *85*, 346–363.

McCobb, D.P., and Beam, K.G. (1991). Action potential waveform voltage-clamp commands reveal striking differences in calcium entry via low and high voltage activated calcium channels. Neuron *7*, 119–127.

McDonough, S.I., Swartz, K.J., Mintz, I.M., Boland, L.M., and Bean, B.P. (1996). Inhibition of calcium channels in rat central and peripheral neurons by omega-conotoxin MVIIC. The Journal of Neuroscience : The Official Journal of the Society for Neuroscience *16*, 2612–2623.

Newcomb, R., Szoke, B., Palma, A., Wang, G., Chen, X.H., Hopkins, W., Cong, R., Miller, J., Urge, L., Tarczy-Hornoch, K., et al. (1998). Selective peptide antagonist of the class E calcium channel from the venom of the tarantula Hysterocrates gigas. Biochemistry *37*, 15353–15362.

Ogawa, Y., and Rasband, M.N. (2008). The functional organization and assembly of the axon initial segment. Current Opinion in Neurobiology *18*, 307–313.

Pan-Vazquez, A., Wefelmeyer, W., Gonzalez Sabater, V., Neves, G., and Burrone, J. (2020). Activity-dependent plasticity of axo-axonic synapses at the axon initial segment. Neuron *106*, 265-276.e6.

Price, G.D., and Trussell, L.O. (2006). Estimate of the chloride concentration in a central glutamatergic terminal: A gramicidin perforated-patch study on the Calyx of Held. Journal of Neuroscience *26*, 11432–11436.

Rebola, N., Reva, M., Kirizs, T., Szoboszlay, M., Lőrincz, A., Moneron, G., Nusser, Z., and DiGregorio, D.A. (2019). Distinct nanoscale calcium channel and synaptic vesicle topographies contribute to the diversity of synaptic function. Neuron *104*, 693-710.e9.

Rinetti-Vargas, G., Phamluong, K., Ron, D., and Bender, K.J. (2017). Periadolescent maturation of GABAergic hyperpolarization at the axon initial segment. Cell Rep *20*, 21–29.

Rojas, P., Akrouh, A., Eisenman, L.N., and Mennerick, S. (2011). Differential effects of axon initial segment and somatodendritic GABAA receptors on excitability measures in rat dentate granule neurons. J Neurophysiol *105*, 366–379.

Rowan, M.J.M., Tranquil, E., and Christie, J.M. (2014). Distinct Kv channel subtypes contribute to differences in spike signaling properties in the axon initial segment and presynaptic boutons of cerebellar interneurons. Journal of Neuroscience *34*, 6611–6623.

Ruiz, A., Campanac, E., Scott, R.S., Rusakov, D.A., and Kullmann, D.M. (2010). Presynaptic GABAA receptors enhance transmission and LTP induction at hippocampal mossy fiber synapses. Nat Neurosci *13*, 431.

Schamiloglu, S., Lewis, E., Hergarden, A.C., Bender, K.J., and Whistler, J.L. (2022). Arrestin-3 agonism at D3 dopamine receptors defines a subclass of second generation antipsychotics that promotes drug tolerance. BioRxiv 2022.08.17.504324.

Schneider-Mizell, C.M., Bodor, A.L., Collman, F., Brittain, D., Bleckert, A.A., Dorkenwald, S., Turner, N.L., Macrina, T., Lee, K., Lu, R., et al. (2021). Structure and function of axo-axonic inhibition. Elife *10*, 1–39.

Scimemi, A., and Diamond, J.S. (2012). The number and organization of Ca2+ channels in the active zone shapes neurotransmitter release from Schaffer collateral synapses. Journal of Neuroscience *32*, 18157–18176.

Shang, Z., Huang, J., Liu, N., and Zhang, X. (2022). Bi-directional control of synaptic input summation and spike generation by GABAergic inputs at the axon initial segment. Neuroscience Bulletin 2022 1–13.

Simms, B.A., and Zamponi, G.W. (2014). Neuronal voltage-gated calcium channels: Structure, function, and dysfunction. Neuron *82*, 24–45.

Sochivko, D., Pereverzev, A., Smyth, N., Gissel, C., Schneider, T., and Beck, H. (2002). The CaV2.3 Ca2+ channel subunit contributes to R-Type Ca2+ currents in murine hippocampal and neocortical neurones. The Journal of Physiology *542*, 699–710.

Somogyi, P., Freund, T.F., and Cowey, A. (1982). The axo-axonic interneuron in the cerebral cortex of the rat, cat and monkey. Neuroscience *7*, 2577–2607.

Spratt, P.W.E., Ben-Shalom, R., Keeshen, C.M., Burke, K.J., Clarkson, R.L., Sanders, S.J., and Bender, K.J. (2019). The autism-associated gene Scn2a contributes to dendritic excitability and synaptic function in the prefrontal cortex. Neuron *103*, 1–13.

Szabadics, J., Varga, C., Molnar, G., Olah, S., Barzo, P., and Tamas, G. (2006). Excitatory effect of GABAergic axo-axonic cells in cortical microcircuits. Science (1979) *311*, 233–235.

Szentágothai, J. (1975). The "module-concept" in cerebral cortex architecture. Brain Research *95*, 475–496.

Takeuchi, A., and Takeuchi, N. (1967). Anion permeability of the inhibitory postsynaptic membrane of the crayfish neuromuscular junction. J. Physiol *191*, 575–590.

Turecek, R., and Trussell, L.O. (2001). Presynaptic glycine receptors enhance transmitter release at a mammalian central synapse. Nature 2001 411:6837 *411*, 587–590.

Ulrich, D., and Huguenard, J.R. (1997). GABA A -Receptor-Mediated Rebound Burst Firing and Burst Shunting in Thalamus. 7–10.

Vierra, N.C., Kirmiz, M., List, D. Van Der, Santana, L.F., and Trimmer, J.S. (2019). Kv2.1 mediates spatial and functional coupling of L-type calcium channels and ryanodine receptors in mammalian neurons. ELife *8*, 1–42.

Vyleta, N.P., and Jonas, P. (2014). Loose coupling between Ca2+ channels and release sensors at a plastic hippocampal synapse. Science *343*, 665–670.

Wang, J., Zhao, J., Liu, Z., Guo, F., and Wang, Y. (2016). Acute Ethanol Inhibition of γ Oscillations Is Mediated by Akt and GSK3 β. Frontiers in Cellular Neuroscience *10*, 1–12.

Wang, K., Lin, M.T., Adelman, J.P., and Maylie, J. (2014). Distinct Ca2+ sources in dendritic spines of hippocampal CA1 neurons couple to SK and Kv4 channels. Neuron *81*, 379–387.

Van Wart, A., Trimmer, J.S., and Matthews, G. (2006). Polarized Distribution of Ion Channels within Microdomains of the Axon Initial Segment.

Wefelmeyer, W., Cattaert, D., and Burrone, J. (2015). Activity-dependent mismatch between axo-axonic synapses and the axon initial segment controls neuronal output. PNAS *112*.

Woodruff, A., and Yuste, R. (2008). Of Mice and Men, and Chandeliers. PLoS Biology *6*, 1833–1836.

Woodruff, A., Xu, Q., Anderson, S.A., and Yuste, R. (2009). Depolarizing effect of neocortical chandelier neurons. Front Neural Circuits *3*, 1–10.

Woodruff, A., McGarry, L., Vogels, T., Inan, M., Anderson, S., and Yuste, R. (2011). State-Dependent Function of Neocortical Chandelier Cells. Journal of Neuroscience *31*, 759–785.

Woodruff, A.R., Monyer, H., and Sah, P. (2006). GABAergic excitation in the basolateral amygdala. Journal of Neuroscience *26*, 11881–11887.

Yu, Y., Maureira, C., Liu, X., and Mccormick, D. (2010). P/Q And N channels control baseline and spike-triggered calcium levels in neocortical axons and synaptic boutons. Journal of Neuroscience *30*, 11858–11869.

Zamponi, G.W., Bourinet, E., and Snutch, T.P. (1996). Nickel block of a family of neuronal calcium channels: Subtype- and subunit-dependent action at multiple sites. Journal of Membrane Biology *151*, 77–90.

Zorrilla de San Martin, J., Trigo, F.F., and Kawaguchi, S.Y. (2017). Axonal GABAA receptors depolarize presynaptic terminals and facilitate transmitter release in cerebellar Purkinje cells. J Physiol *595*, 7477–7493.

Chapter 2   Functional microstructure of Ca$_V$-mediated calcium signaling in the axon initial segment

2.1   Abstract

The axon initial segment (AIS) is a specialized neuronal compartment in which synaptic input is converted into action potential (AP) output. This process is supported by a diverse complement of sodium, potassium, and calcium channels (Ca$_V$). Different classes of sodium and potassium channels are scaffolded at specific sites within the AIS, conferring unique functions, but how calcium channels are functionally distributed within the AIS is unclear. Here, we use conventional two-photon laser scanning and diffraction-limited, high-speed spot two-photon imaging to resolve AP-evoked calcium dynamics in the AIS with high spatiotemporal resolution. In mouse layer 5 prefrontal pyramidal neurons, calcium influx was mediated by a mix of Ca$_V$2 and Ca$_V$3 channels that differentially localized to discrete regions. Ca$_V$3 functionally localized to produce nano- domain hotspots of calcium influx that coupled to ryanodine-sensitive stores, whereas Ca$_V$2 localized to non-hotspot regions. Thus, different pools of Ca$_V$s appear to play distinct roles in AIS function.

2.2 Introduction

Voltage-gated calcium channels (Ca_Vs) occupy a unique functional niche in neurons, affecting both electrical signaling across the membrane and initiating intracellular cascades that regulate ion channel function, cellular processes, and gene expression. Ca_Vs are distributed broadly across somatodendritic and axonal compartments, but only recently have we come to appreciate their role at the intersection of these two compartments, the axon initial segment (AIS). The AIS is enriched with sodium and potassium channels scaffolded by a complex intracellular skeleton and can be a site for specialized inhibitory synaptic input (Bender and Trussell, 2012; Kole and Stuart, 2012; Huang and Rasband, 2018; Leterrier, 2018). Of all Ca_V classes, low voltage- activated Ca_V3s appear to be most commonly expressed in the AIS. AIS Ca_V3 channels were first shown to regulate the threshold and timing of APs in auditory brainstem cartwheel inter- neurons, somatosensory cortex pyramidal cells, and cerebellar Purkinje cells (Bender and Trussell, 2009; Bender et al., 2012). AIS-localized Ca_V3 channels have also been identified at the AIS of cells in avian brainstem and murine cerebellum, hippocampus, and frontal cortex (Martinello et al., 2015; Clarkson et al., 2017; Dumenieu et al., 2018; Fukaya et al., 2018; Hu and Bean, 2018; Jing et al., 2018). In many of these cells, Ca_V3 channels appear to be interspersed in the AIS with other Ca_V classes. This diversity is most apparent in neocortical pyramidal cells, where calcium influx has been reported to be mediated by a range of channel types, including Ca_V1, members of the Ca_V2 family, and Ca_V3 (Clarkson et al., 2017; Hanemaaijer et al., 2020; Yu et al., 2010).

Across neuronal compartments, the spatial organization of Ca_Vs shapes function by linking spatially-restricted calcium influx to nearby calcium-sensitive processes. In somatodendritic compartments, coupling of Ca_Vs to calcium-activated potassium channels regulates action potential (AP) dynamics (Bock and Stuart, 2016; Irie and Trussell, 2017), EPSP amplitude and summation (Wang et al., 2014; Chen-Engerer et al., 2019), and calcium influx (Jones and Stuart, 2013). In the soma, calcium influx through Ca_V1 channels influences activity-dependent transcrip- tion by nuclear transcription factors through activation of CREB via CaMKII (Wheeler et al., 2012). And in axon terminals, the density and spatial arrangement of

Ca$_V$s relative to neurotransmitter release machinery determines release probability (Scimemi and Diamond, 2012; Rebola et al., 2019), shaping both the dynamics of short-term plasticity and its regulation by neuromodulators (Bucurenciu et al., 2008; Vyleta and Jonas, 2014; Burke et al., 2018). However, the organization of Ca$_V$s within the AIS, and how they interact with calcium sensitive signaling pathways, remains unclear.

The AIS serves multiple roles, acting both as a site of electrogenesis for APs as well as a diffusion barrier between somatodendritic and axonal compartments (Bender and Trussell, 2012; Leterrier and Dargent, 2014). These functions are supported by a complex scaffold of intracellular and membrane-bound proteins. Rings of actin connected by spectrins occur periodically along the AIS, forming a scaffold for ankyrin-G to bind and anchor voltage-gated sodium channels (Na$_V$) and voltage-gated potassium (K$_V$) K$_V$7 channels (Leterrier, 2018). K$_V$1.1 and K$_V$1.2 are anchored by a complex that includes PSD-93 the paranodal protein Caspr and typically cluster at actin rings (Ogawa and Rasband, 2008; Pinatel et al., 2017). K$_V$2.1 channels are found at yet another clustering domain enriched with the scaffolding protein gephyrin (King et al., 2014). In neocortical pyramidal cells, these gephyrin-rich sites are punctate, occupying small gaps in an otherwise continuous sheath of Na$_V$-rich membrane. It is here that chandelier cells form GABAergic synapses at the AIS (Inan and Anderson, 2014). Furthermore, a specialized endoplasmic reticulum, termed the cisternal organelle, abuts these gephyrin-rich regions. These cisternal organelles express ryanodine receptors (RyRs) (King et al., 2014), which mediate calcium-induced calcium release from intracellular stores. Interestingly, we have previously shown that RyR-dependent signaling is necessary for dopaminergic signaling cascades that regulate AIS Ca$_V$3 function (Yang et al., 2016), but the local calcium source that evokes calcium-induced-calcium-release at these sites has not been identified. Given the differential distribution of other ion channel classes in the AIS (Lorincz and Nusser, 2008), we hypothesized that a unique complement of Ca$_V$s may be localized to these regions and engage RyRs.

Here, we developed diffraction-limited, high-frequency 2-photon imaging techniques to explore the functional microstructure of AP-evoked calcium signaling in mouse prefrontal pyramidal cell initial segments. Calcium influx was mediated by a mix of Ca$_V$2.1, 2.2, 2.3 and Ca$_V$3-type calcium channels that

27

were distributed into distinct functional domains. In some regions, micron-wide "hotspots" of fast, high-amplitude calcium influx occurred. These hotspots were dominated by Ca_V3-mediated calcium influx, whereas non-hotspot regions were dominated by $Ca_V2.1/2.2$-mediated influx. Furthermore, Ca_V3 channels were preferentially linked to RyR-dependent intracellular stores, suggesting that AIS Ca_V3 channels, commonly expressed in many neuronal classes, are complexed in pyramidal cells to regions associated with GABAergic synaptic transmission. Thus, Ca_Vs may play distinct roles in different subcompartments within the AIS.

2.3   Methods

Ex vivo electrophysiological recordings.

All experiments were performed in accordance with guidelines set by the University of California Animal Care and Use Committee. C57Bl/6 mice of both sexes aged P20 through P30 were anesthetized and 250 μm coronal sections containing medial prefrontal cortex were collected. Cutting solution contained, in mM: 87 NaCl, 25 NaHCO$_3$, 25 glucose, 75 sucrose, 2.5 KCl, 1.25 NaH$_2$PO$_4$, 0.5 CaCl$_2$, and 7 MgCl$_2$, bubbled with 5% CO$_2$/95% O$_2$. After cutting, slices were incubated in the same solution for 30 min at 33°C, then at room temperature until recording. Recording solution contained, in mM: 125 NaCl, 2.5 KCl, 2 CaCl$_2$, 1 MgCl$_2$, 25 NaHCO$_3$, 1.25 NaH$_2$PO$_4$, and 25 glucose, bubbled with 5% CO$_2$/95% O$_2$. Recordings were done at 32-34°C. Osmolarity of the recording solution was adjusted to ~310 mOsm.

Neurons were visualized using Dodt contrast optics for visually-guided whole-cell recording. Patch electrodes were pulled from Schott 8250 glass (3-4 MΩ tip resistance) and filled with a solution containing, in mM: 113 K-gluconate, 9 HEPES, 4.5 MgCl$_2$, 14 Tris$_2$-phosphocreatine, 4 Na$_2$-ATP, 0.3 Tris-GTP, ~290 mOsm, pH 7.2-7.25. Calcium buffers, volume filling dyes, and calcium indicators were included in the internal solution as follows: for linescan calcium imaging experiments, 250 μM Fluo-5F and 20 μM Alexa 594 were added. For calcium imaging at single diffraction limited spots, 600 μM OGB-5N, 0.1 μM EGTA and 20 μM Alexa 594 were added.

Electrophysiological data were acquired using a Multiclamp 700B amplifier (Molecular Devices). For fast linescan experiments, data were acquired at 50 kHz and filtered at 20 kHz. For all other experiments, data were acquired at 20 kHz and filtered at 10 kHz. All recordings were made using a quartz electrode holder to eliminate electrode drift within the slice, enabling stable imaging of diffraction-limited spots in close proximity to the recording electrode (Sutter Instruments). Cells were excluded if series resistance exceeded 20 MΩ or if the series resistance changed by greater than 30%. All recordings were made from Layer 5b pyramidal neurons in prefrontal cortex and data were corrected for a 12 mV junction potential.

Two Photon Imaging.

Two photon laser scanning microscopy (2PLSM) was performed as described previously (Bender and Trussell, 2009). A Coherent Ultra II laser was tuned to 810 nm for morphology and calcium imaging. Fluorescence was collected with either a 40x, 0.8 NA objective (data in Figs. 2.1-2.3) or a 60x, 1.0 NA objective (data in Fig. 2.4) paired with a 1.4 NA oil immersion condenser (Olympus). Dichroic mirrors and band-pass filters (575 DCXR, ET525/70 m-2p, ET620/60 m-2p, Chroma) were used to split fluorescence into red and green channels unless otherwise specified. HA10770-40 photomultiplier tubes (PMTs, Hamamatsu) selected for >50% quantum efficiency and low dark counts captured green fluorescence (Fluo-5F, Fluo-4FF). Red fluorescence (AlexaFluor 594) was captured using R9110 PMTs.

Fluorescence data were collected either using linescan or pointscan configurations. In linescan mode, the laser was repeatedly scanned over a region of axon at a rate of ~0.5 kHz. For 0.5 kHz calcium imaging, data were averaged over 20-40 trials and reported as $\Delta G/G_{sat}$, which was calculated as $\Delta(G/R)/(G/R)_{max}*100$ where G/R_{max} is the maximal fluorescence in saturating calcium (2 mM). In pointscan mode, the laser was parked at a single diffraction-limited spot and calcium influx was imaged with OGB-5N for 25 ms preceding and 100 ms following an AP. Fluorescence data were acquired at 20 kHz. Points were imaged in sets of 5, each sampling a single AP, spaced at 0.5 µm intervals along the visualized edge of the axon. Individual points were imaged in a sequence of 2,4,1,3,5, with 2 being the point most proximal to the soma. Pointscans were imaged between 2 and 35 microns from the axon hillock. Individual APs within the set of 5 points were separated by 250 or 500 ms for calcium and sodium imaging, respectively. Data were averaged over 20-50 repetitions and then smoothed using a 40 point binomial filter in IgorPro before analysis.

Chemicals.

TTA-P2 was from Alomone Labs. ω-conotoxin-MVIIC, ω-conotoxin-GVIA, ω-agatoxin-TK, and SNX-482 were from Peptides International. Nifedipine was from Tocris. All calcium channel antagonists were

prepared as stock solutions in ddH20 in glass vials. Ryanodine was from Tocris and was prepared as a stock solution (25 mM) in DMSO (0.08% final concentration DMSO). Peptide toxins were applied in recording solution supplemented with 1% bovine serum albumin to minimize peptide pre-absorption. Recording solution reservoirs and tubing connecting the reservoir to the recording chamber were made of borosilicate glass, except for 30 mm lengths of Tygon tubing fed through the recirculation peristaltic pump (Ismatec Reglo). Alexa Fluor 594 hydrazide Na^+ salt, Fluo-5F pentapotassium salt, and Oregon Green 488 BAPTA-5N hexapotassium salt were from Invitrogen.

Statistics.

All data are reported as medians with inter-quartile ranges in text and displayed with box plots (medians, quartiles and 90% tails) or violin plots with individual data points overlaid. For linescan experiments, n denotes cells. For pointscan experiments, n denotes point sets, and the number of cells is reported in the text. For cells in Fig. 2.1-2.3, time-locked control cells were interleaved with antagonist cells. Sample sizes were chosen based on standards in the field. No assumptions were made for data distributions, and unless otherwise noted, two-sided, rank-based nonparametric tests were used. Significance level was set for an alpha value of 0.05, and a Holm-Sidak correction was used for multiple comparisons when appropriate. Statistical analysis was performed using Statview, IgorPro 8.0, and the Real Statistic Resource Pack plugin for Microsoft Excel (Release 7.2).

2.4   Results

While action potential-evoked Ca_V-mediated calcium influx has been observed in the AIS of a range of cell classes, the channels that mediate such influx appear to vary from class to class (Bender and Trussell, 2009; Clarkson et al., 2017; Hanemaaijer et al., 2020; Martinello et al., 2015; Yu et al., 2010). To determine the relative contributions of different calcium channel types during AP-evoked calcium influx in mouse prefrontal pyramidal cells, we made whole-cell current-clamp recordings from layer 5 pyramidal neurons in slices prepared from mice aged 20-30 days old. Neurons were filled via whole cell dialysis with an internal solution containing Alexa 594 for morphological identification and the low-affinity calcium indicator Fluo-5F. The AIS was identified by the absence of spines and its stereotyped placement opposite the apical dendrite. Three action potentials (APs) were evoked by somatic current injection (1–1.5 nA, 5 ms duration, 20 ms inter-AP interval), and resultant AIS calcium influx was imaged in linescan mode ~30 μm from the axon hillock (**Fig. 2.1A**). AP-evoked calcium transients were stable over repeated linescan sets performed at time intervals used for subsequent pharmacological studies (**Fig. 2.1B**, **2.1D-E**, median normalized peak $\Delta G/G_{sat}$ = 92.1% of baseline, IQR = 88.4–104.4%, n = 38). This calcium influx was largely blocked by a cocktail of Ca_V antagonists that included blockers of $Ca_V2.1$, $Ca_V2.2$, $Ca_V2.3$, and Ca_V3 channels (1 μM ω-conotoxin MVIIC, 1 μm ω-conotoxin GVIA, 0.2 μM agatoxin TK, 0.5 μM SNX-482, 2 μM TTA-P2) (**Fig. 2.1B**, **2.1D**, median normalized peak $\Delta G/G_{sat}$ = 34.6%, IQR = 22.9–48.4%, n = 7, p = 0.002).

Specific channel antagonists were then applied one-by-one to examine contributions from individual Ca_V classes. Consistent with previous reports across a range of cell types (Bender and Trussell, 2009; Clarkson et al., 2017; Fukaya et al., 2018; Martinello et al., 2015), Ca_V3 channels were a substantial source of AIS calcium influx, as the specific antagonist TTA-P2 reduced calcium influx to 76.6% of baseline (**Fig. 2.1C, 2.1E**, IQR = 75.0–84.9%, n = 11, p = 0.002, Mann Whitney U-Test). Consistent with these results, application of 50 μM $NiCl_2$ caused a similar decrease in calcium influx (**Fig. 2.1E**, IQR = 77.5–86.9%, n = 6, p = 0.004). Additional contributions were made from Ca_V2 channels, with the $Ca_V2.3$-

preferring antagonist SNX-482 reducing AIS calcium influx to 77.6% of baseline (**Fig. 2.1C, 2.1E**, 500 nM; IQR = 72.4–88.4%, n = 9, p = 0.005). Application of the $Ca_V2.1$ channel antagonist ω-agatoxin-TK (200 nM) resulted in variable blockade, with AIS calcium unaffected in some cells and reduced ~30% in others (**Fig. 2.1E**, median: 74.1% of baseline, IQR = 68.6–91.9%, n = 6, p = 0.067). The $Ca_V2.2$ antagonist ω-conotoxin GVIA (1 µM) had little to no effect on AIS calcium (**Fig. 2.1E**, median = 88.9%, IQR = 85.6–91.3%, n = 6, p = 0.137), but the dual $Ca_V2.1/2.2$ antagonist ω-conotoxin MVIIC (1 µM) appeared to have an additive effect, blocking ~40% of total calcium influx (**Fig. 2.1C, 2.1E**, median normalized peak $\Delta G/G_{sat}$ = 61.5%, IQR = 58.3–73.0%, n = 9, p = 4.03 x 10^{-6}). The presence of each of these $Ca_V2.1/2.2$ antagonists at the slice was confirmed by monitoring progressive blockade of evoked EPSPs elicited by a glass bipolar stimulating electrode placed 200 µm lateral to the soma in layer 5 (**Table 2.1**). Lastly, we applied the Ca_V1 antagonist nifedipine (10 µM), which had no effect on AIS calcium influx (**Fig. 2.1E**, median = 99.5%, IQR = 91.9–102.3%, n = 7, p = 0.253). We observed no change in action potential peak, threshold, or half-width throughout the recordings (**Table 2.1**). Together, these data indicate that AP-evoked calcium influx in mouse prefrontal pyramidal cells is supported by a mix of Ca_V2 and Ca_V3 channels.

Ca_V3 channels couple to RyR-dependent stores at the AIS.

Calcium-containing cisternal organelles are found in pyramidal cell initial segments throughout the neocortex (Antón-Fernández et al., 2015; Benedeczky et al., 1994; Sánchez-Ponce et al., 2012; Schlüter et al., 2017), but their role as a potential source of calcium during APs is not well understood. These cisternal organelles localize to discrete sites within the AIS of pyramidal cells (King et al., 2014; Schneider-Mizell et al., 2020) and express ryanodine receptors (RyR) which gate calcium-induced calcium release (Chamberlain et al., 1984; Endo et al., 1970; Van Petegem, 2012). Thus, they may boost AP-evoked calcium transients if they are coupled to Ca_Vs in the AIS. To determine whether calcium release from cisternal organelles is recruited at the AIS during AP generation, we began by comparing AP-evoked calcium influx at the AIS before and after ryanodine application, which at high concentrations (>10 µM) blocks calcium-induced calcium release by preventing the opening of ryanodine receptors (Thomas and Williams, 2012).

In contrast to somatosensory cortex layer 5b pyramidal neurons, where calcium stores account for ~50% of AP-evoked calcium transients (Hanemaaijer et al., 2020), ryanodine (20 µM) had a more modest effect in prefrontal cortex, reducing AP-evoked calcium transients to 85.4% of baseline (**Fig. 2.2A-B**, IQR = 79.2–89.4%, n = 17, p = 0.008). These RyR-dependent stores appear to be the sole source of intracellular calcium in the AIS, as subsequent application of the SERCA-ATPase inhibitor cyclopiazonic acid (CPA, 20 µM), which completely depletes calcium stores, did not lead to further decrements in AP-evoked calcium transients. (**Fig. 2.2A, 2.2C**, ryanodine: 86.4% of baseline, IQR = 85.0–89.1%, ryanodine + CPA (30-min application): 77.0% of baseline, IQR = 75.8–82.7%, n = 7, p = 0.108, Wilcoxon Signed-Rank Test). This suggests that ryanodine receptors govern the majority of store-related calcium release during AP activity in the AIS.

Ryanodine receptors can be coupled tightly to Ca$_V$s, either through direct physical coupling or through indirect nanodomain proximity (Irie and Trussell, 2017; Johenning et al., 2015). In the AIS, ryanodine-sensitive signaling is also important for D3 dopamine receptor-dependent regulation of Ca$_V$3s (Yang et al., 2016). To test if RyR-dependent stores were preferentially coupled to particular Ca$_V$ classes present at the AIS, we performed sequential application of a selective Ca$_V$ antagonist followed by ryanodine (20 µM). With this approach, occlusion of any ryanodine-mediated reductions in AIS calcium would suggest that the blocked Ca$_V$ was the source of calcium that induced subsequent RyR-dependent store release. Interestingly, we found that block of Ca$_V$3 with TTA-P2 produced the clearest occlusion (**Fig. 2.3A-B**, TTA alone: median = 77.6%, IQR = 74.7–85.5%, TTA plus ryanodine = 72.5%, IQR = 71.2–78.9%, n = 6, p = 0.53, Wilcoxon Signed-Rank Test). Conversely, application of ryanodine after pre-application of ω-conotoxin MVIIC resulted in a significant reduction in AIS calcium (**Fig. 2.3A-B**, conotoxin alone: median = 65.4%, IQR = 59.7–74.3%, conotoxin plus ryanodine: median = 56.1%, IQR = 47.4–62.8%, n = 7, p = 0.03, Wilcoxon Signed-Rank Test). A mixed phenotype was observed with Ca$_V$2.3 block by SNX-482; decrements in calcium influx after ryanodine were observed in some cells, but the overall change was not significant (**Fig. 2.3A-B**, SNX alone: median = 73.8%, IQR = 70.3–89.8%, SNX plus ryanodine: median = 69.8%, IQR = 52.9–87.8%, n = 7, p = 0.20, Wilcoxon Signed-Rank Test). Overall, these data

indicate that, of all Ca$_V$ classes found in the AIS, Ca$_V$3s are most likely to be in close proximity to cisternal organelles to evoke release of calcium stores, though it is possible that Ca$_V$2.3s may also couple to ryanodine receptors.

Functional distribution of Ca$_V$3 and Ca$_V$2.1/2.2 in the AIS.

Ryanodine receptors are localized to discrete, ankyrin-G deficient regions of the AIS (King et al., 2014). Given the tight association between Ca$_V$3 channels and RyR-dependent release, we hypothesized that Ca$_V$3 channels may exhibit similar clustering at the functional level, which could be observed using approaches for resolving nanodomain "hotspots" of calcium. Such approaches have been utilized to examine discrete sites of calcium incursion at presynaptic terminals using confocal microscopy entry (DiGregorio et al., 1999; Nakamura et al., 2015), but, to our knowledge, have not been applied at the AIS with two-photon imaging.

To test whether there are sites within the AIS that are hotspots for calcium entry, the excitation laser was parked at one of 5 sites along the wall of the AIS membrane, each 500 nm apart, and APs were evoked while imaging calcium influx at 20 kHz. Calcium influx was reported with a recording solution containing the low-affinity calcium indicator Oregon Green BAPTA-5N (600 µM) supplemented with the slow calcium chelator EGTA (0.1 µM) to restrict imaged signals to sites experiencing rapid, high concentrations of calcium incursion (DiGregorio et al., 1999). The derivative of these events, which corresponds to the time in which calcium fluxes through channels (Sabatini and Regehr, 1999), corresponds to the rising phase of calcium transients (**Fig. 2.4C**). Data were quantified by comparing isochronal influx amplitude at the peak within the set of 5 points to the point (or average of points) 1 µm away on either flank. Using this approach, we identified a range of responses, from small differences across all five sites, to areas where certain locations had calcium incursions that were elevated relative to neighboring sites. In initial experiments that averaged over 50 trials, we found that the majority of sites (46 of 59 sites imaged across 6 cells) fell within a normal distribution (**Fig. 2.4D**), with no appreciable difference in peak calcium influx across all 5 sites. But in the remainder (13 of 59 sites across 6 cells; at least one site identified in

each cell), calcium influx appeared to be more elevated and have sharper kinetics, consistent with a hotspot for calcium entry. Indeed, calcium entry at these sites was ~2x larger than in non-hotspot regions (**Fig. 2.4E**), while flanks 1 µm from the peak both more proximal or more distal to the axon hillock were of comparable amplitude to non-hotspot regions (**Fig. 2.4F**).

These hotspots may represent sites of concentrated calcium influx through Ca_Vs or reflect coupling to intracellular calcium stores. To test this, imaging was repeated (averages of 20 scans) in the presence of Ca_V3 antagonists, $Ca_V2.1/2.2$ antagonists, or with stores depleted with CPA. TTA-P2 (2 µM), $NiCl_2$ (50 µM), and conotoxin-MVIIC (1 µM) reduced overall calcium influx by 33.6%, 32.6%, and 17.1%, respectively (Control median: 4.13 $\Delta G/G_{sat}$, IQR: 3.19–5.60, n= 61; TTA: 2.81, IQR: 2.37–3.66, n = 50; $NiCl_2$: 3.11, IQR: 2.76–3.46, n = 28; MVIIC 2.99, IQR: 2.39–4.26, n = 36). Co-application of TTA-P2, $NiCl_2$, and conotoxin-MVIIC reduced AP-evoked calcium transients below the level at which we could perform hotspot analysis (data not shown; average amplitude across 5 sites: 0.99 ± 0.11 G/G_{sat}; baseline RMS noise per site: 1.78 ± 0.16, n = 29 sites over 5 cells). By contrast, CPA had no effect on peak amplitude when compared to control sets acquired with identical approaches (**Fig. 2.4G;** CPA median: 3.88 IQR: 2.23–4.83, n = 37). This is consistent with the hypothesis that such imaging approaches using high concentrations of calcium indicators supplemented with calcium buffers may uncouple Ca_V-mediated influx from intracellular stores (Collier et al., 2000).

To determine whether Ca_V3 or $Ca_V2.1/2.2$ channels preferentially contribute to hotspot regions, amplitudes at the peak were compared to isochronal amplitudes 1 µm lateral for all data. To determine hotspot frequency after pharmacological manipulation, hotspots were defined as any set with a 1.5x difference between the peak and 1 µm lateral amplitudes. While CPA had no effect on hotspot frequency, application of Ca_V antagonists changed hotspot frequency dramatically. Application of TTA-P2 or $NiCl_2$ eliminated hotspots almost entirely, whereas conotoxin-MVIIC increased the fraction of observed hotspots (**Fig. 2.4H**). Taken together, these data indicate that Ca_V3 channels are uniquely clustered in the AIS, producing nanodomains of elevated calcium entry that then couple to RyR-dependent stores. These regions likely account for hotspots that are eliminated upon Ca_V3 block. By contrast, $Ca_V2.1/2.2$ channels appear

to reside outside of hotspots, perhaps interspersed with ankyrin-G rich regions of AIS membrane. Consistent with this, hotspot frequency increases with $Ca_V2.1/2.2$ block, consistent with the idea that hotspots are more easily resolved if calcium entry in non-hotspot regions is attenuated (e.g., greater signal to noise for resolving hotspots over valleys in between). Thus, these data indicate that pyramidal cells in multiple neocortical regions express a mix of Ca_V2 and Ca_V3 channels in their initial segments, at least in the mouse brain.

2.5   Discussion

Here, we show that calcium channels are functionally distributed in distinct domains within mouse prefrontal pyramidal cell initial segments. Low voltage-activated Ca_V3-mediated calcium influx occurs in spatially restricted "hotspots" whereas high voltage-activated $Ca_V2.1$ and $Ca_V2.2$ channels provide a more diffuse source of calcium. Ca_V3-mediated hotspots preferentially evoked additional calcium release from RyR-dependent intracellular stores, suggesting that hotspots of Ca_V3-mediated influx localize to regions enriched with RyRs that are also sites for GABAergic input and $K_V2.1$ clustering (King et al., 2014). This suggests that different Ca_V classes are functionally localized to discrete regions int the AIS.

Activity-dependent calcium sources in the AIS

Though AP-evoked calcium influx at the AIS is well-established (Callewaert et al., 1996; Schiller et al., 1995), the sources of this calcium influx have only been investigated relatively recently. These sources appear to be remarkably heterogeneous across neuronal classes and species. In mouse auditory brainstem cartwheel cells, $Ca_V3.2$ and SNX-sensitive $Ca_V2.3$ account for ~90% of AP-evoked calcium influx, with no contributions from $Ca_V2.1$ or $Ca_V2.2$ (Bender and Trussell, 2009). By contrast, the first study of pyramidal cells in ferret neocortex found that calcium influx was mediated by $Ca_V2.1$ and $Ca_V2.2$, but not Ca_V3 (Yu et al., 2010). Here, we find that prefrontal pyramidal cells in mouse prefrontal cortex exhibit Ca_V3-mediated influx, consistent with previous reports in rodent neocortex (Clarkson et al., 2017; Hanemaaijer et al., 2020) and other brain regions (Gründemann and Clark, 2015; Jin et al., 2019; Martinello et al., 2015). $Ca_V2.1/2.2$ and $Ca_V2.3$ were also found to contribute to calcium influx, highlighting the relative complexity of calcium signaling in prefrontal pyramidal cell initial segments.

In addition to Ca_V-mediated calcium influx, we found that a small fraction of AP-evoked calcium was released from ryanodine-sensitive intracellular stores in the AIS. Cisternal organelles at the AIS were proposed to be involved in calcium sequestration due to their expression of a calcium pump (Ca^{2+}-ATPase) in pyramidal neurons of the hippocampus (Benedeczky et al, 1994). Cisternal organelles were originally

identified in the initial segments of cortical principal neurons in sensory cortical regions (Benedeczky et al., 1994; Peters et al., 1968). In these regions, a subpopulation of layer 5 pyramidal neurons contain a giant saccular organelle that extends through the entire AIS and accounts for a major fraction of AP-evoked calcium signals (Antón-Fernández et al., 2015; Hanemaaijer et al., 2020; Sánchez-Ponce et al., 2012). Subsequent work has implicated both RyR-dependent and inositol 1,4,5-triphosphate (IP_3) receptor-dependent AIS-localized stores in a range of processes, including calcium influx during APs, modulation of AIS-associated proteins, and experience-dependent structural plasticity of the AIS compartment (Gomez et al., 2020; Irie and Trussell, 2017; Schlüter et al., 2017; Yang et al., 2016). These different effects may reflect diverse structures and functions in AIS calcium stores across cell types. Conversely, different modes of calcium release from intracellular stores may be recruited by different stimuli.

Functional compartmentalization of calcium influx within the AIS

In mature neocortical pyramidal cells, $Na_V1.6$ channels cluster in the regions of the AIS more distal to the soma, whereas $Na_V1.2$ channels cluster in the region more proximal to the soma (Hu et al., 2009). This subcompartmental distribution affects the integrative properties of the AIS in health and disease (Hu et al., 2009; Spratt et al., 2019), and raised the question of whether similar functional specializations are found in Ca_Vs localized to the AIS. To test this, we adapted spot imaging techniques used previously to observe calcium microdomains with single-photon sources for use with 2-photon microscopy (DiGregorio et al., 1999; Nakamura et al., 2015). This approach revealed that calcium influx in the AIS occurs in two domains, with hotspots of calcium interspersed within regions of more consistent calcium influx (**Fig. 2.4**). These calcium nanodomains are hypothesized to result from channel clustering, as isochronal calcium measurements at increasing distances from the calcium source decreased in amplitude, a consequence of calcium diffusing away from its entry site (DiGregorio et al., 1999). It is plausible that the hotspots observed here represent points that are, by chance, closer to clusters of Ca_Vs; however, the differential pharmacological block of hotspots and non-hotspots with selective Ca_V antagonists indicates that these hotspots indeed reflect a differential organization of Ca_V channel types at the AIS. In future efforts, it will

be important to develop immunostaining methods sensitive enough to visualize these channels relative to other AIS constituents to validate these functional observations.

The biophysics of different Ca_V channel types may shape calcium hotspot kinetics and duration as well. Relative to currents measured by step-commands, proportionally more current is carried by low voltage-activated than high voltage-activated channels during an AP waveform (McCobb and Beam, 1991). Low voltage-activated channels, including Ca_V3, can exhibit rapid activation kinetics when membrane voltage transitions quickly from rest to very depolarized potentials (e.g., during an AP) (Chemin et al., 2001, 2002). As such, Ca_V3 channels open earlier than other Ca_V isoforms in the course of the AP, and, due to their slower deactivation kinetics, remain open longer than high voltage-activated channels, resulting in a longer duration of calcium influx through these channels (Lambert et al., 1998; McCobb and Beam, 1991). Hotspot calcium influx observed here is consistent with these biophysical aspects of AP-evoked Ca_V3-mediated currents.

Pharmacological block of RyR-dependent stores indicates that Ca_V3 channels couple to intracellular sources of calcium in the AIS. $Ca_V2.3$ channels may also couple to these stores, but data were less clear, perhaps due to incomplete block of $Ca_V2.3$ channels by SNX-482 (Sochivko et al., 2002). These ryanodine receptor-dependent stores are found at ankyrin-G deficient regions of the axonal membrane (King et al., 2014), clustered with other AIS constituents. The components of the cytoskeletal scaffolding machinery that tether Na_V, K_V channels, and $GABA_A$ receptors in the AIS have been well-characterized (Leterrier, 2018), but how Ca_Vs are anchored at the AIS remains an open question. One possibility, at least for Ca_Vs clustered with RyRs, are $K_V2.1$ channels. $K_V2.1$ channels have been shown to tether Ca_V1 channels near junctions between the endoplasmic reticulum and plasma membrane (Fox et al., 2015), as well as to enhance the functional coupling of these channels to ryanodine receptors (Vierra et al., 2019). However, whether or not $K_V2.1$ channels tether Ca_Vs near the cisternal organelle at the AIS specifically has not been explored. Another candidate is amphiphysin II/Bridging integrator 1 (BIN1), a T-tubule protein involved in localizing $Ca_V1.2$ channels in cardiac myocytes (Hong et al., 2010). This protein shows specific localization to neuronal AIS and nodes of Ranvier, but whether this protein interacts with AIS channels has not been

explored (Butler et al., 1997). Additionally, the presence of auxiliary subunits on Ca_V1 and Ca_V2 channels has been shown to affect localization and membrane expression (Arikkath and Campbell, 2003). As Ca_V3 channels do not associate with auxiliary subunits (Simms and Zamponi, 2014), Ca_V3 and Ca_V2 could acquire differential expression within the AIS through differential association of auxiliary subunits with scaffolding elements.

Functional implications of calcium channel compartmentalization within the AIS

$GABA_A$ receptors cluster in ankyrin-G deficient pockets of the AIS and associate with clustered non-conducting $K_V2.1$ channels that stabilize junctions between cisternal organelles and the plasma membrane (Benedeczky et al., 1994; King et al., 2014; Kirmiz et al.; Schneider-Mizell et al., 2020). These clustering domains appear across species and brain regions (King et al., 2014). The coupling of Ca_V3 channels to ryanodine receptors, as well as the clustering of these channels into hotspots, suggests that Ca_V3 channels co-localize with GABAergic chandelier synapses in the AIS. Thus, AIS Ca_V3s may be particularly sensitive to chandelier cell input. In mature neurons, hyperpolarizing inhibition has been shown to relieve Ca_V3 channels from steady-state inactivation, thereby promoting rebound spike bursts immediately following an inhibitory epoch (Molineux et al., 2006; Ulrich and Huguenard, 1997). Interestingly, chandelier inputs switch from depolarizing to hyperpolarizing the AIS membrane relatively late in development (Lipkin and Bender, 2020; Pan-Vazquez et al., 2020; Rinetti-Vargas et al., 2017), corresponding to the emergence of synchronized higher-order rhythmicity in cortical networks (Uhlhaas and Singer, 2011). Whether this tight coupling between AIS GABAerigic inputs and Ca_V3s contributes to the development of these network phenomena remains to be explored.

In addition to regulation by chandelier inputs, calcium hotspots could enable precise neuromodulatory control over spike properties, perhaps within select temporal windows relative to neuromodulator signals. In striatal medium spiny neurons, a form of credit assignment for synapses that encode information relevant to reward has been demonstrated based on coincident dopaminergic and glutamatergic signaling (Yagishita et al., 2014). In cells that express D3 dopamine receptors, including

some prefrontal pyramidal cells, AIS Ca$_V$3 function can be modulated in ways that hyperpolarize the voltage dependence of channel inactivation, in turn lowering the number of channels available for activation during subsequent APs (Clarkson et al., 2017; Yang et al., 2016), This process depends on RyR-dependent intracellular stores (Yang et al., 2016). Thus, in D3 receptor-expressing neurons, Ca$_V$3 channels may be modulated only when dopamine binding to D3 receptors coincides with neuronal activity that promotes calcium influx through AIS Ca$_V$3s. This may result in preferential suppression of Ca$_V$3 function in cells that are actively spiking, thereby modulating only the population of neurons that were active during dopaminergic signaling.

2.6 Figures
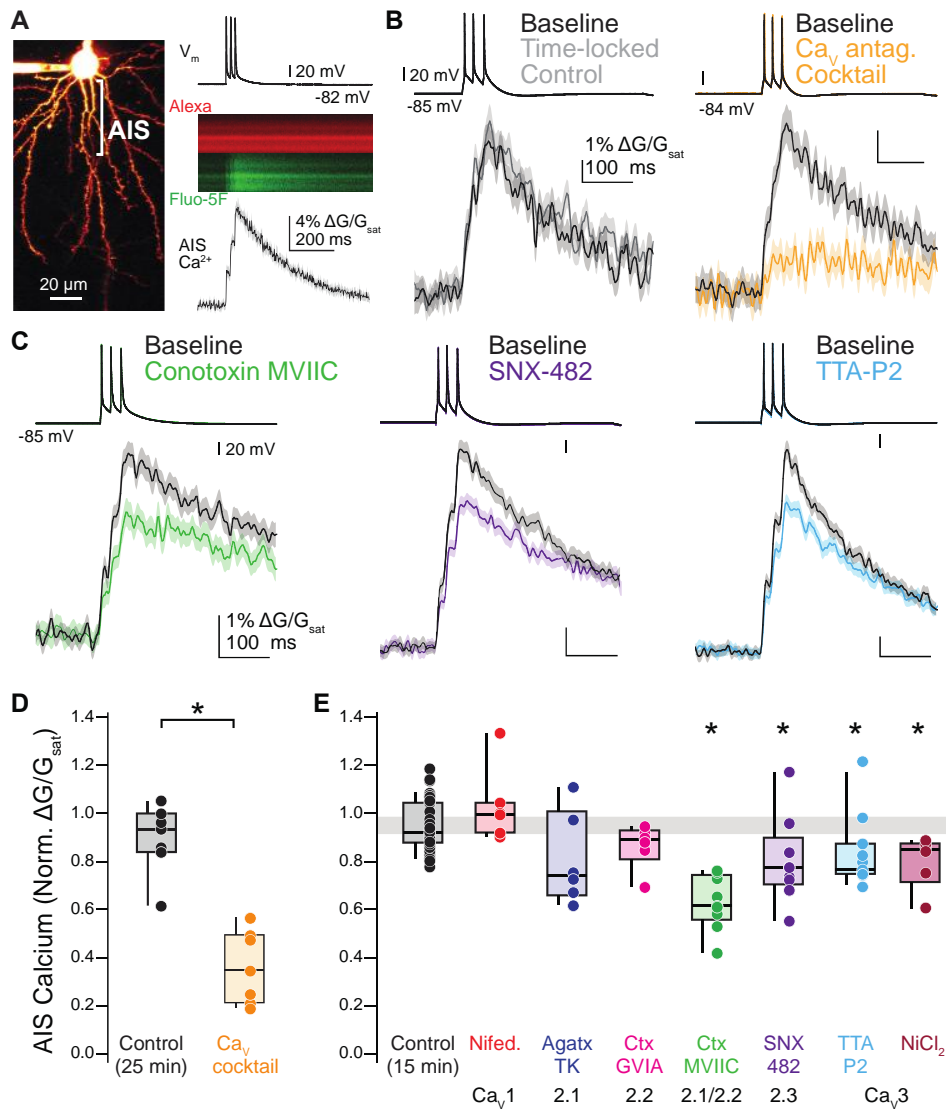
Figure 2.1. Ca$_V$2.1, Ca$_V$2.2, and Ca$_V$3 contribute to calcium influx at the axon initial segment.

A. Left: Two photon laser-scanning microscopy (2PLSM) z-stack of a Layer 5 pyramidal neuron visualized with Alexa 594. AIS indicated by bracket. Right: example linescan of AIS averaged over 20 trials. APs were evoked with somatic current injection (1 nA, 5 ms, 20 ms interstimulus interval).

B. Left: Representative time-locked control cell. Linescan data displayed as mean ± standard error. Baseline, black; post, gray. Right: Representative effects of Ca$_V$ antagonist cocktail on AIS calcium. Baseline, black; cocktail, yellow.

C. Representative examples of selective Ca$_V$ antagonists on AIS calcium. Baseline, black; antagonists, other colors.

D. Summary of the effects of the Ca$_V$ antagonist cocktail on AIS calcium.

E. Summary of the effects of individual Ca$_V$ antagonists on AIS calcium. Gray bar represents 95% confidence interval of control data.
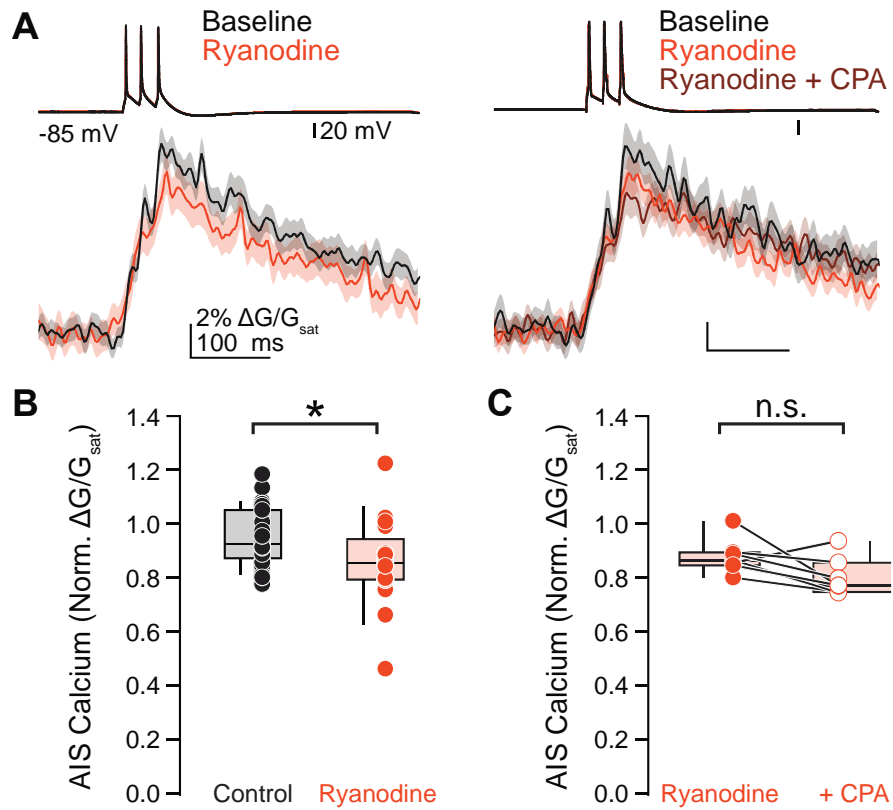
Figure 2.2. Calcium stores contribute to AIS calcium during AP firing.

A. Left: Representative effect of ryanodine (20 µM) on AIS calcium. Right: Representative effect of sequential ryanodine and cyclopiazonic acid (CPA, 20 µM) application on AIS calcium. Linescan data presented as mean ± standard error.
B. Summary of the effects of ryanodine on AIS calcium.
C. Summary of the effects of sequential application of ryanodine and cyclopiazonic acid.
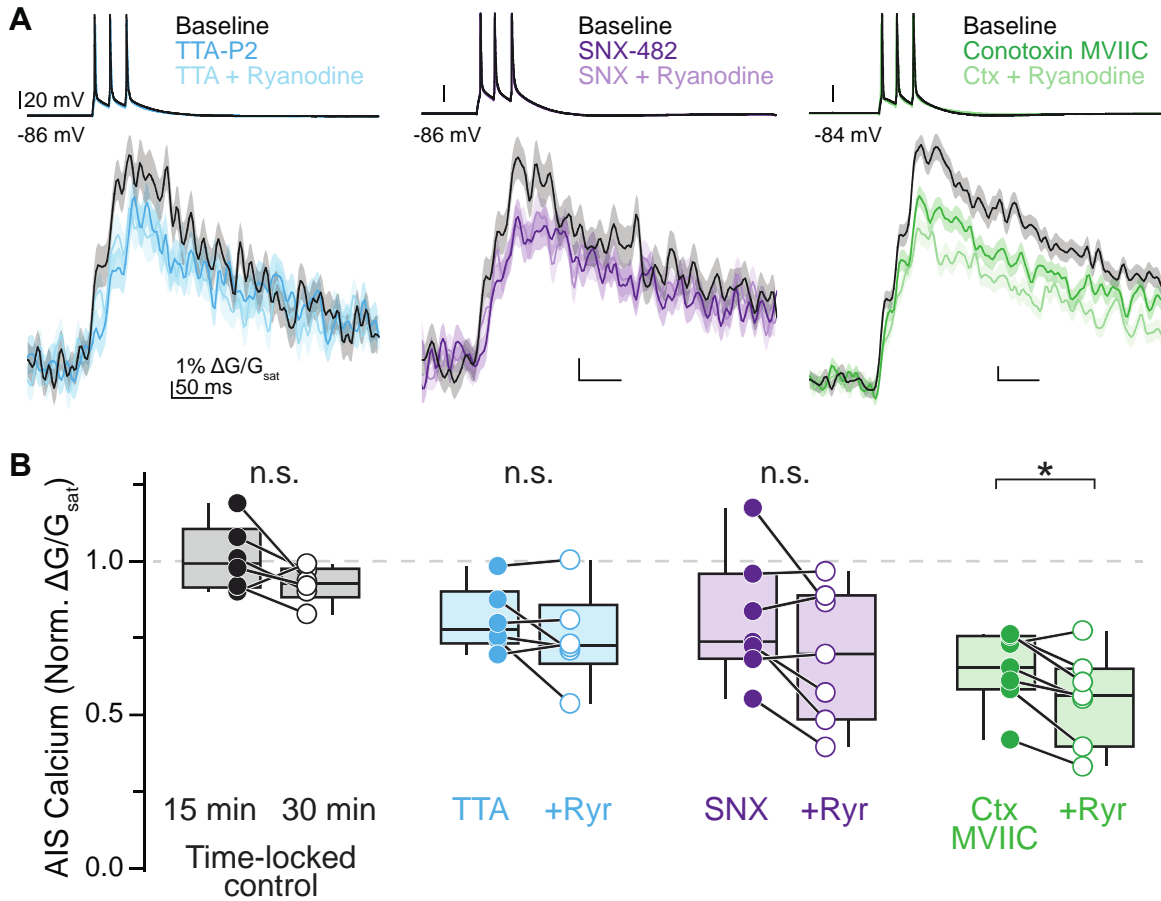
Figure 2.3. Ca$_V$3 channels couple to ryanodine receptors on calcium stores.

A. Representative effects of sequential block of individual Ca$_V$ types and release from calcium stores. Linescan data shown as mean ± standard error.
B. Summary of the effects of Ca$_V$ antagonists and ryanodine block. n.s.: not significant.
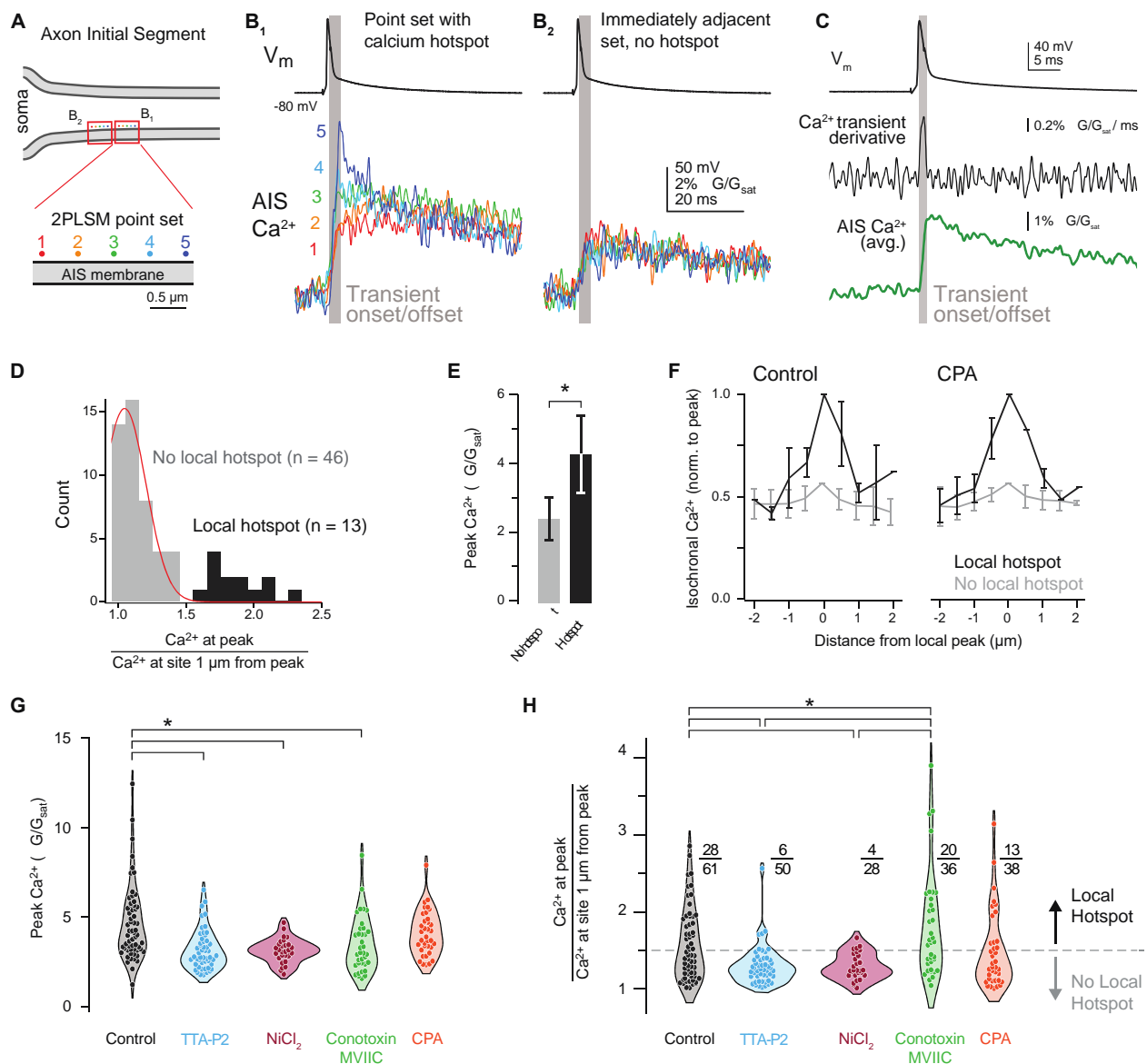
Figure 2.4. Ca$_V$3 channels and Ca$_V$2.1/2.2 exhibit distinct functional distributions.

A. Schematic of 2PLSM pointscan imaging protocol. Points were imaged in sets of 5, with each point separated by 0.5 µm. The laser was parked at a single diffraction-limited point for 25 ms preceding and 100 ms following an AP and calcium influx was measured with OGB-5N. Points were scanned in the sequence 2, 4, 1, 3, 5 and each point sampled a single AP. Data was averaged over 20-50 repetitions.

B. Isochronal calcium peaks from neighboring point sets. Calcium influx at each point is color-coded as in panel A. B$_1$ shows a point set with a hotspot at point 5. B$_2$ is the point set immediately adjacent to B$_1$ and shows equivalent calcium influx across all points. Gray bar indicates the calcium transient onset and offset.

C. Average of calcium influx from a set of 5 points (bottom), its time derivative (middle), aligned to somatic voltage recording (top). Grey bar defines transient onset/offset, which corresponds to deviation of time derivative above baseline noise.

D. Distribution of point sets containing hotspots. Peak calcium influx at the brightest point was divided by the isochronal calcium influx at the point(s) 1 µm away. 46 of 59 sites imaged fell within a normal

distribution, while 13 sites exhibited higher relative calcium influx. Black, point sets containing a local hotspot; gray, point sets with no local hotspot. Red line indicates the fit of a normal distribution. Total distribution fit for normality (Shapiro Wilk test p = 0.0016).

E. Calcium influx at hotspots was approximately 2x higher than calcium influx at non-hotspot points. Black, point sets containing a local hotspot; gray, point sets with no local hotspot. Data are plotted as mean ± standard deviation.

F. Comparison of the flanks of point sets with a local hotspot and those without. Black, point sets containing a local hotspot; gray, point sets with no local hotspot. Data are plotted as mean ± standard deviation for each 0.5 µm increment from the brightest point of the set.

G. Influence of selective Ca_V antagonists or store depletion on peak calcium influx during pointscan imaging. Circles represent single point sets. Black, control; cyan, TTA-P2; red, $NiCl_2$; green, ω-conotoxin MVIIC; orange, CPA. * : p < 0.001, Kruskall-Wallis test with rank-sum post hoc.

H. Influence of selective Ca_V antagonists or store depletion on calcium hotspots. Hotspots were classified as points >1.5 times brighter than the point(s) 1 µm away. Dotted gray line represents the distinction between point sets with a local hotspot (above) and those without (below). Color code as in panel F. * : p < 0.001, Kruskall-Wallis test with rank-sum post hoc.

2.7 Tables

Table 2.1: Changes in action potential waveform properties across the course of recording.

 * denotes a p-value < 0.05. One-way ANOVAs or two-tailed t-tests were performed for each waveform property, as appropriate. Paired t-tests were performed for EPSP amplitudes.

	ΔV_m (mV)	$\Delta V_{threshold}$ (mV)	Δ AP half-width (% baseline)	Δ AP peak (mV)	Δ rheobase (pA)	n	Baseline EPSP (mV)	Post-drug EPSP (mV)
time-locked control (15 min)	0.48 ± 1.05	-1.34 ± 1.86	98 ± 10	-3.23 ± 5.43	-10 ± 29.21	35	5.9 ± 4.6	4.6 ± 3.8
conotoxin MVIIC	0.47 ± 0.54	-2.12 ± 1.55	99 ± 8	-3.12 ± 2.97	-21.43 ± 26.73	8	4.8 ± 3.8	0.5 ± 0.4 *
SNX-482	-0.18 ± 0.72	-0.92 ± 1.00	102 ± 11	-3.39 ± 5.00	-14.29 ± 19.67	8	—	—
TTA-P2	0.37 ± 0.65	-0.90 ± 0.88	100 ± 8	-3.02 ± 2.75	7.50 ± 37.36	11	—	—
nifedipine	0.89 ± 0.42	-0.62 ± 1.42	102 ± 5	-3.12 ± 3.00	-8.33 ± 25.82	5	—	—
conotoxin GVIA	0.14 ± 0.90	-0.78 ± 1.46	103 ± 5	-2.64 ± 1.17	-20.00 ± 20.92	5	5.3 ± 6.0	4.8 ± 5.5
agatoxin TK	0.55 ± 0.42	-2.55 ± 0.84	104 ± 8	-2.70 ± 1.71	-12.50 ± 13.69	6	5.6 ± 4.1	1.5 ± 1.4 *
ryanodine	1.49 ± 4.24	-1.14 ± 1.60	106 ± 11	-5.38 ± 5.62	-13.46 ± 24.19	14	—	—
Nickel(II) chloride	-0.26 ± 3.09	-0.51 ± 2.34	102 ± 5	-2.54 ± 2.58	-33.33 ± 43.78	6	—	—
time-locked control (25 min)	0.54 ± 0.87	-3.25 ± 2.37	101 ± 7	-5.16 ± 3.71	-37.50 ± 37.91	6	3.7 ± 2.4	2.1 ± 0.8
Ca$_V$ antagonist cocktail	0.37 ± 0.83	-3.26 ± 2.96	105 ± 4	-2.58 ± 6.08	-45.00 ± 32.60	5	2.5 ± 1.5	0.5 ± 0.4 *

2.8   References

Antón-Fernández, A., Rubio-Garrido, P., DeFelipe, J., and Muñoz, A. (2015). Selective presence of a giant saccular organelle in the axon initial segment of a subpopulation of layer V pyramidal neurons. Brain Struct. Funct. *220*, 869–884.

Arikkath, J., and Campbell, K.P. (2003). Auxiliary subunits: Essential components of the voltage-gated calcium channel complex. Curr. Opin. Neurobiol. *13*, 298–307.

Bender, K.J., and Trussell, L.O. (2009). Axon initial segment Ca2+ channels influence action potential generation and timing. Neuron *61*, 259–271.

Bender, K.J., and Trussell, L.O. (2012). The Physiology of the Axon Initial Segment. Annu. Rev. Neurosci. *35*, 249–265.

Benedeczky, I., Molnár, E., and Somogyi, P. (1994). The cisternal organelle as a Ca2+-storing compartment associated with GABAergic synapses in the axon initial segment of hippocampal pyramidal neurones. Exp. Brain Res. *101*, 216–230.

Butler, M.H., David, C., Ochoa, G.C., Freyberg, Z., Daniell, L., Grabs, D., Cremona, O., and De Camilli, P. (1997). Amphiphysin II (SH3p9; BIN1), a member of the amphiphysin/Rvs family, is concentrated in the cortical cytomatrix of axon initial segments and nodes of ranvier in brain and around T tubules in skeletal muscle. J. Cell Biol. *137*, 1355–1367.

Callewaert, G., Eilers, J., and Konnerth, A. (1996). Axonal calcium entry during fast "sodium" action potentials in rat cerebellar Purkinje neurones. J. Physiol. *495*, 641–647.

Chamberlain, B.K., Volpe, P., and Fleischer, S. (1984). Inhibition of calcium-induced calcium release from purified cardiac sarcoplasmic reticulum vesicles. J. Biol. Chem. *259*, 7547–7553.

Chemin, J., Monteil, A., Bourinet, E., Nargeot, J., and Lory, P. (2001). Alternatively spliced α1G (Cav3.1) Intracellular loops promote specific T-type Ca2+ channel gating properties. Biophys. J. *80*, 1238–1250.

Chemin, J., Monteil, A., Perez-Reyes, E., Bourinet, E., Nargeot, J., and Lory, P. (2002). Specific

contribution of human T-type calcium channel isotypes (α_{1G}, α_{1H} and α_{1I}) to neuronal excitability. J. Physiol. *540*, 3–14.

Clarkson, R.L., Liptak, A.T., Gee, S.M., Sohal, X.V.S., and Bender, X.K.J. (2017). D3 receptors regulate excitability in a unique class of prefrontal pyramidal cells. J. Neurosci. *37*, 5846–5860.

Collier, M.L., Ji, G., Wang, Y.X., and Kotlikoff, M.I. (2000). Calcium-induced calcium release in smooth muscle: Loose coupling between the action potential and calcium release. J. Gen. Physiol. *115*, 653–662.

DiGregorio, D.A., Peskoff, A., and Vergara, J.L. (1999). Measurement of action potential-induced presynaptic calcium domains at a cultured neuromuscular junction. J. Neurosci. *19*, 7846–7859.

Endo, M., Tanaka, M., and Ogawa, Y. (1970). Calcium induced release of calcium from the sarcoplasmic reticulum of skinned skeletal muscle fibres. Nature *228*, 34–36.

Fox, P.D., Haberkorn, C.J., Akin, E.J., Seel, P.J., Krapf, D., and Tamkun, M.M. (2015). Induction of stable ER-plasma-membrane junctions by Kv2.1 potassium channels. J Cell Sci *128*, 2096–2105.

Fukaya, R., Yamada, R., and Kuba, H. (2018). Tonotopic variation of the T-Type Ca2+ current in avian auditory coincidence detector neurons. J. Neurosci. *38*, 335–346.

Gomez, L.C., Kawaguchi, S.Y., Collin, T., Jalil, A., del Pilar Gomez, M., Nasi, E., Marty, A., and Llano, I. (2020). Influence of spatially segregated IP3-producing pathways on spike generation and transmitter release in Purkinje cell axons. Proc. Natl. Acad. Sci. U. S. A. *117*, 11097–11108.

Gründemann, J., and Clark, B.A. (2015). Calcium-activated potassium channels at nodes of Ranvier secure axonal spike propagation. Cell Rep. *12*, 1715–1722.

Hanemaaijer, N.A.K., Popovic, M.A., Wilders, X., and Grasman, S. (2020). Ca2+ entry through NaV channels generates submillisecond axonal Ca2+ signaling. Elife *9*.

Hong, T.-T., Smyth, J.W., Gao, D., Chu, K.Y., Vogan, J.M., Fong, T.S., Jensen, B.C., Colecraft, H.M., and Shaw, R.M. (2010). BIN1 localizes the L-type calcium channel to cardiac T-tubules. PLoS Biol. *8*, e1000312.

Hu, W., Tian, C., Li, T., Yang, M., Hou, H., and Shu, Y. (2009). Distinct contributions of Na(v)1.6 and

Na(v)1.2 in action potential initiation and backpropagation. Nat. Neurosci. *12*, 996–1002.

Inan, M., and Anderson, S.A. (2014). The chandelier cell , form and function. Curr. Opin. Neurobiol. *26*, 142–148.

Irie, T., and Trussell, L.O. (2017). Double-nanodomain coupling of calcium channels, ryanodine receptors, and BK channels controls the generation of burst firing. Neuron *96*, 856-870.e4.

Jin, X., Chen, Q., Song, Y., Zheng, J., Xiao, K., Shao, S., Fu, Z., Yi, M., Yang, Y., and Huang, Z. (2019). Dopamine D2 receptors regulate the action potential threshold by modulating T-type calcium channels in stellate cells of the medial entorhinal cortex. J. Physiol. *597*, 3363–3387.

Johenning, F.W., Theis, A.-K., Pannasch, U., Rückl, M., Rüdiger, S., and Schmitz, D. (2015). Ryanodine receptor activation induces long-term plasticity of spine calcium dynamics. PLOS Biol. *13*, e1002181.

King, A.N., Manning, C.F., and Trimmer, J.S. (2014). A unique ion channel clustering domain on the axon initial segment of mammalian neurons. J. Comp. Neurol. *522*, 2594–2608.

Kirmiz, M., Palacio, S., Thapa, P., King, A.N., Sack, J.T., and Trimmer, J.S. Organizing neuronal ER-PM junctions is a conserved nonconducting function of Kv2 plasma membrane ion channels.

Lambert, R.C., McKenna, F., Maulet, Y., Talley, E.M., Bayliss, D.A., Cribbs, L.L., Lee, J.H., Perez-Reyes, E., and Feltz, A. (1998). Low-voltage-activated Ca2+ currents are generated by members of the Ca(v)T subunit family (α1G/H) in rat primary sensory neurons. J. Neurosci. *18*, 8605–8613.

Leterrier, C. (2018). The axon initial segment: an updated viewpoint. J. Neurosci. *38*, 1922–17.

Leterrier, C., and Dargent, B. (2014). No Pasaran! Role of the axon initial segment in the regulation of protein transport and the maintenance of axonal identity. Semin. Cell Dev. Biol. *27*, 44–51.

Lipkin, A.M., and Bender, K.J. (2020). Flipping the switch: Homeostatic tuning of chandelier synapses follows developmental changes in GABA polarity. Neuron *106*, 199–201.

Lorincz, A., and Nusser, Z. (2008). Cell-type-dependent molecular composition of the axon initial segment. J. Neurosci. *26*, 7172–7180.

Martinello, K., Huang, Z., Lujan, R., Tran, B., Watanabe, M., Cooper, E.C., Brown, D.A., and Shah, M.M. (2015). Cholinergic afferent stimulation induces axonal function plasticity in adult hippocampal

granule cells. Neuron *85*, 346–363.

McCobb, D.P., and Beam, K.G. (1991). Action potential waveform voltage-clamp commands reveal striking differences in calcium entry via low and high voltage activated calcium channels. Neuron *7*, 119–127.

Molineux, M.L., Mcrory, J.E., Mckay, B.E., Hamid, J., Mehaffey, W.H., Rehak, R., Snutch, T.P., Zamponi, G.W., and Turner, R.W. (2006). Specific T-type calcium channel isoforms are associated with distinct burst phenotypes in deep cerebellar nuclear neurons. *103*, 5555–5560.

Nakamura, Y., Harada, H., Kamasawa, N., Matsui, K., Rothman, J.S., Shigemoto, R., Silver, R.A., DiGregorio, D.A., and Takahashi, T. (2015). Nanoscale distribution of presynaptic Ca2+ channels and its impact on vesicular release during development. Neuron *85*, 145–158.

Ogawa, Y., and Rasband, M.N. (2008). The functional organization and assembly of the axon initial segment. Curr. Opin. Neurobiol. *18*, 307–313.

Pan-Vazquez, A., Wefelmeyer, W., Gonzalez Sabater, V., Neves, G., and Burrone, J. (2020). Activity-dependent plasticity of axo-axonic synapses at the axon initial segment. Neuron *106*, 265-276.e6.

Van Petegem, F. (2012). Ryanodine receptors: Structure and function. J. Biol. Chem. *287*, 31624–31632.

Peters, A., Proskauer, C.C., and Kaiserman-Abramof, I.R. (1968). The small pyramidal neuron of the rat cerebral cortex. The axon hillock and initial segment. J. Cell Biol. *39*, 604–619.

Pinatel, D., Hivert, B., Saint-Martin, M., Noraz, N., Savvaki, M., Karagogeos, D., and Faivre-Sarrailh, C. (2017). The Kv1-associated molecules TAG-1 and Caspr2 are selectively targeted to the axon initial segment in hippocampal neurons. J. Cell Sci. *130*, 2209–2220.

Rinetti-Vargas, G., Phamluong, K., Ron, D., and Bender, K.J. (2017). Periadolescent Maturation of GABAergic Hyperpolarization at the Axon Initial Segment. Cell Rep. *20*, 21–29.

Sabatini, B.L., and Regehr, W.G. (1999). Timing of synaptic transmission. Annu. Rev. Physiol. *61*, 521–542.

Sánchez-Ponce, D., Blázquez-Llorca, L., Defelipe, J., Garrido, J.J., and Muñoz, A. (2012). Colocalization of α-actinin and synaptopodin in the pyramidal cell axon initial segment. Cereb. Cortex *22*, 1648–

1661.

Schiller, J., Helmchen, F., and Sakmann, B. (1995). Spatial profile of dendritic calcium transients evoked by action potentials in rat neocortical pyramidal neurones. J. Physiol. *487*, 583–600.

Schlüter, A., Del Turco, D., Deller, T., Gutzmann, A., Schultz, C., and Engelhardt, M. (2017). Structural plasticity of synaptopodin in the axon initial segment during visual cortex development. Cereb. Cortex *27*, 4662–4675.

Schneider-Mizell, C.M., Bodor, A.L., Collman, F., Brittain, D., Bleckert, A.A., Dorkenwald, S., Turner, N.L., Macrina, T., Lee, K., Lu, R., et al. (2020). Chandelier cell anatomy and function reveal a variably distributed but common signal. BioRxiv 2020.03.31.018952.

Simms, B.A., and Zamponi, G.W. (2014). Neuronal voltage-gated calcium channels: Structure, function, and dysfunction. Neuron *82*, 24–45.

Sochivko, D., Pereverzev, A., Smyth, N., Gissel, C., Schneider, T., and Beck, H. (2002). The CaV2.3 Ca2+ channel subunit contributes to R-Type Ca2+ currents in murine hippocampal and neocortical neurones. J. Physiol. *542*, 699–710.

Spratt, P.W.E., Ben-Shalom, R., Keeshen, C.M., Burke, K.J., Clarkson, R.L., Sanders, S.J., and Bender, K.J. (2019). The autism-associated gene Scn2a contributes to dendritic excitability and synaptic function in the prefrontal cortex. Neuron *103*, 1–13.

Thomas, N.L., and Williams, A.J. (2012). Pharmacology of ryanodine receptors and Ca2+-induced Ca2+ release. Wiley Interdiscip. Rev. Membr. Transp. Signal. *1*, 383–397.

Uhlhaas, P.J., and Singer, W. (2011). The development of neural synchrony and large-scale cortical networks during adolescence: Relevance for the pathophysiology of schizophrenia and neurodevelopmental hypothesis. Schizophr. Bull. *37*, 514–523.

Ulrich, D., and Huguenard, J.R. (1997). Nucleus-specific chloride homeostasis in rat thalamus. J. Neurosci. *17*, 2348–2354.

Vierra, N.C., Kirmiz, M., List, D. Van Der, Santana, L.F., and Trimmer, J.S. (2019). Kv2.1 mediates spatial and functional coupling of L-type calcium channels and ryanodine receptors in mammalian neurons.

Elife *8*, 1–42.

Yagishita, S., Hayashi-Takagi, A., Ellis-Davies, G.C.R., Urakubo, H., Ishii, S., and Kasai, H. (2014). A critical time window for dopamine actions on the structural plasticity of dendritic spines. Science (80- .). *345*, 1616–1620.

Yang, S., Ben-Shalom, R., Ahn, M., Liptak, A.T.A.T., van Rijn, R.M.R.M., Whistler, J.L.J.L., and Bender, K.J.K.J. (2016). β-Arrestin-dependent dopaminergic regulation of calcium channel activity in the axon initial segment. Cell Rep. *16*, 1518–1526.

Yu, Y., Maureira, C., Liu, X., and Mccormick, D. (2010). P/Q And N channels control baseline and spike-triggered calcium levels in neocortical axons and synaptic boutons. J. Neurosci. *30*, 11858–11869.

Chapter 3   Calcium channels are the dedicated source of calcium entry at the axon initial segment

3.1   Introduction

Chapter 2 of this dissertation demonstrates that a diverse population of Ca_Vs are localized to the AIS, with differential spatial distributions that hint at distinct functional roles of Ca_V types. Although concurrently applying antagonists to a range of Ca_Vs dramatically reduced calcium influx (**Fig. 2.1B, D**), there was a persistent calcium residual that was resistant to block. This contrasts with previous experiments examining bouton calcium influx, which was fully blocked with the application of calcium channel antagonists (Hanemaaijer et al. 2020, Burke et al., 2018). We theorized that incomplete block of CaV2.3 channels by SNX-482 (Sochivko et al., 2002) underlies this residual calcium influx, which may then be amplified by ryanodine-mediated calcium release from cisternal organelles (**Fig 2.2**). However, a theory that voltage-gated sodium channels (Na_Vs) at the AIS may have the ability to flux calcium has recently emerged (Hanemaaijer et al., 2020, Filipis et al., 2022). This chapter focuses on testing the hypothesis that a proportion of AIS calcium influx occurs through sodium channels in mouse prefrontal pyramidal neurons.

The idea that Na_Vs could underlie AIS calcium influx emerged as a result of calcium-imaging and voltage-imaging experiments in Layer 5b pyramidal neurons in rat somatosensory cortex (Hanemaaijer et al., 2020). Here, action potential waveforms were captured in current-clamp recording mode and played back to the same neuron in voltage-clamp mode (an approach called AP-clamp) to result in a voltage deviation of the same magnitude. By circumventing the role of Na_Vs in generating the AP-related membrane depolarization, this approach enabled the authors to assess the possibility of Na_V-mediated calcium influx using pharmacological tools. Using this method, the authors showed a nearly 90% reduction in calcium influx at the AIS after application of the specific Na_V antagonist tetrodotoxin (TTX, 1 µM). This led the authors to conclude that calcium influx at the AIS occurs via Na_Vs. While calcium influx through Na_Vs has

been established in recordings from squid giant axon (Meves and Vogel, 1973), reports of calcium-conducting Na$_V$s in mammalian cells are rare outside of pathological conditions (Santana et al., 1998).

To test the involvement of Na$_V$s in calcium influx at the AIS, we performed pointscan and linescan imaging of sodium and calcium influx to compare the relative timing and spatial organization of the two ion fluxes. We found that calcium influx occurred during AP repolarization, and was distinct from sodium influx that occurred during the rising phase of the AP (Filipis and Canepari, 2021; Pressler and Strowbridge, 2019) but see (Hanemaaijer et al., 2020). Additionally, we showed that Ca$_V$2.1/2.2 channels provide a more substantial fraction of AIS calcium than previously reported in somatosensory cortex, suggesting that dampened activation of these channels in voltage-clamp may account for the effects of TTX shown in Hanemaaijer et al., 2020. Finally, by measuring calcium influx dynamics in neurons expressing a variant of AIS-localized Na$_V$1.2 that disrupts the channel's ion selectivity, we showed that calcium influx through Na$_V$s would in fact occur earlier in the course of an action potential than what we observe in baseline conditions. Overall, these results strongly imply that calcium influx at the AIS occurs exclusively through Ca$_V$s.

3.2 Methods

Mice.

Scn2a[K1422E] mice on the C57BL/6J strain were generated using CRISPR/Cas9 to introduce the modification of K1422 by homology directed repair. A single nucleotide change was introduced in codon 1422 (AAA>GAA), resulting in a glutamate residue being encoded at the modified position. A single guide RNA (TCCTTTAAAT- GTGGCCTGTA) with low predicted off-target effects, and a 151 bp repair oligo (5' – CCTTGTTTCCACTTTTACTCTGATAATCTATTTCCTAA

ACTATAAAAAAGAGAAGAAGTATATATGTTGATTGTTTTACAGGCCACATTT**G**AAGGATGG

ATGGATATCATGTATGCAGCTGTTGACTCAAGAAATGTAAGTTTACTTTGG) were delivered to C57BL/6J embryos at the two-cell stage using electroporation by the Northwestern University Transgenic and Targeted Mutagenesis Laboratory.

Potential founders were screened by PCR of genomic DNA using primers outside the repair oligo homology region (Table 1), and the region of interest was cloned into pCR-TOPO (ThermoFisher) and Sanger sequenced. The mosaic K1422E founder was backcrossed to C57BL/6 J mice (Jackson Labs, #000664, Bar Harbor, ME) to generate N1 offspring. N1 offspring were genotyped by Sanger sequencing to confirm transmission of the K1422E editing event and were screened for off-target events by Sanger sequencing of all potential sites with <3 mismatches. N1 males with the confirmed on- target event and without predicted off-target events were bred with C57BL/6J females to establish the line Scn2a[em1Kea] (MGI:6390565), which is maintained as an isogenic strain on C57BL/6J by continual backcrossing of Scn2a[K1422E/+] heterozygous mice (abbreviated as Scn2a[E/+]) with inbred C57BL/6J mice. Heterozygous Scn2a[E/+] and Scn2a^{+/+} (wild-type, abbreviated as WT) mice for experiments were obtained from this breeding at generations >N3.

Mice were maintained in a specific pathogen free (SPF) barrier facility with a 14 h light/10 h dark cycle and access to food and water ad libitum. Both female and male mice were used for all experiments. All animal care and experimental procedures were approved by the Northwestern University and UC San

Francisco Animal Care and Use Committees in accordance with the National Institutes of Health Guide for the Care and Use of Laboratory Animals.

Ex vivo electrophysiological recordings.

Electrophysiological recordings were performed as described in Chapter 2. All experiments were performed in accordance with guidelines set by the University of California Animal Care and Use Committee. Briefly, 250 μm coronal section containing medial prefrontal cortex were collected from P20-30 male and female mice using a sucrose cutting solution. Recordings were made in ACSF as described in Chapter 2. Recordings were performed at 32-34°C, with the exception of SBFI and Fluo4ff experiments, which were performed at room temperature (22°C). Osmolarity of the recording solution was adjusted to ~310 mOsm.

Glass patch electrodes were filled with an internal solution described above and supplemented with calcium buffers, volume filling dyes, and calcium or sodium indicators as follows: for linescan calcium imaging experiments, 250 μM Fluo-5F and 20 μM Alexa 594 were added. For fast (5.3kHz) linescan sodium imaging, 2 mM SBFI, 0.1 μM EGTA, and 20 μM Alexa 594 were added. For fast linescan calcium imaging, 500 μM Fluo-4FF and 0.1 μM EGTA were added. For calcium imaging at single diffraction limited spots, 600 μM OGB-5N, 0.1 μM EGTA and 20 μM Alexa 594 were added. For pointscan sodium imaging, 500 μM ING-2 was added.

Electrophysiological data were acquired as described in Chapter 2. Cells were excluded if series resistance exceeded 20 MΩ or if the series resistance changed by greater than 30%. All recordings were made from Layer 5b pyramidal neurons in prefrontal or primary somatosensory cortex and data were corrected for a 12 mV junction potential. We observed no change in action potential peak, threshold, or half-width throughout the recordings (**Table 3.1**).

Two Photon Imaging.

Two photon laser scanning microscopy (2PLSM) was performed as described in Chapter 2, with the following modifications: The laser was tuned to 790 nm for SBFI-based imaging. Fluorescence was

collected with either a 40x, 0.8 NA objective (data in Figs. 3.4) or a 60x, 1.0 NA objective (data in Figs. 3.1-3.3) paired with a 1.4 NA oil immersion condenser (Olympus). For ING-2 based imaging, the epifluorescence filters were removed and the transfluorescence filters were replaced with a single 535/150 bandpass filter (Semrock) and all fluorescence was collected on HA10770-40 PMTs.

Fluorescence data were collected either using linescan or pointscan configurations. In linescan mode, the laser was repeatedly scanned over a region of axon at a rate of ~0.5 or 5.3 kHz. For 0.5 kHz calcium imaging, data were averaged over 20-40 trials and reported as $\Delta G/G_{sat}$, which was calculated as $\Delta(G/R)/(G/R)_{max}*100$ where G/R_{max} is the maximal fluorescence in saturating calcium (2 mM). For 5.3 kHz imaging, data were averaged over 50 trials and reported as the change in fluorescence detected by HA10770-40 PMTs ($\Delta G/G$). In pointscan mode, the laser was parked at a single diffraction-limited spot and calcium and sodium influx were imaged with OGB-5N and ING-2, respectively, for 25 ms preceding and 100 ms following an AP. Fluorescence data were acquired at 20 kHz. Points were imaged and processed as described in Chapter 2.

Chemicals.

TTA-P2 was from Alomone Labs. ω-conotoxin-MVIIC was from Peptides International. All calcium channel antagonists were prepared as stock solutions in ddH20 in glass vials. Conotoxin was applied in recording solution supplemented with 1% bovine serum albumin to minimize peptide pre-absorption. Alexa Fluor 594 hydrazide Na^+ salt, Fluo-5F pentapotassium salt, SBFI tetraammonium salt, Fluo-4FF pentapotassium salt, and Oregon Green 488 BAPTA-5N hexapotassium salt were from Invitrogen. ION NaTRIUM-Green-2 TMA+ salt (ING-2) was from Abcam.

Statistics.

Statistics were performed as described in Chapter 2.

3.3 Results

Temporally distinct AP-evoked sodium and calcium dynamics in the AIS

Imaging data in Chapter 2 suggests that AIS calcium entry occurs during AP repolarization. While this is consistent with Ca_V activity during APs in a range of imaging and electrophysiological studies at various sites within the axon (Bischofberger et al., 2002; Díaz-Rojas et al., 2015; DiGregorio et al., 1999; Nakamura et al., 2015; Rowan et al., 2014), it has recently been proposed that AIS calcium influx during APs is mediated by Na_Vs, not Ca_Vs (Hanemaaijer et al., 2020). If this is the case, we hypothesized that calcium and sodium influx should occur simultaneously. To test this, we started by comparing AP-evoked sodium and calcium transients using 5.3 kHz linescans that transected the AIS 30 µm from the hillock. Linescans were collected at room temperature (22 °C) to best separate the rising and falling phase of the AP. The low-affinity indicator Fluo-4FF was used for calcium imaging and the most commonly utilized sodium indicator, SBFI, was used for sodium imaging. SBFI reports changes in sodium concentration with a shift in emission spectra, which, with 2-photon excitation sources, is best visualized as a reduction in fluorescence (Bender et al., 2010; Rose et al., 1999). Sodium and calcium transients were fitted with sigmoid functions and event onset was defined as the time at which the sigmoid fit first exceeded the amplitude of baseline root-mean-squared noise (RMS). Similar to previous reports (Hanemaaijer et al., 2020), we found that the rising slope of sodium and calcium transients were comparable (**Fig. 3.1B**, Na median = 0.07% ΔF/F per s, IQR = 0.06–0.08% ΔF/F per s, n = 11, Ca median = 0.07% ΔF/F per s, IQR = 0.04–0.08% ΔF/F per s, n = 9, p = 0.6, Mann-Whitney). However, sodium influx typically occurred during the rising phase of the AP whereas calcium influx occurred during the falling phase (relative to AP peak, Na median = -0.343 ms, IQR = -0.4045–0.063 ms, n = 11 cells, Ca median = 0.901 s, IQR = 0.622–1.284, n = 9 cells, p = 0.0007, Mann-Whitney). The mean difference in transient onset was 1.2 ms, comparable to the duration of the rising phase of the AP in these recording conditions (median = 0.85 ms, IQR 0.76–0.94 ms, n = 20 cells).

SBFI typically reported ion influx with a higher signal-to-noise ratio than Fluo-4FF (peak amplitude/baseline RMS). This alone may account for the earlier event onset for SBFI-based signals. To

test whether this was the case, we analyzed the subset of data in which signal-to-noise was comparable between sodium and calcium imaging scans (**Fig. 3.1B**). In these cases, sodium influx still preceded calcium influx. Thus, these data suggest that sodium and calcium influx occur through distinct mechanisms that can be separated temporally.

Previous work has suggested that the timing of calcium influx during an AP may shift to earlier parts of the AP at high temperature, in part due to differences in gating kinetics between Na_Vs and Ca_Vs (Sabatini and Regehr, 1996). This would be best assayed with the temporal fidelity of pointscan imaging. Unfortunately, we found the high basal fluorescence of SBFI resulted in significant photo-toxicity when the laser was parked at single sites. Therefore, we made use of a relatively new sodium-sensitive dye, ING-2, which reports increases in sodium concentration with an increase in fluorescence intensity without a change in emission spectra (Filipis and Canepari, 2021). Sodium influx was imaged in sets of 5 sites each 0.5 µm apart, as done for calcium pointscan imaging. But in contrast to calcium imaging data, sodium influx did not appear to occur with regions that could be defined as hotspots. Rather, data reporting the relative amplitudes of the peak sodium transient relative to a neighbor 1 µm away could all be fit within a normal distribution (**Fig. 3.2B-C**, Shapiro-Wilk test for normality, p = 0.36), consistent with relatively constant Na_V density throughout the AIS (Kole et al., 2008; Leterrier, 2018; Lorincz and Nusser, 2008).

Similar to data obtained at 22 °C, sodium influx imaged 25-35 µm from the axon hillock again preceded the peak of the AP at 32-34°C (median = -0.65 ms, IQR = -0.9625 – -0.5ms, n = 56 sites, 23 cells). Moreover, these events tended to precede AP onset as measured in the soma (median = -0.05 ms, IQR = -0.3625–0.1 ms). This may be due in part to the conduction delay between the AIS site of AP initiation and the soma (Kole et al., 2007; Rowan et al., 2014; Spratt et al., 2021), and in part to subthreshold sodium influx before AP onset (Filipis and Canepari, 2021).

Comparisons with onset kinetics of calcium transients imaged with pointscan approaches again revealed marked differences between the onset of sodium and calcium entry. Calcium influx was detectable 1.2 ms after sodium influx, typically during the first millisecond of AP repolarization (**Fig. 3.2D**, median = 0.75, IQR =0.60–1.35 ms after AP threshold, median = 0.35, IQR = 0.10–0.85 ms after AP peak, n = 38

sites, 13 cells). Similar results were obtained in conditions where Ca_V3 or $Ca_V2.1/2.2$ channels were blocked (TTA-P2: median = 1.1 ms, IQR = 0.8–1.6 ms after AP threshold, median = 0.6 ms, IQR = 0.3–1.1 ms after AP peak, n = 33 point sets, 7 cells; $NiCl_2$: median = 1.1 ms, IQR = 0.5–1.7 ms after AP threshold, median = 0.63 ms, IQR = 0.13–1.3 ms after AP peak, n = 28 point sets, 5 cells; ω-conotoxin MVIIC: median = 1.25 ms, IQR = 0.9625–1.575 ms after AP threshold, median = 0.7 ms, IQR = 0.375–1.1 ms after AP peak, n = 16 sites, 5 cells), and when intracellular stores were depleted with CPA (median = 0.7 ms, IQR = 0.4–0.9375 ms after AP threshold, median = 0.15 ms, IQR = -0.0375–0.4875 ms after AP peak, n = 20 point sets, 5 cells). As block of various Ca_Vs did not alter transient onset timing, these results argue against the idea that an early, Na_V-driven component of calcium influx can be "unmasked" upon Ca_V blockade.

To determine if these differences in timing between sodium influx and calcium influx truly reflect their reliance of different channels, we turned to a Na_V variant with disrupted ion selectivity; in short, a sodium channel that is known to conduct calcium ions. A variant in SCN2A, the gene encoding $Na_V1.2$, shows altered ion selectivity, gating, and TTX-sensitivity. This *de novo* missense variant affects one of the four critical residues within the ion-conducting pore domain that confer selectivity for sodium over other cations (11-13). This variant alters the overall charge of the ion selectivity filter, converting the positively-charged amino acid, lysine (K), to the negatively-charged amino acid glutamic acid (E). The resultant channel, SCN2A-p.K1422E, which has been studied in heterologous expression systems, loses sodium selectivity, instead becoming a mixed, non-selective cation channel with apparent permeability for sodium, potassium, and calcium with diminished overall conductance (Heinemann et al., 1992, Schlief et al., 1996). As $Na_V1.2$ is expressed in the proximal AIS in prefrontal pyramidal neurons (Hu et al., 2009), we repeated our calcium imaging experiments in cortical slices taken from these mice to understand how altered ion selectivity in $Na_V1.2$ affects the timing of calcium influx.

To determine the temporal dynamics of calcium influx through $Na_V1.2^{E/+}$ channels, we imaged AP-evoked calcium transients in the AIS with high spatiotemporal precision using 2-photon pointscan imaging. Under control conditions, calcium influx occurs during AP repolarization in all regions of the axon, including the AIS, and can be separated temporally from sodium influx occurring during AP depolarization

(Geiger and Jonas, 2000, Ritzau-Jost et al., 2014, Filipis and Canepari., 2021, Hanemaaijer et al., 2020). But in cells expressing K1422E channels, we hypothesized that calcium influx would also occur during the rising phase of the AP in regions enriched with $Na_V1.2$ channels. In mature pyramidal neurons, $Na_V1.2$ channels are clustered densely in a region of the AIS proximal to the soma, whereas $Na_V1.6$ channels are enriched in the distal AIS (**Fig. 3.3A**) (Hu et al., 2009). Therefore, we imaged the proximal and distal initial segment, 5 and 30 μm from the axon hillock, respectively, corresponding to regions enriched for or lacking $Na_V1.2$ channels (**Fig. 3.3B**). Consistent with a lack of $Na_V1.2$ channels in the distal AIS, there were no differences in the amplitude or timing of AP-evoked calcium transients in the distal AIS. By contrast, calcium transients were larger and occurred earlier, before the peak of the AP, in the proximal AIS of $Scn2a^{K1422E}$ cells (Amplitude, WT: 2.8 ± 0.2 $\Delta G/G_{sat}$, $Scn2a^{E/+}$: 3.8 ± 0.3 $\Delta G/G_{sat}$, P = 0.014; timing relative to AP peak, WT: 0.62 ± 0.15 ms, n= 12, $Scn2a^{E/+}$: -0.17 ± 0.13 ms, n = 10; P < 0.001, unpaired t- test; **Fig. 3.3B–D**). Thus, these data indicate that when $Na_V1.2$- K1422E channels flux calcium into the cell, this influx occurs during AP depolarization in the AIS, significantly earlier than calcium influx through Ca_Vs.

Overall, these data are most consistent with the hypothesis that Ca_Vs are the sole source of calcium influx from the extracellular space in the AIS. This contrasts with work in rat somatosensory cortex (S1), where AP-evoked calcium transients were partially blocked by the Ca_V3 antagonist TTA-P2 (1 μM at equilibrium in the extracellular solution), but, notably, not affected by the Ca_V2 peptide antagonist ω-conotoxin MVIIC (2 μM, applied via pressure ejection local to the AIS) (Hanemaaijer et al., 2020). Therefore, we tested whether mouse S1 pyramidal cells differ from mouse prefrontal pyramidal cells in the expression of $Ca_V2.1/2.2$ channels in the AIS by applying ω-conotoxin MVIIC (1 μM at equilibrium in the extracellular solution) to L5 pyramidal neurons in the somatosensory cortex, again imaging calcium influx resulting from 3 APs as in **Fig. 2.1**. Similar to mouse prefrontal cortex, block of $Ca_V2.1/2.2$ channels reduced peak calcium influx by over 35% (**Fig. 3.4A-B**, median = 63.8%, IQR = 42.5–69.9%, n = 5; time-locked controls: median = 90.9%, IQR = 79.6–95.5%, n = 5; p = 0.012, Mann Whitney U-Test). Thus, these data indicate that pyramidal cells in multiple neocortical regions express a mix of Ca_V2 and Ca_V3 channels

in their initial segments, at least in the mouse brain. Furthermore, these results show through multiple lines of evidence that calcium influx at the AIS occurs through Ca_Vs rather than Na_Vs.

3.4   Discussion

A recent study in rat somatosensory cortex layer 5b pyramidal cells examining the sources of AP-evoked AIS calcium elevations found that a similar fraction of AIS calcium was sensitive to Ca_V3 antagonists as in mouse prefrontal cortex (**Fig. 2.1**), whereas inhibition of intracellular store calcium release reduced AP-evoked calcium transients to a far higher degree than observed here, consistent with the presence of giant saccular organelle in somatosensory cortical pyramidal neurons (Antón-Fernández et al., 2015; Hanemaaijer et al., 2020). Of note, peptide antagonists of $Ca_V2.x$ channels, puffed for 3s onto the AIS, did not affect AIS calcium influx, despite almost completely blocking AP-evoked calcium signals in axonal boutons. It was therefore proposed that the residual influx was through Na_Vs rather than Ca_Vs, based in part on the observations that influx was sensitive to Na_V antagonists and that the rising kinetics of sodium and calcium transients were similar (Hanemaaijer et al., 2020). Similar TTX-sensitivity has been observed previously for AIS calcium transients largely blocked by subthreshold depolarizations in auditory brainstem interneurons; however, this sensitivity was attributed to a failure to activate AIS-localized Ca_Vs, rather than calcium influx through Na_Vs, as these transients could be blocked completely by Ca_V antagonists in the absence of TTX (Bender and Trussell 2009).

In contrast to work in rat, we observed a marked block of AP-evoked influx in mouse prefrontal and somatosensory pyramidal cells from Ca_V2 antagonists when allowed to equilibrate in the extracellular solution (**Fig. 2.1, Fig. 3.4**). Furthermore, we found that the kinetics of sodium and calcium influx were indeed identical, but that calcium influx lagged sodium influx in ways that were consistent with sodium and calcium influx occurring on the rising and falling phases of the AP, respectively. These results are consistent with studies using high-speed optical imaging, where sodium influx occurs during the rising phase of the AP (Filipis and Canepari, 2021), whereas calcium influx occurs during the falling phase of the AP in the AIS or AIS-like regions of AP initiation (Pressler and Strowbridge, 2019). Furthermore, we observed consistent results at both room temperature and physiological temperatures with two different sodium-sensitive indicators and two different calcium-sensitive indicators, suggesting that calcium influx occurs

during Ca_V-mediated tail currents on the falling phase of the AP in the axon, regardless of temperature (Kawaguchi and Sakaba, 2015; Pressler and Strowbridge, 2019; Rowan et al., 2014; but see Sabatini and Regehr, 1996). Nevertheless, calcium influx, as assayed with synthetic indicators, could not be blocked completely with Ca_V antagonists. This may be due to several issues, including incomplete block of $Ca_V2.3$, or R-type calcium channels, so named for their resistance to antagonist block. Indeed, careful pharmacological studies across cell classes have shown that $Ca_V2.3$ channels in pyramidal cells are particularly resistant to block by SNX-482 (Sochivko et al., 2002). Furthermore, block of Ca_Vs by peptide toxins can have relatively slow kinetics (McDonough et al., 1996), and while we made every effort to allow for equilibration, with application times exceeding 20 min, this may not have been sufficient for complete block. Regardless, the kinetics of AIS calcium transients, observed here and in other reports (**Fig. 3.1**, **Fig. 3.2**, Pressler and Strowbridge, 2019), are most consistent with influx predominantly through Ca_Vs.

Despite substantial advances in the specificity and selectivity of Ca_V antagonists in recent years, pharmacology remains an imperfect tool to fully understand the mechanisms underlying calcium entry at the AIS. Fortunately, the K1422E variant of $Na_V1.2$ provided the perfect complementary test bed to understand how calcium influx kinetics change as the ion selectivity of Na_V changes. We observed that calcium influx occurred earlier, during the initial depolarization of the AP, in the proximal AIS, an area where $Na_V1.2$-p.K1422E channels are expressed. At the same time, calcium influx timing was not altered in the distal AIS, where NaV1.6 channels with unaltered permeability dominate. The clear differences in timing of calcium influx between the proximal and distal AIS in neurons from $Na_V1.2^{E/+}$ mice neatly recapitulate the differences seen in timing of sodium and calcium influx onsets. In this way, $Na_V1.2$-p.K1422E serves as a positive control of sorts, showing conclusively that sodium and calcium onset timings would overlap if Na_Vs in the AIS fluxed calcium under typical conditions.

3.5 Figures
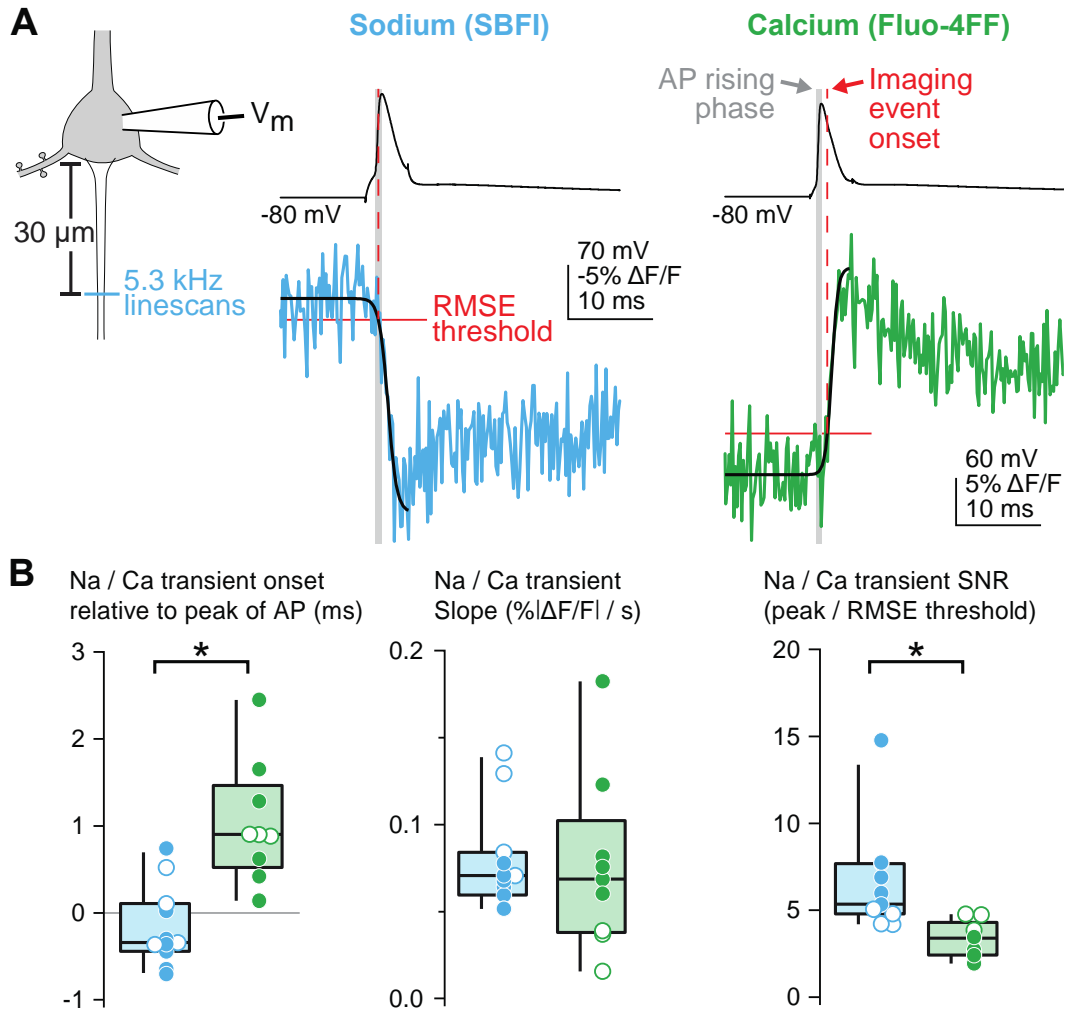
Figure 3.1 Fast linescan imaging reveals distinct temporal profiles of sodium and calcium influx.

A. Schematic of fast linescan protocol. Left: Linescan imaging was performed transecting the AIS at 5.3 kHz with either the sodium dye SBFI or the calcium dye Fluo-4FF. Middle: representative example of sodium influx aligned to soma-evoked AP shows that sodium influx begins during the rising phase of the AP. Right: representative example of calcium imaging aligned to AP. Calcium influx occurs during AP repolarization. Blue, SBFI; green, Fluo-4FF. Dashed vertical red line indicates imaging event onset. Gray bar represents rising phase of the AP (threshold to peak). Black line is the sigmoid fit of the linescan. Solid red line shows baseline noise of the linescan.

B. Comparison of sodium and calcium transient onset time, slope, and signal-to-noise ratio. Left: summary of the timing of sodium and calcium transients relative to the peak of the AP. Negative values represent transient onset that precedes the AP peak. Middle: The slope of optically-recorded sodium and calcium transients. Slope was calculated using the sigmoid fit. Right: signal-to-noise ratio for sodium and calcium transients. Circles represent individual cells. Open circles are cells with similar signal-to-noise ratios. Blue, SBFI; green, Fluo-4FF.
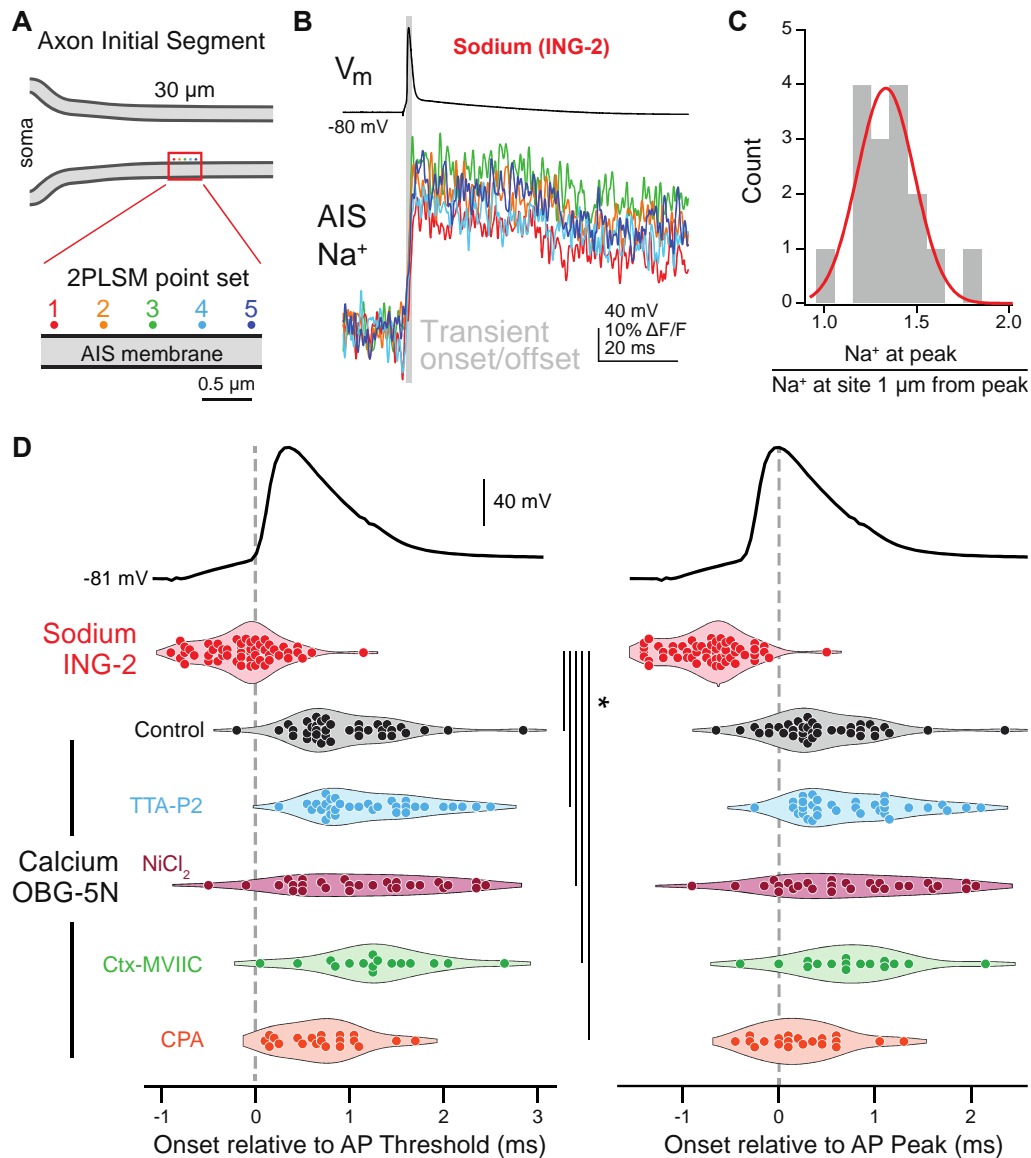
Figure 3.2 Sodium and calcium influx occur on the rising and falling phases of the AP at near-physiological temperatures, respectively.

A. Pointscan imaging protocol was performed as in Figure 4A. OGB-5N was replaced with the sodium indicator ING-2, and Alexa-594 was excluded from the internal recording solution.
B. Representative ING-2 sodium imaging pointset. Points are color-coded as in Panel A. Gray bar indicates the sodium transient onset and offset.
C. Distribution of sodium imaging point sets calculated as in Fig 4C. Red line represents the fit of a normal distribution to the data.
D. Sodium and calcium transients from pointscan imaging temporally-aligned to AP threshold and peak. Left: Sodium and calcium influx onset relative to AP threshold. Right: Sodium and calcium influx onset relative to AP peak. Transient onset time was measured for the brightest point in a point set. Circles are individual point sets. Gray dashed line shows AP threshold (left) or peak (right) timing. Red, ING-2 sodium imaging; black, OGB-5N color coded as in Fig. 4. * : p < 0.001, Kruskall-Wallis test with rank-sum post hoc.
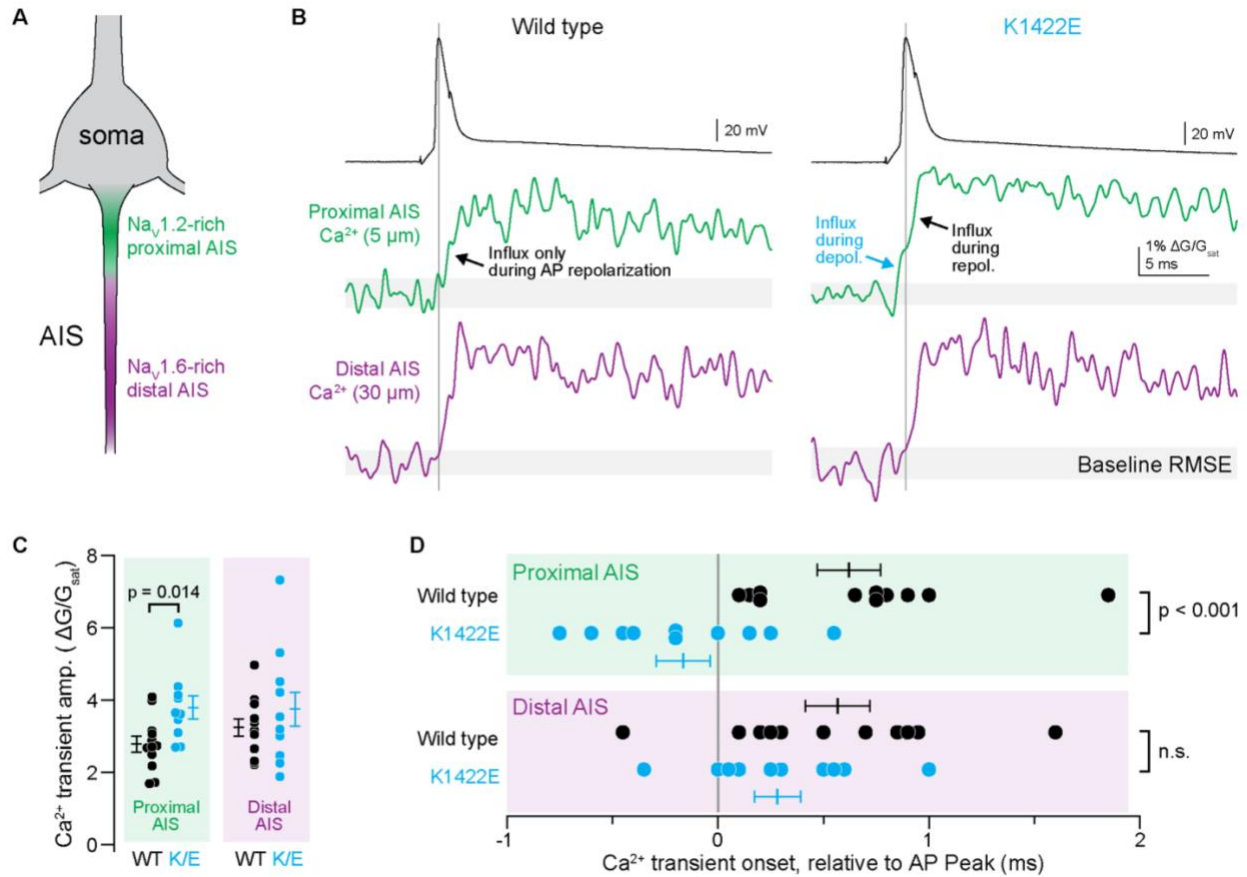
Figure 3.3 AP-evoked Ca2+ influx occurs during the rising phase of the AP in the proximal AIS of Scn2a$^{E/+}$ cells.

A. Pyramidal cell initial segments are enriched with $Na_V1.2$ proximal to the soma and $Na_V1.6$ more distal to the soma. Pointscan imaging was performed 5 and 30 μm from the axon hillock, corresponding to $Na_V1.2$ and $Na_V1.6$-enriched regions, respectively.

B. Examples of AP-evoked (2 nA, 2 ms stimulus; black, top) calcium transients imaged in pointscan mode in the proximal (green, middle) and distal (violet, bottom) AIS in WT (left) and Scn2a$^{E/+}$ cells (right). Vertical line is aligned to peak AP voltage. Gray shaded area encompasses imaging signal root-mean-squared error (RMSE) during baseline, before AP. Consistent deviation above this error value defines onset of Ca^{2+} transient. Note Ca^{2+} influx before AP peak in proximal AIS of K1422E condition only.

C. Amplitude of Ca^{2+} transient is higher in proximal AIS of Scn2a$^{E/+}$ cells, consistent with influx from both local voltage-gated calcium channels and additional influx through K1422E $Na_V1.2$ channels. Circles are single cells and bars are mean ± SEM. P-values from unpaired t-tests.

D. Ca^{2+} transient onset occurs earlier in the proximal AIS of Scn2a$^{E/+}$ cells, consistent with Ca^{2+} influx through K1422E $Na_V1.2$ channels. Display as in (C).
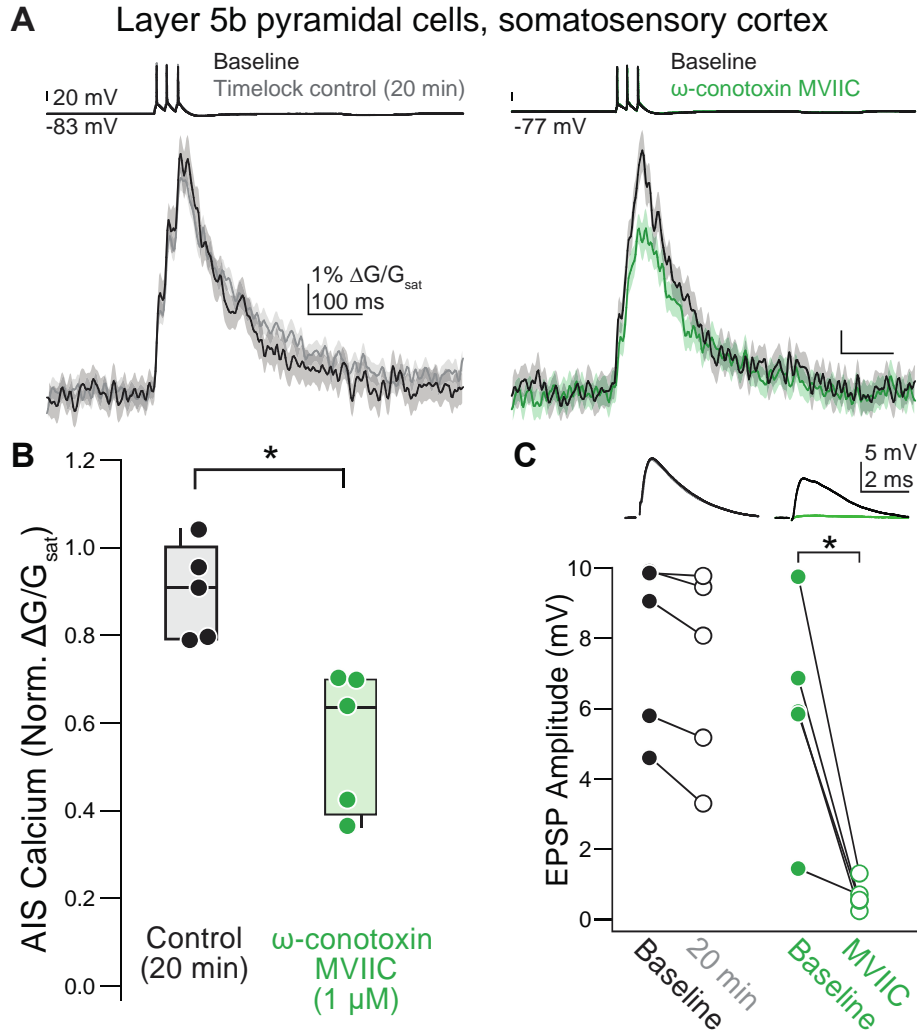
Figure 3.4 Ca$_V$2.1/2.2 contribute to AIS calcium in the somatosensory cortex.

A. Representative effect of ω-conotoxin MVIIC application on AIS calcium in L5b pyramidal cells in the somatosensory cortex. Left: example time-locked control cell. Black, baseline; gray, post. Right: example of the effect of ω-conotoxin MVIIC. Black, baseline; green, ω-conotoxin MVIIC. Linescan data are plotted as mean ± standard error.
B. Summary of the effects of ω-conotoxin MVIIC on AIS calcium in somatosensory L5b pyramidal neurons. Black, time-locked control cells; green, ω-conotoxin MVIIC.
C. Decreases in EPSP amplitude confirm the presence of ω-conotoxin MVIIC at the slice. Top: representative examples of EPSPs in w-conotoxin MVIIC (right) or in time-locked control cells (left). Bottom: Summary of the effects of ω-conotoxin MVIIC on EPSP amplitude in somatosensory cortex. Black, baseline; gray, time-locked control; green, ω-conotoxin MVIIC.

3.6 Tables

Table 3.1 Changes in action potential waveform properties across the course of recording.

* denotes a p-value < 0.05. One-way ANOVAs or two-tailed t-tests were performed for each waveform property, as appropriate. Paired t-tests were performed for EPSP amplitudes.

	Δ V$_m$ (mV)	Δ V$_{threshold}$ (mV)	Δ AP half-width (% baseline)	Δ AP peak (mV)	Δ rheobase (pA)	n	Baseline EPSP (mV)	Post-drug EPSP (mV)
S1 time-lock control	0.46 ± 0.96	-3.09 ± 2.07	96 ± 4	-2.57 ± 1.68	-8.33 ± 14.43	3	7.8 ± 2.5	7.2 ± 2.8
S1 conotoxin MVIIC	0.58 ± 2.57	-1.04 ± 1.84	98 ± 7	-6.09 ± 5.48	0 ± 86.60	3	6.0 ± 3.0	0.7 ± 0.4 *

3.7   References

Antón-Fernández, A., Rubio-Garrido, P., DeFelipe, J., and Muñoz, A. (2015). Selective presence of a giant saccular organelle in the axon initial segment of a subpopulation of layer V pyramidal neurons. Brain Struct. Funct. *220*, 869–884.

Bender, K.J., Ford, C.P., and Trussell, L.O. (2010). Dopaminergic modulation of axon initial segment calcium channels regulates action potential initiation. Neuron *68*, 500–511.

Bischofberger, J., Geiger, J.R.P., and Jonas, P. (2002). Timing and efficacy of Ca2+ channel activation in hippocampal mossy fiber boutons. J. Neurosci. *22*, 10593–10602.

Díaz-Rojas, F., Sakaba, T., and Kawaguchi, S.Y. (2015). Ca2+ current facilitation determines short-term facilitation at inhibitory synapses between cerebellar Purkinje cells. J. Physiol. *593*, 4889–4904.

DiGregorio, D.A., Peskoff, A., and Vergara, J.L. (1999). Measurement of action potential-induced presynaptic calcium domains at a cultured neuromuscular junction. J. Neurosci. *19*, 7846–7859.

Filipis, L., and Canepari, M. (2021). Optical measurement of physiological sodium currents in the axon initial segment. J. Physiol. *599*, 49–66.

Hanemaaijer, N.A.K., Popovic, M.A., Wilders, X., and Grasman, S. (2020). Ca2+ entry through NaV channels generates submillisecond axonal Ca2+ signaling. Elife *9*.

Kawaguchi, S. ya, and Sakaba, T. (2015). Control of inhibitory synaptic outputs by low excitability of axon terminals revealed by direct recording. Neuron *85*, 1273–1288.

Kole, M.H.P., Letzkus, J.J., and Stuart, G.J. (2007). Axon initial segment Kv1 channels control axonal action potential waveform and synaptic efficacy. Neuron *55*, 633–647.

Kole, M.H.P., Ilschner, S.U., Kampa, B.M., Williams, S.R., Ruben, P.C., and Stuart, G.J. (2008). Action potential generation requires a high sodium channel density in the axon initial segment. Nat. Neurosci. *11*, 178–186.

Leterrier, C. (2018). The axon initial segment: an updated viewpoint. J. Neurosci. *38*, 1922–17.

Lorincz, A., and Nusser, Z. (2008). Cell-type-dependent molecular composition of the axon initial segment.

J. Neurosci. *26*, 7172–7180.

McDonough, S.I., Swartz, K.J., Mintz, I.M., Boland, L.M., and Bean, B.P. (1996). Inhibition of calcium channels in rat central and peripheral neurons by omega-conotoxin MVIIC. J. Neurosci. *16*, 2612–2623.

Nakamura, Y., Harada, H., Kamasawa, N., Matsui, K., Rothman, J.S., Shigemoto, R., Silver, R.A., DiGregorio, D.A., and Takahashi, T. (2015). Nanoscale distribution of presynaptic Ca2+ channels and its impact on vesicular release during development. Neuron *85*, 145–158.

Pressler, R.T., and Strowbridge, B.W. (2019). Functional specialization of interneuron dendrites: Identification of action potential initiation zone in axonless olfactory bulb granule cells. J Neurosci *39*, 9674–9688.

Rose, C.R., Kovalchuk, Y., Eilers, J., and Konnerth, A. (1999). Two-photon Na+ imaging in spines and fine dendrites of central neurons. Pflügers Arch - Eur J Physiol *439*, 201–207.

Rowan, M.J.M., Tranquil, E., and Christie, J.M. (2014). Distinct Kv channel subtypes contribute to differences in spike signaling properties in the axon initial segment and presynaptic boutons of cerebellar interneurons. J. Neurosci. *34*, 6611–6623.

Sabatini, B.L., and Regehr, W.G. (1996). Timing of neurotransmission at fast synapses in the mammalian brain. Nature *384*, 170–172.

Santana, L.F., Gómez, A.M., and Lederer, W.J. (1998). Ca2+ flux through promiscuous cardiac Na+ channels: Slip-mode conductance. Science (80-.). *279*, 1027–1033.

Sochivko, D., Pereverzev, A., Smyth, N., Gissel, C., Schneider, T., and Beck, H. (2002). The CaV2.3 Ca2+ channel subunit contributes to R-Type Ca2+ currents in murine hippocampal and neocortical neurones. J. Physiol. *542*, 699–710.

Spratt, P.W.E., Alexander, R.P.D., Ben-Shalom, R., Sahagun, A., Kyoung, H., Keeshen, C.M., Sanders, S.J., and Bender, K.J. (2021). Paradoxical hyperexcitability from NaV1.2 sodium channel loss in neocortical pyramidal cells. Cell Rep. *36*, 109483.

Chapter 4 GABA synapses at the axon initial segment depolarize action potential threshold across adolescent development via shunting inhibition

4.1 Abstract

Chandelier cells are a class of parvalbumin-positive, GABAergic interneurons that uniquely target the axon initial segment of pyramidal neurons in the cortex, amygdala, and hippocampus. Based on their dense and overlapping innervation of pyramidal neurons and their privileged access to the site of action potential generation, these neurons are well-poised to provide a strong inhibitory "veto" of pyramidal neuron firing. However, the postsynaptic effects of chandelier cell input are not uniformly inhibitory throughout life. Unlike most compartments, where GABA responses switch from depolarizing to hyperpolarizing in early life, the axon initial segment shows a delayed developmental profile, with GABA responses remaining depolarizing through adolescence before switching to the typical hyperpolarizing response in adolescence. This delayed switch has been shown to occur through regulation of chloride transporters and is specific to the axon initial segment. However, the functional consequences of this switch on pyramidal neuron firing remains unclear. Additionally, the involvement of these chandelier cell inputs in generating cortical oscillations across adolescence is not well understood.

To understand how chandelier cell inputs affect the functional output of pyramidal neurons across developmental conditions, we performed whole-cell patch-clamp recording from Layer 2/3 pyramidal neurons in *ex vivo* slices of mouse prefrontal cortex and used GABA iontophoresis to target specific neuronal compartments. To mimic different developmental stages, we manipulated the chloride concentration of the intracellular recording solution to yield different GABA reversal potentials. We show that GABA applied to the axon initial segment depolarizes action potential threshold and delays action potential onset, a net inhibitory effect on pyramidal neuron output. This effect depends on shunting inhibition under both adolescent- and adult-like GABA reversal potential conditions. In the adolescent-like condition, however, depolarization-mediated reductions in sodium channel availability also contribute to changes in action potential threshold. These results reveal the mechanism by which chandelier cells provide

an inhibitory "veto" across the range of GABA polarity observed in normal adolescent development, providing a platform for deepening our understanding of these enigmatic cells' circuit function.

4.2 Introduction

Chandelier cells are a class of parvalbumin-positive, GABAergic interneurons in the prefrontal cortex that exclusively target the axon initial segment of pyramidal neurons (Somogyi et al., 1982). Based on this specific synaptic target, chandelier cells have been proposed to orchestrate synchronous activity across a network of pyramidal neurons by providing a powerful "veto" over pyramidal cell firing (Lewis, 2011; Veres et al., 2014). However, the inhibitory nature of this GABAergic synapse has been controversial (Dugladze et al., 2012; Glickfield et al., 2009; Pan-Vazquez et al., 2020; Rinetti-Vargas et al., 2017; Szabadics et al., 2006; Woodruff et al., 2009). In some cell types across brain regions, chandelier cell synapses have an excitatory effect due to a depolarized GABA reversal potential (E_{GABA}) (Khirug et al., 2008; Szabadics et al., 2006; Woodruff et al., 2009, 2006). In other regions, GABA appears to have an inhibitory effect (Dugladze et al., 2012; Glickfield et al., 2009). However, work from our lab suggests that these differences arise from a periadolescent shift in E_{GABA} rather than persistent differences in E_{GABA} across cell types (Rinetti-Vargas et al., 2017).

Complicating matters, differences in the reversal potential of GABA alone do not fully determine whether a particular synapse has an excitatory or inhibitory effect. The effects of GABA are deeply context-dependent, relying on factors like resting membrane potential, the position and timing of the GABA synapse relative to excitatory inputs, and intrinsic membrane conductances of the postsynaptic neuron (Gulledge and Stuart, 2003; Kwag and Paulsen, 2009; Lombardi et al., 2021). Chandelier cell inputs onto pyramidal neurons provide an appealing context to ask questions about the effect of changing E_{GABA}: these inputs display a change in E_{GABA} at a point when other maturational changes are complete (Pan-Vazquez et al., 2020), they have a well-characterized postsynaptic target down to the subcellular level, and by virtue of their specific targeting, they provide an accessible output metric of inhibition: action potential initiation.

The axon initial segment (AIS), the site of action potential generation in L2/3 prefrontal pyramidal neurons (Bender and Trussell, 2012), is exclusively and selectively targeted by chandelier cell synapses (Somogyi et al., 1982). This precise inhibitory contact onto the site of AP initiation has led to the suggestion

that chandelier cells exercise a powerful veto over spiking. However, the precise mechanisms by which GABAergic inputs at the AIS suppress APs have not been fully characterized. The axon initial segment has a varied complement of sodium, potassium, and calcium channels, each of which could respond to GABA-mediated changes in membrane potential to affect AP initiation (Bender and Trussell, 2012). Additionally, previous work in our lab has shown that GABAergic chandelier synapses show a delayed maturational profile in the prefrontal cortex, where the reversal potential of GABA remains elevated beyond the normal early childhood switch and does not hyperpolarize until after adolescence (Rinetti-Vargas et al., 2017). The consequences of this periadolescent shift on AP initiation remain unclear. Does a depolarized E_{GABA} at the AIS lead to excitatory effects on AP generation during adolescence that shift to inhibitory in adulthood?

Here, we used capacitance-compensated GABA iontophoresis and whole-cell electrophysiology to characterize the consequences of AIS GABAergic input on AP properties across developmental E_{GABA} values. We found that GABAergic input to the initial segment, but not proximal dendrite, exerted an inhibitory effect on AP generation across E_{GABA} conditions. This inhibitory effect resulted from shunting inhibition and reduced Na_V availability, which led to an increase in AP threshold and a delay in AP onset. Furthermore, by pushing E_{GABA} beyond the range seen physiologically in L2/3 pyramidal neuron initial segments, we showed that shunting inhibition could be overcome only by pronounced GABA-mediated depolarization. Thus, chandelier cell synapses onto prefrontal pyramidal neurons are uniformly inhibitory across adolescent development, despite undergoing a developmental shift in E_{GABA} across this time period.

4.3   Materials and Methods

Ex vivo electrophysiology and two-photon imaging

All procedures were performed in accordance with University of California IACUC guidelines. C57Bl/6 mice of either sex, aged postnatal day 24–50 were used for all experiments. Mice were anesthetized and acute coronal slices (250 µm) containing medial prefrontal cortex were collected. To preserve neuronal health in layer 2/3 neurons, high-HEPES, low Na^+ solutions were used during slice preparation. Ice-cold HEPES cutting solution contained: 2.5 mM KCl , 1.2 mM NaH_2PO_4, 30 mM $NaHCO_3$, 20 mM HEPES, 5 mM Na^+ ascorbate, 2 mM thiourea, 3 mM Na^+ pyruvate, 25 mM glucose, 10 mM $MgSO_4 \cdot 7 H_20$, 0.5 mM $CaCl_2 \cdot 2 H_20$, and 92 mM NaCl (pH 7.3, 300 mOsm). Slices were then allowed to recover for 15 min at 32-34° C in an N-methyl D-glucamine (NMDG) recovery solution containing 2.5 mM KCl, 1.2 mM NaH_2PO_4, 30 mM $NaHCO_3$, 20 mM HEPES, 5 mM Na^+ ascorbate, 2 mM thiourea, 3 mM Na^+ pyruvate, 25 mM glucose, 10 mM $MgSO_4 \cdot 7 H_20$, 0.5 mM $CaCl_2 \cdot 2 H_20$, and 93 mM NMDG (pH 7.3, 300 mOsm). Following this recovery, slices were allowed to equilibrate in HEPES cutting solution at room temperature for 2 hours before recording. All solutions were bubbled with 5% CO_2/95% O_2.

Whole-cell recordings were made from layer 2/3 pyramidal neurons in prefrontal cortex using Dodt contrast optics. Patch electrodes were pulled from Schott 8250 glass (3-4 MΩ tip resistance) and filled with internal solution. Three different internals were used to calibrate the GABA reversal potential (E_{GABA}) for each experiment. For E_{GABA} = -90 mV experiments, internal solution contained: 113 mM K-gluconate, 9 mM HEPES, 2.25 mM $MgCl_2$, 2.25 mM $MgSO_4$, 10 mM sucrose, 14 mM $Tris_2$-phosphocreatine, 4 mM Na_2-ATP, 0.3 Tris-GTP, and 0.1 µM EGTA. For E_{GABA} = -50 mV experiments, internal solution contained: 102 mM K-gluconate, 11 mM KCl, 9 mM HEPES, 4.5 mM $MgCl_2$, 10 mM sucrose, 14 mM $Tris_2$-phosphocreatine, 4 mM Na_2-ATP, 0.3 Tris-GTP, and 0.1 µM EGTA. For E_{GABA} = -4 mV experiments, internal solution contained: 113 mM KCl, 9 mM HEPES, 4.5 mM $MgCl_2$, 10 mM sucrose, 14 mM $Tris_2$-phosphocreatine, 4 mM Na_2-ATP, 0.3 Tris-GTP and 0.1 µM EGTA. For all internal solutions, pH was 7.2-7.5 and osmolarity was adjusted to ~290 mOsm. To visualize the AIS with two-photon imaging, all internals

were supplemented with 20 µM Alexa-594. After whole-cell configuration was achieved, cells were allowed to equilibrate for at least 5 minutes to allow whole-cell dialysis of the internal solution.

Electrophysiological data were acquired using a Multiclamp 700B amplifier (Molecular Devices) and custom routines written in IgorPro (Wavemetrics). Data were acquired at 50 kHz and filtered at 20 kHz. APs were generated with somatic current injection and injection current amplitude was calibrated to be just-suprathreshold. Briefly, somatic current step amplitude was adjusted in 100 pA increments until the minimum value where APs were reliably generated could be found. AP threshold was defined as the voltage at which dV/dt exceeded 15 mV/ms. AP onset was defined as the time at which threshold was reached after the start of the current injection. To eliminate electrode drift within the slice, all recordings were made using a quartz electrode holder. Cells were excluded if series resistance exceeded 20 MΩ. Data were corrected *post hoc* for junction potential as follows: E_{GABA} = -90 mV, 12 mV; E_{GABA} = -50 mV, 8 mV; E_{GABA} = -5 mV.

GABA iontophoresis was performed using parafilm-wrapped borosilicate pipettes (0.5-µm tips, 1 M GABA in H_2O [pH 4]) placed in proximity to neurites visualized with two-photon laser-scanning microscopy. Two-photon laser-scanning microscopy was performed as previously described (Bender and Trussell, 2009). Briefly, a Coherent Ultra II laser or Mira 900 laser was tuned to 800 nm, and Alexa-594 was visualized with R9110 photomultiplier tubes positioned to capture epifluorescence (<660 nm light, no bandpass) and transfluorescence (535/150 bandpass, Semrock) through a 40x, 0.8 NA objective paired with a 1.4 NA oil immersion condenser (Olympus). After placement near the neurite of interest, GABA was released onto the neurite using an iontophoresis amplifier with pipette capacitance compensation circuitry (MVCS-C, npi electronic, Germany) (30-400 nA application current, -40 nA retention current, 2 ms pulses). This amplifier reduces spatial spread and temporal duration of GABA iontophoresis to allow synaptic-like release of GABA. E_{GABA} was confirmed for each cell in voltage-clamp. Experiments were performed in the presence of CGP55845 (10 µM) to block $GABA_B$ receptors.

Chemicals

SR95531, CGP55845, and XE991 were from Tocris Bioscience. TTA-P2 was from Alomone Labs. Alexa Fluor 594 was from Invitrogen. All other chemicals were from Sigma.

Statistics

Unless otherwise specified, all data are reported as medians with interquartile ranges (IQR) in text and displayed with box plots showing the median, quartiles, and 10%/90% tails). *n* denotes number of cells. Sample sizes were chose based on standards in the field. No assumptions were made about data distributions, and unless otherwise noted, two-side, rank-based nonparametric tests were used. Significance level was set for an α value of 0.05. Holm-Sidak correction was used for multiple comparisons when appropriate. Statistical analysis was performed using Igor 8.0.

4.4   Results

Axonal GABAergic input leads to failures in AP initiation across E_{GABA} values

An individual chandelier cell extends cartridges of boutons along the axon initial segment (AIS) of hundreds of pyramidal neurons in the prefrontal cortex, prompting theories that chandelier cells may synchronize activity across the prefrontal cortex through a "veto" power over pyramidal neuron firing (Schneider-Mizell et al., 2021; Somogyi et al., 1982). While chandelier cells are positioned to provide strong inhibitory control over action potential (AP) initiation in prefrontal pyramidal neurons, the delayed shift in GABA reversal potential (E_{GABA}) at the AIS of their postsynaptic contacts suggests that this connection may instead be excitatory in early adolescence (**Fig. 4.1A**). To understand how GABAergic inputs influence AP generation, we performed whole-cell *ex vivo* electrophysiology combined with GABA iontophoresis to probe AP probability in the absence and presence of GABA in L2/3 pyramidal neurons in prefrontal cortex from mice aged (P24–P50). To precisely control E_{GABA} throughout each recorded neuron, we altered the intracellular chloride concentration in the patch pipette, as $GABA_A$ receptors allow the passage of Cl^- (and to a lesser extent HCO_3^-) ions into the cell (Blaesse et al., 2009). We set E_{GABA} based on values measured in early adolescence (-50 mV) and adulthood (-90 mV) (Rinetti-Vargas et al., 2017). Neurons were filled via whole-cell dialysis with either the E_{GABA} = -90 mV or the E_{GABA} = -50 mV internal solution, both containing the dye Alexa Fluor 594 to allow for morphological identification of the AIS. The AIS was identified by its placement opposite the apical dendrite and its lack of spines. To bypass the presynaptic cell and focus on the postsynaptic effects of altering E_{GABA}, we delivered GABA via an iontophoretic pipette placed 20-30 µm from the soma, which corresponds to the site of AP initiation in these neurons (**Fig. 4.1*B***). Traditional GABA iontophoresis generates GABA responses that last hundreds of milliseconds and with poorly-characterized spatial spread. This impedes efforts to understand the effects of synaptically-released GABA, whose temporal and spatial spread are much narrower in comparison. To increase the speed and reduce the spread of GABA release in this study, we utilized an iontophoretic amplifier that allows for pipette capacitance compensation. Using this system, GABA release was spatially and temporally restricted

compared to traditional GABA iontophoresis (**Fig. 4.1***C*). While still slower than synaptic GABA release, this set-up offered an advantage over paired recordings between one chandelier cell and one pyramidal cell by allowing us to mimic the more physiological effect of several chandelier cell synapses impinging on a single AIS. To compare AP generation with and without GABA, two APs were evoked by minimal-stimulation somatic current injection (0.6 – 2.5 nA, 5 ms duration, 400–500 ms inter-AP interval). A GABA postsynaptic current (PSC) was evoked via iontophoresis during the second AP (**Fig. 4.1***D*). To ensure the maximum effect of GABA application, the relative timing of GABA and the second AP were calibrated so the AP occurred simultaneously with the peak amplitude of the GABA PSC.

When the iontophoretic pipette was placed at the AIS and E_{GABA} was set to -90 mV, as seen in the mature AIS, GABA suppressed AP generation (**Fig. 4.1***E-F*). We next tested the effects of immature, depolarized E_{GABA}. As cells rested near -80 mV, we hypothesized that AIS GABA would increase excitatory drive and lead to increases in AP output. However, we were surprised to find the opposite: AIS GABA reduced AP probability even when E_{GABA} was set to -50 mV (**Fig. 4.1***E-F*). To test if AIS GABA could drive AP generation under strongly depolarizing conditions, we set E_{GABA} to 0 mV, a condition that leads to a non-physiologically strong driving force on Cl^-. In this case, we did observe AP promotion by AIS GABA, as lower currents were needed to evoke APs in with GABA application than without (**Fig. 4.1***E-F*). This confirms that the AP suppression observed with AIS GABA at physiological E_{GABA} was not a product of iontophoresis, but instead reflects a surprising inhibition of AP generation across developmentally-observed E_{GABA} values.

Hyperpolarized and depolarized E_{GABA} at the AIS both increase AP threshold and delay AP initiation
While GABA applied to the AIS does "veto" some APs across physiological E_{GABA} values, the mechanism by which this AP failure occurs may differ across conditions. Given the importance of the AIS in setting the voltage threshold for AP generation (Kole et al., 2008), we hypothesized that AIS GABA decreases AP probability by increasing AP threshold. To determine if AIS GABA application is associated with changes in AP threshold or timing, we compared APs generated in the presence and absence of GABA iontophoresis

in the same three E_{GABA} conditions. Briefly, we increased the somatic stimulation intensity until APs were reliably evoked during GABA iontophoresis. We then measured AP threshold and onset timing with and without GABA application using within-sweep controls to account for changes in series resistance and holding potential over time, which may affect AP threshold. Threshold was determined as the voltage at which the first derivative of voltage with respect for time, dV/dt, exceeded 15 mV/ms (Bean, 2007). AP onset was defined as the time at which AP threshold was reached and was compared to the timing of somatic current injection onset. Changes in threshold and onset were averaged over 5-50 sweeps for each cell.

For GABA iontophoresis onto the initial segment, setting E_{GABA} to -90 mV led to a delay in AP initiation. In control conditions, AP onset occurred 3.64 ms (IQR: 3.46 – 4.21) after the onset of somatic current injection. By contrast, AIS GABA delayed AP onset to 4.28 ms (IQR 4.18 – 4.48) after current injection, a within-sweep median difference of 0.52 ms (IQR: 0.28 – 0.85) (**Fig. 4.2A, D**). AP onset was similarly delayed when E_{GABA} was set to -50 mV. APs without GABA application occurred at 3.68 ms (IQR: 3.49 – 4.08) after current injection and were delayed to 4.15 ms (IQR: 3.674 – 4.3) with GABA (within-sweep median difference = 0.26 ms, IQR: 0.03 – 0.40, **Fig. 4.2A, D**). By contrast, non-physiological E_{GABA}, which promoted rather than suppressed AP generation (**Fig. 4.1**), was associated with an advancement of AP onset, with APs occurring 0.85 ms (IQR: -1.23 – -0.48) earlier with AIS GABA (**Fig. 4.2A, D**).

We next placed the iontophoretic pipette at an equidistant dendrite to determine the effect of basket cell synapses on AP initiation. Basket cells typically target the soma and proximal dendrites of pyramidal neurons (Taniguchi et al., 2013), and unlike chandelier cell synapses, they show a hyperpolarized E_{GABA} early in childhood. Because E_{GABA} is hyperpolarized throughout adolescent development in proximal dendrites, we set E_{GABA} to -90 mV for all experiments with dendritic GABA application. With dendritic GABA, the median within-sweep change in AP onset was 0.32 ms (IQR: 0.17 – 0.46), with control APs reaching threshold at 4.23 ms (IQR: 3.75 – 4.61) after current injection and dendritic GABA AP onset at 4.63 ms (IQR: 4.11 – 4.76) (**Fig. 4.2A, D**).

Next, we examined changes in AP threshold with and without GABA application at the above location/E_{GABA} combinations. For GABA application at the AIS when E_{GABA} was set to -90 mV, median AP threshold across cells shifted from -59.4 mV (IQR: -61.6 – -56.9) without GABA to -57.9 mV (IQR: -59.9 – -54.1) with GABA (**Fig. 4.2B**). Within-sweep changes in AP threshold had a median value of 1.79 mV (IQR: 1.09 – 3.18) (**Fig. 4.2C**). When E_{GABA} was set to -50 mV, AIS GABA application also resulted in an increase in AP threshold, from -54.5 mV (IQR: -56.7 – -52.6) without GABA to -52.1 mV (IQR: -54.9 – -50.7) with GABA (**Fig. 4.2*B***). The median within-sweep change in threshold with E_{GABA} = -50 mV was 1.57 mV (IQR: 0.57 – 3.35) (**Fig. 4.2*C***). 0 mV EGABA again showed a divergent effect, hyperpolarizing AP threshold by 1.78 mV (IQR: -2.36 – -1.23, **Fig. 4.2*B, C***). By contrast, while GABA application to an equidistant dendrite similarly resulted in delayed AP onset and suppression (data not shown), this application did not result in a change in AP threshold (baseline threshold = -56.6 mV, IQR: -57.8 – -55.4; GABA threshold = -56.9 mV, IQR: -57.9 – -55.2, within-sweep median = 0.04 mV, IQR: 0.01 –0.08) (**Fig. 4.2*B, C***).

To ensure that sodium channel availability did not change between APs in the absence of GABA, we quantified the change in threshold and timing in the absence of iontophoresis pulses. The median change in AP threshold without iontophoresis was 0.03 mV (IQR: -0.001 – 0.11) and the median change in AP onset was -0.005 ms (IQR: -0.009 – 0.002502), confirming that sodium channel availability did not change substantially between APs (300-350 ms interstimulus interval) (**Fig. 4.2*C, D***). Next, we confirmed that the effects on threshold and timing were directly due to GABA release by applying the GABA$_A$ antagonist gabazine (SR95531, 10 µM). In the presence of gabazine, AP threshold changes had a median value of 0 mV (IQR: -0.18 – 0.15) and AP onset changed by -0.02 ms (IQR: -0.07 – 0.001) (**Fig. 4.2*C,D***). The complete block of iontophoresis-induced changes in AP threshold and timing by gabazine confirm that these effects are due solely to GABA binding to GABA$_A$ receptors at the AIS and not an artifact of the strong electrical current used to release GABA. The depolarization of AP threshold across physiological E_{GABA} values at the AIS suggests that initial segment GABA has an inhibitory effect on AP initiation across

adolescent development. Additionally, the stability AP threshold when GABA was applied to proximal dendrites highlights the privileged control of AIS GABA over threshold.

Ca_V3 and K_V7 channels do not play a role in AP threshold changes during AIS GABA application

The increases in AP threshold seen with both "mature" and "immature" E_{GABA} values during GABA iontophoresis at the AIS may be a case of convergent outcomes through divergent means: that is, threshold changes with E_{GABA} = -90 mV may occur through a different mechanism than changes with E_{GABA} = -50 mV. For example, while E_{GABA} is depolarized relative to rest in certain avian auditory brainstorm neurons, the high expression of KV1 channels in these neurons means that strongly depolarizing GABAergic input activates KV1 channels and leads to a net inhibitory effect of GABA on AP firing(Al-Yaari et al., 2021). To determine if channels present at the AIS underlie convergent shifts in AP threshold or timing across E_{GABA} values, we quantified the change in AP properties in the presence of selective pharmacological blockers.

K_V7 channels, which underlie the m-current, are present at the AIS and contribute to setting the resting membrane potential and threshold in hippocampal granule cells and prefrontal pyramidal neurons (Hu and Bean, 2018; Martinello et al., 2015). Cholinergic input can shift AP threshold in hippocampal granule cells via Ca-dependent inhibition of axonal K_V7 (Martinello et al., 2015). To determine if a similar mechanism may underlie shifts in AP threshold seen after GABA iontophoresis, we applied the K_V7 antagonist XE991 (10 µM) during the same protocol as described above. If K_V7 channels underlie the shift in AP threshold in either E_{GABA} condition, we would expect to see the change in threshold abolished in the presence of the antagonist. However, GABA continued to alter AP threshold in both cases during XE991 application (E_{GABA} = -90 mV, median change in AP threshold = 3.63 mV, IQR: 1.86 – 5.57; E_{GABA} = -50 mV, median change in AP threshold = 2.05 mV, IQR: 0.70 – 2.83), suggesting that K_V7 channels do not contribute to threshold changes after brief AIS GABA stimulation in these neurons (**Fig. 4.3*A***). Similarly, we saw no alteration in changes in AP onset during XE991 application (E_{GABA} = -90 mV, median change

in AP onset = 0.84 ms, IQR: 0.50 – 1.22; E_{GABA} = -50 mV, median change in AP onset = 0.44 ms, IQR: 0.27 – 1.15, **Fig. 4.3***B*).

Additionally, we examined the role of Ca_V3 channels in AIS GABA-mediated changes in AP threshold and timing. Ca_V3 channels are a class of low-threshold calcium channels found at the AIS in a variety of cell classes (Bender and Trussell, 2009; Bender et al., 2012; Clarkson et al., 2017; Dumenieu et al., 2018; Fukaya et al., 2018; Hu and Bean, 2018; Lipkin et al., 2021; Martinello et al., 2015). These channels activate and inactivate near resting membrane potential and can be relieved from inactivation by membrane hyperpolarization (Huguenard, 1996). As a consequence, small change in membrane voltage can lead to large shifts in Ca_V3 availability. To assess if Ca_V3 channel availability contributes to the observed changes in AP threshold and onset, we blocked Ca_V3 channels with the selective antagonist TTA-P2 (2 µM). As with XE991, TTA-P2 did not block AIS GABA-induced changes in AP threshold (E_{GABA} = -90 mV, median change in AP threshold = 4.85 mV, IQR: 4.55 – 5.26; E_{GABA} = -50 mV, median change in AP threshold = 1.85 mV, IQR: 1.46 – 2.57) or AP onset (E_{GABA} = -90 mV, median change in AP onset = 1.18 ms, IQR: 1.00 – 1.20; E_{GABA} = -50 mV, median change in AP onset = 0.31 ms, IQR: 0.22 – 0.47) in either E_{GABA} condition (**Fig. 4.3***A, B*). In fact, TTA-P2 application with hyperpolarized E_{GABA} led to a small but significant increase in AP threshold and delay in AP initiation (threshold: p = 0.001, onset: p = 0.0019, Mann-Whitney Wilcoxon Test). This is consistent with the observed role of AIS Ca_V3 channels in affecting AP threshold (Bender and Trussell, 2009). (In the absence of GABA iontophoresis, AP threshold was hyperpolarized from -54.4 mV (IQR: -56 – -54.1) to -59.4 mV (IQR: -61.6 – -56.9) by TTA-P2 application alone. Having ruled out the dependence of AIS GABA-mediated AP threshold changes on Ca_V3 and K_V7, we next focused on the role of shunting inhibition in the observed effects.

AIS GABA modulates AP threshold through shunting inhibition across physiological E_{GABA} values
GABAergic inhibition of pyramidal cell firing can occur through two major mechanisms: hyperpolarizing inhibition and shunting inhibition. When hyperpolarizing inhibition occurs, overt decreases in the cell's membrane potential move the cell away from threshold and reduce AP probability. By contrast, shunting

inhibition occurs regardless of changes in membrane voltage. Briefly, GABA binds to $GABA_A$ receptors, increasing the local conductance of the cell and in turn reducing the local input resistance. With a decreased input resistance, current injections or incoming synaptic currents are less effective at changing the membrane voltage. Shunting inhibition can occur across a range of E_{GABA} values and resting membrane potentials but lasts only as long as the GABA postsynaptic current lasts, since the increased conductance following $GABA_A$ receptor opening is short-lived relative to the membrane time constant and the change in membrane potential (Paulus and Rothwell, 2016). Overt changes in membrane potential may accompany shunting inhibition if E_{GABA} is far from the baseline membrane potential and these changes often outlast the shunt. As our pharmacological approaches ruled out several ion channels recruited by changes in membrane potential in GABA-mediated threshold and timing shifts, we sought to understand the role of shunting inhibition in these effects instead.

If shunting inhibition underlies changes in AP threshold, these changes would be predicted to remain at a similar magnitude at regardless of the recorded neuron's holding potential. Conversely, changes in threshold that rely on GABA-mediated changes in membrane potential will increase with increases in the driving force on GABA and decrease with decreases in driving force (**Fig. 4.4B**). To test GABA effects at different holding potentials, we repeated our paired AP protocol as above, but for each sweep, added an additional pair of APs that were generated from a more depolarized resting membrane potential. As before, the second AP of each set occurred during the peak GABA current (**Fig. 4.4A**). When E_{GABA} was set to -50 mV, the driving force (DF) for GABA was lower when the cell was held at -55 mV compared to -85 mV (a decrease in GABA PSP amplitude is visible in **Fig. 4.4A**). Despite this decrease in driving force, however, changes in AP threshold were consistent across holding potentials (high DF: median change in AP threshold = 1.57 mV, IQR: 0.57 – 3.35; low DF: median change in AP threshold = 1.53 mV, IQR: 0.69 – 2.41, **Fig. 4.4C-F**), suggesting that shunting inhibition is a major contributor to AIS GABA-driven changes in AP threshold. A similar pattern was seen when E_{GABA} was -90 mV. Despite the increased driving force on GABA at -65 mV compared to -85 mV, we observed no increase in the AIS GABA-mediated AP threshold change with E_{GABA} at -90 mV (low DF: median change in AP threshold = 1.79 mV, IQR: 1.09 – 3.18; high

DF: median change in AP threshold = 1.82 mV, IQR: 1.48 – 3.10, **Fig. 4.4*C-E, G***). Overall, as changes in AP threshold were consistent across driving force, these changes following GABAergic input to the AIS appear to largely result from shunting inhibition.

Reduced sodium channel availability following depolarizing AIS GABA contributes to GABA-mediated threshold changes

While shunting inhibition appears to play a large role in AIS GABA-mediated changes in AP threshold, it remains possible that membrane depolarization in the "immature" E_{GABA} condition may additionally contribute to threshold changes via alteration of sodium channel availability in the AIS. Na_Vs are found at high density in the AIS, where they are largely responsible for setting AP threshold in pyramidal neurons (Hu et al., 2009; Kole et al., 2008). Similarly to Ca_V3 channels, their activation and inactivation near rest means that small changes in membrane potential can translate to large changes in Na_V availability and therefore AP threshold. However, exploring the role of Na_V pharmacologically is difficult, as interfering with Na_V function necessarily interferes with AP generation, regardless of GABA effects. One elegant tool for exploring the role of Na_V function following depolarizing GABAergic input is to decouple the shunting and depolarizing effects of GABA on AP waveform. Previous work performed in axonal bleb recordings from the substantia nigra demonstrated that depolarizing GABA inputs lead to slower APs via sodium channel inactivation (Kramer et al., 2020). The authors determined that this effect was independent of GABA-mediated shunting by evoking depolarization with direct current injection rather than $GABA_A$ receptor activation. While $GABA_A$ activation was more effective at altering AP height than current injection alone, the comparable effectiveness of GABA application and current injection on reducing AP speed suggested that GABA-mediated depolarization rather than shunting was the main driver of the observed effect on AP speed.

We adopted this approach to quantify the relative contributions of these two actions of depolarizing GABA on AP threshold in our layer 2/3 pyramidal neurons. As in **Fig. 4.4**, pairs of action potentials were evoked from two baseline membrane potentials, with GABA iontophoresis at the AIS occurring during the

second AP of each pair (**Fig. 4.5A**). To correlate the effects of membrane depolarization with changes in AP threshold, we first quantified the difference in membrane potential between both baselines (**Fig. 4.5A**, center). We then measured the difference in AP threshold between the first APs in each pair, which were generated without GABA but from different baseline potentials (**Fig. 4.5A**, right). To compare GABA-mediated changes to those generated by membrane depolarization alone, we also quantified the amplitude of the recorded GABA PSP in both physiological E_{GABA} conditions. This allowed us to plot the ΔV_m against the ΔAP threshold in each condition: current injection alone, "immature" E_{GABA}, and "mature" E_{GABA}. We predicted that pure shunting effects would fall along the y-axis of the resulting plot, as changes in threshold would occur in the total absence of V_m changes. Conversely, we predicted that changes in threshold that resulted from reduced Na_V availability at depolarized V_m would be positively-correlated and fall in the upper righthand quadrant (**Fig. 4.5B**).

When E_{GABA} was set to -90 mV and GABA was applied to the AIS, the GABA-associated change in V_m was minimal, as V_m (-85 mV) was very close to E_{GABA} and driving force was therefore low. However, as we observed a pronounced depolarization of AP threshold, plotting Δthreshold against ΔV_m resulted in points falling along the y-axis, in line with our predictions of shunting inhibition as the primary driver of AP threshold depolarization in "mature" E_{GABA} conditions (**Fig. 4.5C**). In contrast to the purely shunting effect of "mature" E_{GABA}, plotting Δthreshold against ΔV_m in the "immature" E_{GABA} condition revealed a mixed effect of shunting and reductions in Na_V availability, as data points clustered between the vertical axis (a pure shunt) and the line describing Na_V availability changes (**Fig. 4.5C**). In the case of non-physiological E_{GABA}, where GABAergic input to the AIS was capable of promoting AP generation through hyperpolarization of AP threshold (**Fig. 4.1–4.2**), changes in V_m were negatively correlated to changes in AP threshold and the resultant points were found in the bottom right cluster of the graph (**Fig. 4.5C**). Patterns were largely similar when APs were evoked from a more depolarized membrane potential (-65 mV), which differentially altered driving force on GABA in different E_{GABA} conditions (**Fig. 4.5D**). However, rather than falling along the vertical axis, "mature" E_{GABA} data points now were plotted in the upper lefthand axis, indicative of hyperpolarization-mediated inhibition (**Fig. 4.5D**).

To determine if differences existed between E_{GABA} conditions at each baseline V_m, we quantified the above results by measuring the angle of each plotted point to the y-axis (**Fig. 4.5*E***). We found that the vector angle differed significantly between holding potentials for "mature" E_{GABA} (p = 0.0015 , Wilcoxon Ranked-Sum Test), as well as between holding potentials for "immature" EGABA (p = 0.0006 , Wilcoxon Ranked-Sum Test, **Fig. 4.5*F***). In the "immature" E_{GABA} condition, the angle was smaller when driving force was reduced, indicating a stronger, but not completely explanatory, effect of shunting inhibition of the observed changes in AP threshold. Taken as a whole, these data indicate that GABA synapses on the AIS of pyramidal neurons inhibit AP generation across the developmental range of E_{GABA} by depolarizing AP threshold. In immature pyramidal neurons, where E_{GABA} is depolarized relative to resting membrane potential, this effect is achieved through a combination of shunting inhibition and depolarization-mediated reductions in sodium channel availability. By adulthood, when E_{GABA} reaches its mature, hyperpolarized value, shunting inhibition is the dominant mode by which axo-axonic synapses regulate AP initiation.

4.5   Discussion

Here, we show the mechanism by which GABAergic input onto the axon initial segment regulates AP initiation. While E_{GABA} undergoes a developmental switch from depolarized to hyperpolarized in L2/3 neuron initial segments (Rinetti-Vargas et al., 2017), the overall effect of GABA at the AIS is inhibitory across developmental E_{GABA} ranges. This uniformly inhibitory effect of GABA on AP initiation is largely mediated by shunting inhibition, whereby changes in membrane conductance associated with the opening of $GABA_A$ receptors reduce the efficacy of incoming currents to generate APs. The effect of this shunt is a depolarization of AP threshold when GABA is applied to the AIS, as well as a delay in AP onset. Dendritically-applied GABA delays AP onset with no effect on AP threshold, suggesting that AIS GABA (presumably from chandelier cells) is preferentially poised to alter AP properties. Overall, this work provides deeper mechanistic insight into the circuit effects of prefrontal chandelier cells.

Depolarized axonal E_{GABA} leads to inhibitory effects on AP initiation

The axon initial segment is a boundary region in neurons that separates the somatodendritic region from the axonal region while harboring characteristics of both (Bender and Trussell, 2012; Leterrier, 2018). Dendritic E_{GABA} is almost exclusively hyperpolarized relative to the cell's resting membrane potential, while axonal E_{GABA}, particularly at axonal terminals, is depolarized relative to rest (Price and Trussell, 2006; Ruiz et al., 2010; Turecek and Trussell, 2001; Zorrilla de San Martin et al., 2017). The AIS shows a mixed phenotype, with E_{GABA} depolarized through early adolescence and subsequently switching to hyperpolarized in adulthood (Rinetti-Vargas et al., 2017). GABA's reversal potential is set by the activity of two chloride transporters, NKCC1 and KCC2, which import and export chloride respectively (Blaesse et al., 2009). It has been hypothesized that KCC2 is excluded from the axonal domain, resulting in depolarized E_{GABA} throughout the axon (Báldi et al., 2010; Hedstrom et al., 2008; Szabadics et al., 2006). However, the AIS likely has KCC2 activity in adulthood, as evidenced by its periadolescent switch (Rinetti-Vargas et al., 2017). Thus, the AIS has some properties of both somatodendritic and axonal regions, resulting in intriguing developmental profiles whose functional consequences are explored in this paper.

However, GABA's inhibitory or excitatory effects are not purely governed by E_{GABA}, and work exploring the effect of GABA_A receptors expressed further down the axon highlights how difficult it is to predict the effects of axonal GABA from E_{GABA} alone. In cerebellar Purkinje neuron terminals and hippocampal mossy fiber boutons, E_{GABA} is depolarized relative to resting membrane potential and results in increases in neurotransmitter release via increases in AP-associated bouton calcium influx (Ruiz et al., 2010; Zorrilla de San Martin et al., 2017). At the presynaptic Calyx of Held, however, a depolarized $E_{Glycine}$ does not alter the amplitude of the postsynaptic glutamate response (Price and Trussell, 2006). In the axons of highly-branched midbrain dopamine neurons, GABA's reversal potential is elevated relative to rest, but GABA application or agonism leads to a shortening and slowing of APs due to a combination of depolarization-mediated sodium channel inactivation and shunting inhibition (Kramer et al., 2020). And in L2/3 pyramidal neurons of immature rat somatosensory cortex, chandelier cells can directly generate APs

in their postsynaptic targets via their depolarized E_{GABA} (Szabadics et al., 2006). While E_{GABA} is depolarized in each of these examples, the responses to axonal GABA vary across cell types and synaptic location. Understanding how the geometry of the axon as well as the conductances present in the bouton or along the axon influence AP waveform and transmitter release is crucial to predicting the postsynaptic effects of GABA in a particular cell type.

Membrane potential changes following $GABA_A$ receptor activation may alter the availability of ion channels near the site of GABA input. In the AIS, sodium channels, low-threshold calcium channels, and potassium channels all show some availability at resting membrane potential, suggesting that small, GABA-mediated changes in membrane potential may lead to the opening or closing of these channels that may promote excitation or inhibition. We show that in immature pyramidal initial segments, GABA-mediated depolarization reduces the availability of sodium channels, working in concert with shunting to reduce AP threshold (**Fig. 4.5**). Additionally, our data suggest that K_V7 channels and Ca_V3 channels are not involved in changing AP threshold after GABA input to the AIS in this manner (**Fig. 4.3**). However, this does not rule out the possibility that longer-lasting changes in postsynaptic membrane potential or calcium signaling may occur downstream of these channels. For example, HCN channels, which underlie I_h current, have been shown to contribute to excitatory effects on AP generation following hyperpolarizing IPSPs in CA1 pyramidal neurons (Kwag and Paulsen, 2009). Specifically, IPSPs advanced AP onset by approximately 10 ms when the IPSP occurred on the falling phase of the theta oscillation. While threshold changes were not directly examined in that study, this example shows that GABA may have effects across a range of time courses. Our work here provides mechanistic insight into one slice of that range: the effects on AP threshold and onset. However, it does not preclude the possibility that hyperpolarized and depolarized E_{GABA} have different downstream effects that we have not captured here. In fact, work revealing an adolescent switch in the homeostatic plasticity of chandelier cell synapses suggests that opposing downstream effects of depolarizing and hyperpolarizing GABA must play a role in governing plasticity at this synapse (Pan-Vazquez et al., 2020).

Depolarized E$_{GABA}$ and AIS homeostatic plasticity

In a recent paper, Pan-Vasquez, Wefelmeyer, et al. observe a switch in the direction of homeostatic plasticity at chandelier cell synapses in L2/3 of somatosensory cortex (Pan-Vazquez et al., 2020): when the authors increased network activity in this brain region before the GABAergic switch (P12–P18), they observed a decrease in the number of chandelier cell synapses, while this same manipulation resulted in an increase in chandelier cell synapses during adulthood (P40–P46). Thus, they were able to characterize homeostatic plasticity rules across this developmental switch and showed that different values of E$_{GABA}$ do have different downstream effects. Therefore, it is surprising to see that regardless of E$_{GABA}$ value (within the physiological range, at least), the effect of AIS GABA on threshold is uniformly inhibitory, driving threshold to more depolarized potentials. These differences may result from differences in brain regions between prefrontal and somatosensory cortices. Or they may reflect the fact that changes in AP threshold are not the main driver of homeostatic plasticity at this synapse, and may instead depend on, for example, slower changes in calcium influx (Lipkin and Bender, 2020). In line with this, homeostatic, activity-dependent plasticity of AIS position persists after blockade of APs but disappears with block of calcium channels (Grubb and Burrone, 2010). As more research emerges showing the role of E$_{GABA}$ shifts in governing behaviors from sleep pressure to migraine-related pain (Alfonsa et al., 2022; Paige et al., 2022), the precise consequences of E$_{GABA}$ changes across a range of excitability and plasticity metrics will need to be explored.

Dendritic and axonal GABA provide differential control over AP generation

Basket cells and chandelier cells are two morphologically-distinct classes of parvalbumin-positive interneurons that synapse onto the perisomatic region of pyramidal cells in the prefrontal cortex (Taniguchi et al., 2013). Basket cells provide inhibitory input onto the soma and proximal dendrites, whereas chandelier cells specifically target the axon initial segment (Taniguchi et al., 2013). While parvalbumin-positive interneurons broadly are crucial in orchestrating gamma oscillations (Cardin et al., 2009; Sohal et al., 2009),

the individual roles of basket and chandelier cells in this oscillatory activity have been difficult to disentangle. Here, we show that chandelier cell synapses on the AIS have preferential control over AP threshold, while both dendritic and AIS GABA synapses can alter AP onset. A similar phenotype was observed in dentate granule cells, where somatic application of the $GABA_A$ agonist muscimol resulted in reductions in AP peak amplitude and delays in AP onset without affecting AP threshold (Rojas et al., 2011). In the same cells, muscimol application to the AIS depolarized AP threshold across E_{GABA} values. These differential effects on AP generation translated to alterations in EPSP summation depending on $GABA_A$ receptor location: somatic GABA receptors created a large membrane shunt, which reduced the efficacy of each EPSP in driving the neuron towards threshold, while initial segment GABA receptors raised AP threshold without altering the efficacy of each EPSP. In the gatekeeping dentate gyrus, this effectively raises the number of coincident inputs required to convey information into the hippocampus (Rojas et al., 2011). Further experiments are needed to explore how basket cell and chandelier cell synapses may shape temporal summation in pyramidal cells in the same manner in the prefrontal cortex.
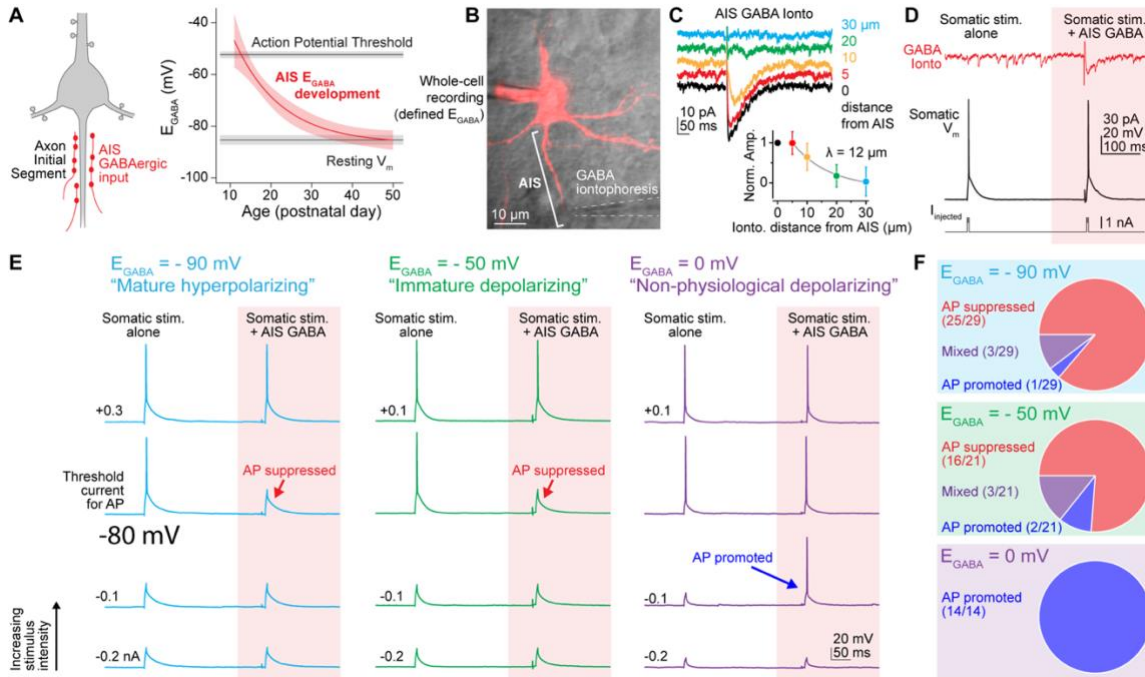
4.6   Figures

Figure 4.1 AIS GABA suppresses AP generation at physiological GABA reversal potentials

A. Left, chandelier cells form GABAergic synapses on the axon initial segment of layer 2/3 pyramidal neurons in prefrontal cortex. Right, the reversal potential of GABA (E_{GABA}) at these synapses follows a periadolescent developmental trajectory, beginning with a depolarized E_{GABA} in early adolescence and reaching a mature, hyperpolarized E_{GABA} by adulthood (P55+).
B. 2PLSM z-stack of a layer 2/3 pyramidal neuron visualized with Alexa Fluor 594. AIS indicated by bracket. An iontophoresis pipette filled with 1M GABA is placed next to the AIS, near the typical site of GABA synapses.
C. Spatial spread of GABA after iontophoresis. The amplitude of GABA PSCs were quantified for different distances of the ionto. pipette from the AIS and fitted with an exponential function. The length constant of GABA spread was 12μm.
D. Schematic of experimental protocol. Action potentials (middle) were generated by minimal-stimulation somatic current injection (bottom). To test the effects of $GABA_A$ receptor activation on AP generation, GABA iontophoresis was used generate a GABA PSC during the second AP. The relative timing of GABA and the second AP were calibrated so the AP occurred simultaneously with the peak amplitude of the GABA PSC.
E. GABA iontophoresis suppresses AP generation at physiological values of E_{GABA}. Somatic stimulation intensity was calibrated to elicit an action potential in both the presence and absence of GABA (top). When stim. intensity was reduced by 0.1 nA, APs occurring with GABA ionto. were suppressed when E_{GABA} was set to -90 mV (left) or -50 mV (center). In the case of E_{GABA} set to 0 mV, reducing stim. intensity resulted in a suppression of the non-GABA AP but a promotion of the GABA AP (right). With a further decrease in stim. intensity, all APs were suppressed across conditions (bottom).
F. The proportion of cells that showed AP suppression, AP promotion, or a combination of both patterns with GABA ionto. across different E_{GABA} values.
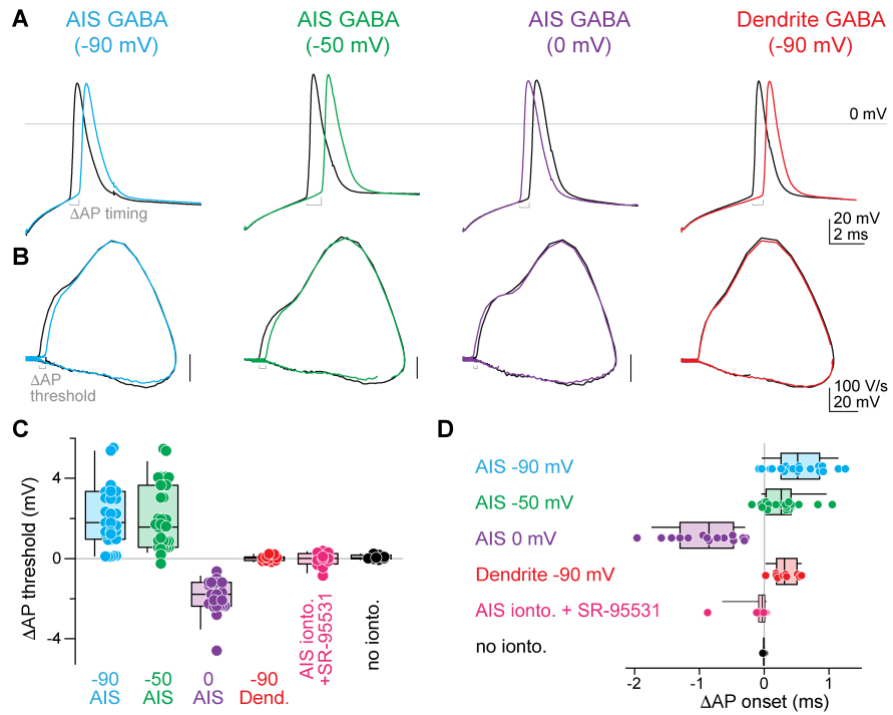
Figure 4.2 GABA alters AP threshold and AP onset differentially across synaptic location

- A. AP onset is altered by GABA application to the AIS or dendrite. Black: APs with no GABA input, color: APs with GABA.
- B. Phase plane plots (dV/dt vs V_m) of APs with and without GABA reveal a location-specific effect of GABA on AP threshold.
- C. Summary of the effects of GABA on AP threshold.
- D. Summary of the effects of GABA on AP onset.
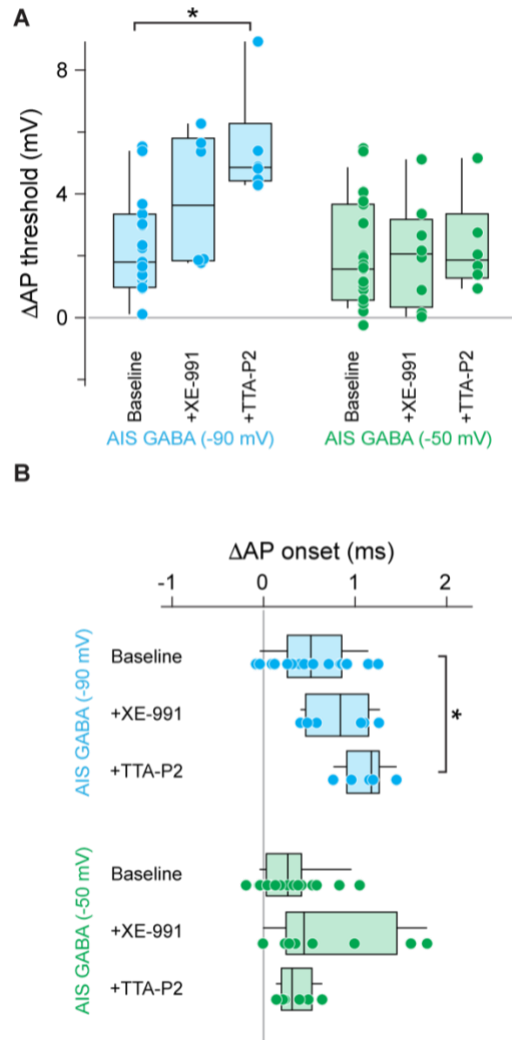
Figure 4.3 AIS GABA effects on threshold and timing are independent of Ca$_V$3 and K$_V$7 channels

A. Summary of the effects of GABA on AP threshold in the presence of different ion channel antagonists. XE-991 was applied at 10 µM concentration; TTA-P2 was applied at 2 µM.
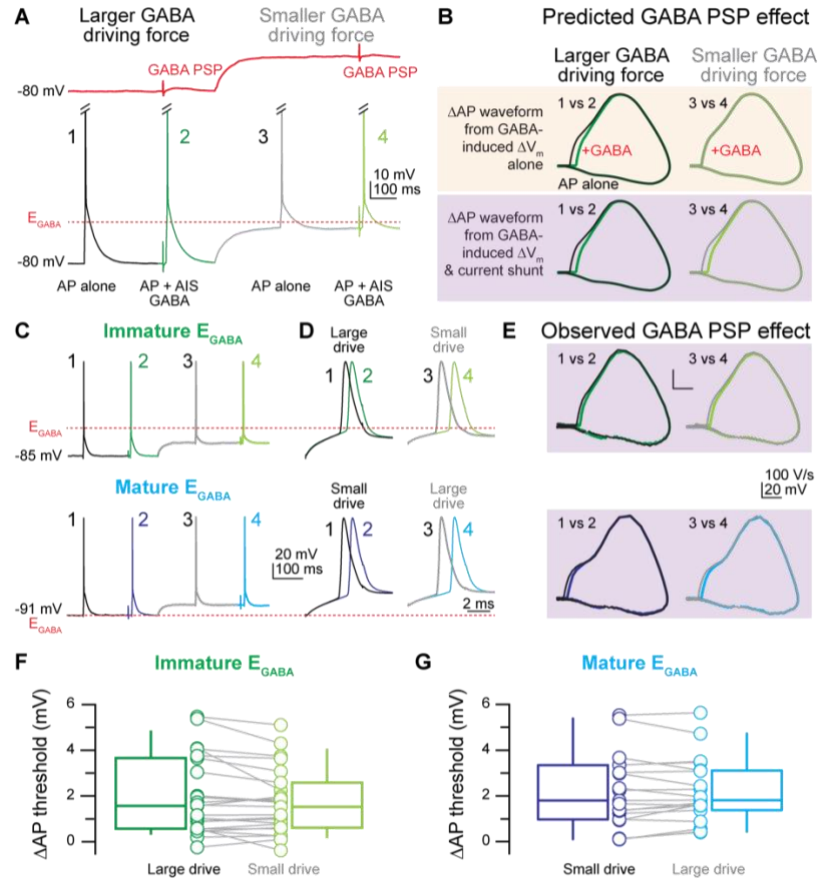B. Summary of the effects of GABA on AP onset in the presence of different ion channel antagonists.

Figure 4.4 GABA depolarizes AP threshold across E_{GABA} values via shunting inhibition

A. Schematic of experimental protocol. GABA PSCs were elicited by GABA iontophoresis onto the AIS (solid red traces) at two different membrane potentials to alter the driving force on GABA according to E_{GABA} (dashed red line). Pairs of action potentials were evoked by somatic current injection at each membrane potential. GABA iontophoresis was delivered during the second AP of each pair. AP threshold was compared between APs generated with and without GABA from the same holding current (i.e. AP 2 (dark green) was compared to AP 1 (black)).

B. Predicted effects of GABA PSP driving force on AP threshold. If GABA-mediated changes in membrane potential underlie changes in AP threshold, reducing the driving force by depolarizing the baseline V_m would be predicted to reduce the change in threshold (yellow, top). If GABA-mediated shunting inhibition underlies changes in AP threshold, the change in threshold would be predicted to stay the same across high and low driving forces (purple, bottom).

C. Top, example APs elicited from a representative neuron with "immature" E_{GABA}. Bottom, example APs elicited from a representative neuron with "mature" E_{GABA}. E_{GABA} for each neuron is represented as a dashed red line.

D. Expanded time base shows AP waveform of spikes elicited with and without AIS GABA at different GABA driving forces. Top, E_{GABA} = -50 mV, bottom, E_{GABA} = -90 mV.

E. Phase plane plots of APs displayed in C and D. Black/gray, without GABA; green/blue, with GABA.

F. Summary of the effects of AIS GABA on AP threshold across different GABA driving forces when E_{GABA} was set to -50 mV. Dark green, high driving force; light green, low driving force.

G. Summary of the effects of AIS GABA on AP threshold across different GABA driving forces when E_{GABA} was set to -90 mV. Dark blue, low driving force; light blue, high driving force.
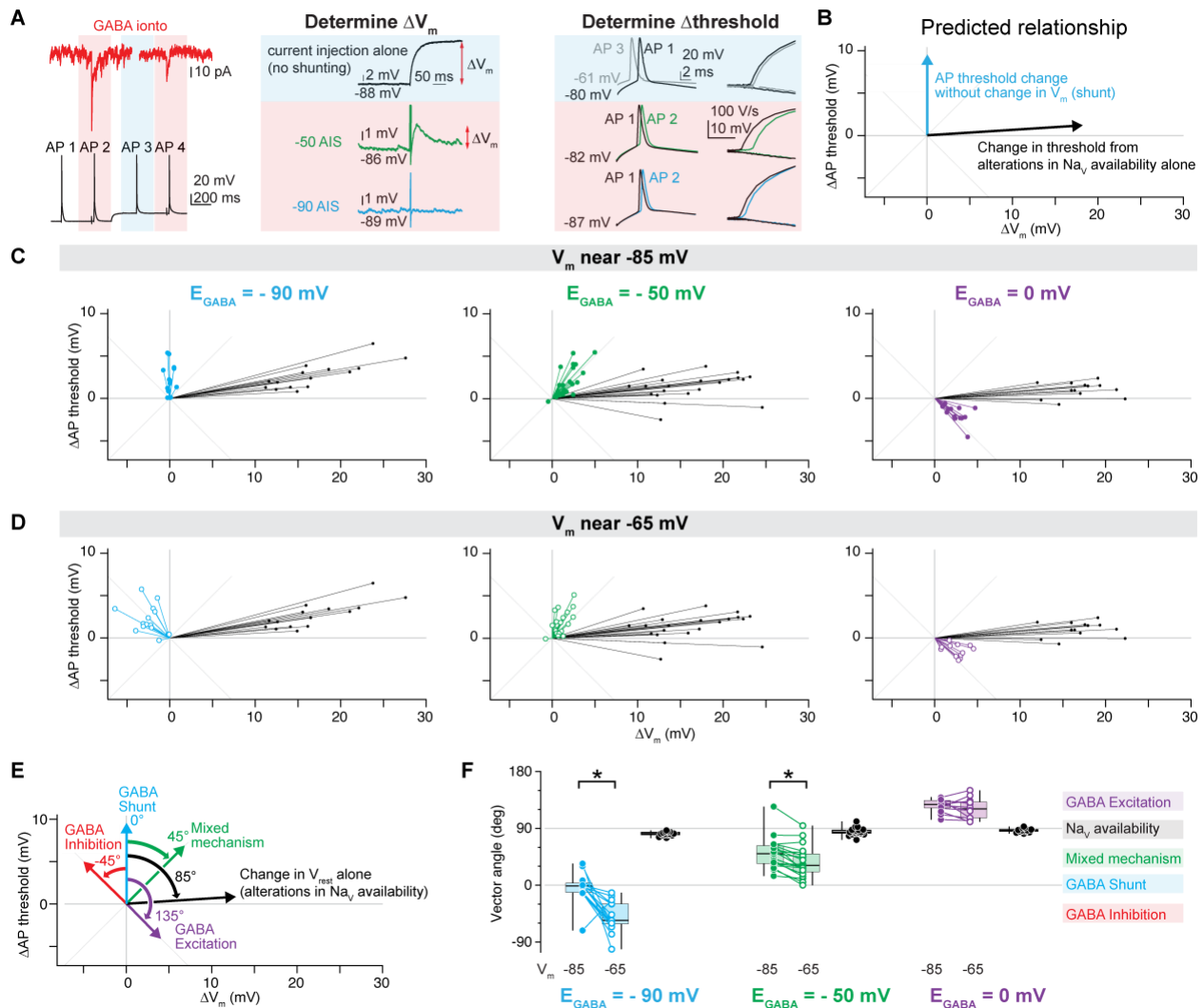
Figure 4.5 Sodium channel availability contributes to GABA-mediated threshold changes

A. Schematic of experimental protocol used to determine the relationship between changes in V_m and changes in AP threshold with and without shunting inhibition. Left, example GABA postsynaptic currents (top, red) recorded from -88 mV (left) and -68 mV (right). Bottom, APs generated from different membrane potentials. Center, depiction of how changes in V_m were calculated for each condition. Note that no change in V_m occurred with -90 mV AIS E_{GABA}. Right, depiction of how changes in AP threshold were calculated for each condition. For current injection alone, AP1 and AP3 (both without GABA) were compared.

B. Predicted relationship between changes in V_m and changes in AP threshold.

C. For neurons held at -85 mV holding potential, changes in AP threshold were plotted against changes in V_m for each condition.

D. For neurons held at -65 mV holding potential, changes in AP threshold were plotted against changes in V_m for each condition.

E. The relationship between ΔV_m and Δthreshold can be quantified by measuring the angle of each point from the y-axis. An 85° angle described Na_V availability changes due to membrane depolarization alone. An angle of 0° is indicative of a pure GABA shunt. Angles near -45° were

considered GABA inhibition. Angles near 135° demonstrated a purely excitatory effect of GABA. Finally, an angle of 45° suggested a mixed mechanism, with some contributions of shunting and some reduction in Na_V availability.

F. For each point in C and D, vector angle from the y-axis was calculated and plotted by condition and by baseline V_m.

4.7 References

Alfonsa, H., Burman, R.J., Brodersen, P.J.N., Newey, S.E., Mahfooz, K., Yamagata, T., Panayi, M.C., Bannerman, D.M., Vyazovskiy, V. V., and Akerman, C.J. (2022). Intracellular chloride regulation mediates local sleep pressure in the cortex. Nature Neuroscience 2022 1–15.

Al-Yaari, M., Onogi, C., Yamada, R., Adachi, R., Kondo, D., and Kuba, H. (2021). Tonotopic specializations in number, size, and reversal potential of GABAergic inputs fine-tune temporal coding at avian cochlear nucleus.

Báldi, R., Varga, C., and Tamás, G. (2010). Differential distribution of KCC2 along the axo-somato-dendritic axis of hippocampal principal cells. European Journal of Neuroscience *32*, 1319–1325.

Bean, B.P. (2007). The action potential in mammalian central neurons. Nature Reviews Neuroscience 2007 8:6 *8*, 451–465.

Bender, K.J., and Trussell, L.O. (2009). Axon initial segment Ca2+ channels influence action potential generation and timing. Neuron *61*, 259–271.

Bender, K.J., and Trussell, L.O. (2012). The physiology of the axon initial segment. Annu Rev Neurosci *35*, 249–265.

Bender, K.J., Uebele, V.N., Renger, J.J., and Trussell, L.O. (2012). Control of firing patterns through modulation of axon initial segment T-type calcium channels. Journal of Physiology *590*, 109–118.

Blaesse, P., Airaksinen, M.S., Rivera, C., and Kaila, K. (2009). Cation-chloride cotransporters and neuronal function. Neuron *61*, 820–838.

Cardin, J.A., Carlén, M., Meletis, K., Knoblich, U., Zhang, F., Deisseroth, K., Tsai, L.H., and Moore, C.I. (2009). Driving fast-spiking cells induces gamma rhythm and controls sensory responses. Nature *459*, 663–667.

Clarkson, R.L., Liptak, A.T., Gee, S.M., Sohal, V.S., and Bender, K.J. (2017). D3 Receptors Regulate Excitability in a Unique Class of Prefrontal Pyramidal Cells. J Neurosci *37*, 5846–5860.

Dugladze, T., Schmitz, D., Whittington, M.A., Vida, I., and Gloveli, T. (2012). Segregation of axonal and network oscillations. Science (1979) *336*, 1458–1462.

Dumenieu, M., Senkov, O., Mironov, A., Bourinet, E., Kreutz, M.R., Dityatev, A., Heine, M., Bikbaev, A., and Lopez-Rojas, J. (2018). The low-threshold calcium channel Cav3.2 mediates burst firing of mature dentate granule cells. Cerebral Cortex *28*, 2594–2609.

Fukaya, R., Yamada, R., and Kuba, H. (2018). Tonotopic variation of the T-Type Ca2+ current in avian auditory coincidence detector neurons. Journal of Neuroscience *38*, 335–346.

Glickfield, L., Roberts, J.D., Somogyi, P., and Scanziani, M. (2009). Interneurons hyperpolarize pyramidal cells along their entire somatodendritic axis. Nat Neurosci *12*, 21–23.

Grubb, M.S., and Burrone, J. (2010). Activity-dependent relocation of the axon initial segment fine-tunes neuronal excitability. Nature 2010 465:7301 *465*, 1070–1074.

Gulledge, A.T., and Stuart, G.J. (2003). Excitatory actions of GABA in the cortex. Neuron *37*, 299–309.

Hedstrom, K.L., Ogawa, Y., and Rasband, M.N. (2008). AnkyrinG is required for maintenance of the axon initial segment and neuronal polarity. J Cell Biol *183*, 635–640.

Hu, W., and Bean, B.P. (2018). Differential control of axonal and somatic resting potential by voltage-dependent conductances in cortical Layer 5 pyramidal neurons. Neuron *97*, 1315-1326.e3.

Hu, W., Tian, C., Li, T., Yang, M., Hou, H., and Shu, Y. (2009). Distinct contributions of Na(v)1.6 and Na(v)1.2 in action potential initiation and backpropagation. Nat Neurosci *12*, 996–1002.

Huguenard, J.R. (1996). Low-threshold calcium currents in central nervous system neurons. Annu Rev Physiol *58*, 329–348.

Khirug, S., Yamada, J., Afzalov, R., Voipio, J., Khiroug, L., and Kaila, K. (2008). GABAergic depolarization of the axon initial segment in cortical principal neurons Is caused by the Na-K-2Cl cotransporter NKCC1. Journal of Neuroscience *28*, 4635–4639.

Kole, M.H.P., Ilschner, S.U., Kampa, B.M., Williams, S.R., Ruben, P.C., and Stuart, G.J. (2008). Action potential generation requires a high sodium channel density in the axon initial segment. Nat Neurosci *11*, 178–186.

Kramer, P.F., Twedell, E.L., Shin, J.H., Zhang, R., and Khaliq, Z.M. (2020). Axonal mechanisms mediating g-aminobutyric acid receptor type a (GABA-A) inhibition of striatal dopamine release. Elife *9*, 1–24.

Kwag, J., and Paulsen, O. (2009). Bidirectional control of spike timing by GABAA receptor-mediated inhibition during theta oscillation in CA1 pyramidal neurons. Neuroreport *20*, 1209–1213.

Leterrier, C. (2018). The axon initial segment: an updated viewpoint. The Journal of Neuroscience *38*, 1922–17.

Lewis, D.A. (2011). The chandelier neuron in schizophrenia. Dev Neurobiol *71*, 118–127.

Lipkin, A.M., and Bender, K.J. (2020). Flipping the switch: Homeostatic tuning of chandelier synapses follows developmental changes in GABA polarity. Neuron *106*, 199–201.

Lipkin, A.M., Cunniff, M.M., Spratt, P.W.E., Lemke, S.M., and Bender, K.J. (2021). Functional microstructure of CaV-mediated calcium signaling in the axon initial segment. Journal of Neurosciences *41*, 3764–3776.

Lombardi, A., Luhmann, H.J., and Kilb, W. (2021). Modelling the spatial and temporal constrains of the GABAergic influence on neuronal excitability. PLoS Comput Biol *17*, e1009199.

Martinello, K., Huang, Z., Lujan, R., Tran, B., Watanabe, M., Cooper, E.C., Brown, D.A., and Shah, M.M. (2015). Cholinergic afferent stimulation induces axonal function plasticity in adult hippocampal granule cells. Neuron *85*, 346–363.

Paige, C., Plasencia-Fernandez, I., Kume, M., Papalampropoulou-Tsiridou, M., Lorenzo, L.E., David, E.T., He, L., Mejia, G.L., Driskill, C., Ferrini, F., et al. (2022). A female-specific role for calcitonin gene-related peptide (CGRP) in rodent pain models. Journal of Neuroscience *42*, 1930–1944.

Pan-Vazquez, A., Wefelmeyer, W., Gonzalez Sabater, V., Neves, G., and Burrone, J. (2020). Activity-dependent plasticity of axo-axonic synapses at the axon initial segment. Neuron *106*, 265-276.e6.

Paulus, W., and Rothwell, J.C. (2016). Membrane resistance and shunting inhibition : where biophysics meets state-dependent human neurophysiology. Journal of Physiology *594*, 2719–2728.

Price, G.D., and Trussell, L.O. (2006). Estimate of the chloride concentration in a central glutamatergic terminal: A gramicidin perforated-patch study on the Calyx of Held. Journal of Neuroscience *26*, 11432–11436.

Rinetti-Vargas, G., Phamluong, K., Ron, D., and Bender, K.J. (2017). Periadolescent maturation of GABAergic hyperpolarization at the axon initial segment. Cell Rep *20*, 21–29.

Rojas, P., Akrouh, A., Eisenman, L.N., and Mennerick, S. (2011). Differential effects of axon initial segment and somatodendritic GABAA receptors on excitability measures in rat dentate granule neurons. J Neurophysiol *105*, 366–379.

Ruiz, A., Campanac, E., Scott, R.S., Rusakov, D.A., and Kullmann, D.M. (2010). Presynaptic GABAA receptors enhance transmission and LTP induction at hippocampal mossy fiber synapses. Nat Neurosci *13*, 431.

Schneider-Mizell, C.M., Bodor, A.L., Collman, F., Brittain, D., Bleckert, A.A., Dorkenwald, S., Turner, N.L., Macrina, T., Lee, K., Lu, R., et al. (2021). Structure and function of axo-axonic inhibition. Elife *10*, 1–39.

Sohal, V.S., Zhang, F., Yizhar, O., and Deisseroth, K. (2009). Parvalbumin neurons and gamma rhythms enhance cortical circuit performance. Nature *459*, 698–702.

Somogyi, P., Freund, T.F., and Cowey, A. (1982). The axo-axonic interneuron in the cerebral cortex of the rat, cat and monkey. Neuroscience *7*, 2577–2607.

Szabadics, J., Varga, C., Molnar, G., Olah, S., Barzo, P., and Tamas, G. (2006). Excitatory effect of GABAergic axo-axonic cells in cortical microcircuits. Science (1979) *311*, 233–235.

Taniguchi, H., Lu, J., and Huang, Z.J. (2013). The spatial and temporal origin of chandelier cells in mouse neocortex. Science (1979) *339*, 70–74.

Turecek, R., and Trussell, L.O. (2001). Presynaptic glycine receptors enhance transmitter release at a mammalian central synapse. Nature 2001 411:6837 *411*, 587–590.

Veres, J.M., Nagy, G.A., Vereczki, V.K., Andrási, T., and Hájos, N. (2014). Strategically positioned inhibitory synapses of axo-axonic cells potently control principal neuron spiking in the basolateral amygdala. Journal of Neuroscience *34*, 16194–16206.

Woodruff, A., Xu, Q., Anderson, S.A., and Yuste, R. (2009). Depolarizing effect of neocortical chandelier neurons. Front Neural Circuits *3*, 1–10.

Woodruff, A.R., Monyer, H., and Sah, P. (2006). GABAergic excitation in the basolateral amygdala. Journal of Neuroscience *26*, 11881–11887.

Zorrilla de San Martin, J., Trigo, F.F., and Kawaguchi, S.Y. (2017). Axonal GABAA receptors depolarize presynaptic terminals and facilitate transmitter release in cerebellar Purkinje cells. J Physiol *595*, 7477–7493.

Chapter 5   Adolescent alcohol consumption does not alter the GABA reversal potential at the axon initial segment

5.1   Abstract

Adolescent alcohol use is accompanied by changes in prefrontal cortex function. These changes are hypothesized to prime individuals towards alcohol use disorder in adulthood. Chandelier cells in prefrontal cortex are one possible target of alcohol's effects. Chandelier cells are a class of parvalbumin-positive interneurons that may contribute to the organization of oscillatory activity in the prefrontal cortex. They display a delayed maturational trajectory due to the actions of chloride transporters at their cellular target, the AIS. Signaling pathways that control chloride transporter function are affected by alcohol intake. Therefore, we explored the effects of adolescent alcohol intake on chloride transporter function in PFC pyramidal neurons by measuring the reversal potential of chandelier cell synapses with and without exposure to alcohol. We found no differences in E_{GABA} after adolescent alcohol consumption, suggesting that chandelier cell polarity is unaffected by alcohol and does not contribute to alterations in PFC-dependent behaviors associated with early alcohol use.

5.2   Introduction

Adolescence is a sensitive period for developing an alcohol use disorder. The anatomical and functional reorganization of the PFC during adolescence leaves the region and the behaviors it supports vulnerable to environmental influences such as alcohol exposure (Spear, 2011). For example, alcohol consumption in adolescence increases the risk of developing an alcohol use disorder later in life sevenfold (Dewit et al., 1991), and one theory about why this may occur posits that alcohol disrupts the normal maturation of the PFC and by doing so, strengthens behaviors that increase propensity to an alcohol use disorder (Witt, 2010). Such disruption of PFC function is evident in deficits in decision-making tasks seen in people with alcohol use disorder (Bechara et al., 2001), and mice who voluntary binge drink in adolescence similarly show impairments in a PFC-dependent working memory task (Salling et al., 2018). This may result from impairments in the ability to generate gamma oscillations, as gamma power is decreased in human subjects with alcohol use disorder (Padmanabhapillai et al., 2006) and is linked to the proper performance of PFC-dependent behaviors in mice (Cho et al., 2015).

Gamma oscillations in the PFC rely on the actions of GABAergic parvalbumin-positive interneurons (Sohal et al., 2009). It has been hypothesized that GABAergic maturation is a rate-limiting step in the maturation of the PFC overall during adolescence (Caballero and Tseng, 2016). In this chapter, I will explore the hypothesis that alcohol-related alterations in chloride transporter function alter GABAergic signaling and contribute to changes in PFC function after adolescent alcohol exposure. Specifically, I hypothesize that these alterations in GABA function will prolong "adolescent-like" PFC function well into adulthood by disrupting the ability to generate gamma oscillations. This hypothesis stems from the observation that in the PFC, reconsolidation of alcohol-related memories activates the PI3K/Akt pathway (Barak et al., 2013). In fact, alcohol consumption itself upregulates the activity of serine/threonine kinase Akt (Laguesse et al., 2016), which can modulate the activity of chloride transporters through the WNK-SPAK/OSR-1 signaling cascade (Alessi et al., 2014; Nishida et al., 2012). By misregulating the WNK-SPAK/OSR-1 signaling cascade, adolescent alcohol exposure could dysregulate chloride

homeostasis at the AIS and lead to disruptions in normal patterning of cortical oscillations in PFC. This modulation of chloride homeostasis at the AIS by the downstream signaling of Akt in the PFC could contribute to the development of alcohol use disorder by preventing the normal development of gamma oscillations and top-down cortical control (Bitzenhofer et al., 2020).

During early development, GABAergic synapses undergo a switch from depolarizing to hyperpolarizing as the activity of chloride transporters NKCC1 and KCC2 shifts to favor chloride extrusion by KCC2. The WNK-SPAK/OSR-1 kinase complex bidirectionally modulates NKCC1 and KCC2 through phosphorylation (Alessi et al., 2014). This complex has been shown to be activated by the PI3K/Akt signaling cascade (Nishida et al., 2012). As Akt is phosphorylated and its activity upregulated by excessive alcohol intake (Laguesse et al., 2016), alcohol could activate this signaling cascade and lead to the dysregulation of neuronal chloride homeostasis and a depolarized GABA reversal potential. Preliminary data in our lab show a specific depolarization of GABA polarity at the AIS but not dendrites in adult animals after chronic adolescent alcohol exposure. However, whether this effect is robust is unclear. The subcellular localization and activity of chloride transporters in adult prefrontal pyramidal neurons has not been well-characterized, and absence or low expression of NKCC1 at the AIS in adulthood could prevent alcohol-related changes in GABA polarity.

To test the hypothesis that adolescent alcohol alters chloride homeostasis at the AIS via the WNK-SPAK/OSR-1 complex, I performed gramicidin-based perforated-patch recordings in Layer 2/3 PFC pyramidal cells in mice after allowing them chronic intermittent access to alcohol during adolescence. In contrast to my preliminary data, I found no effect of adolescent alcohol access on chloride homeostasis at either the AIS or the proximal dendrite. While male and female animals consumed different amounts of alcohol, neither group showed changes in chloride homeostasis after four weeks of alcohol access. Compounding alcohol exposure with two bouts of restraint stress similarly did not alter chloride homeostasis throughout the neuron. Finally, to control alcohol intake across animals, changes in chloride homeostasis were assessed following a two-week vapor-based chronic intermittent alcohol paradigm. However, chloride homeostasis remained consistent, with hyperpolarizing responses to AIS GABA in

adulthood, as seen previously (Rinetti-Vargas et al., 2017). This work rules out alterations in chloride homeostasis as a mechanism by which adolescent alcohol intake alters PFC function to drive alcohol-related changes in behavior.

5.3   Methods

Two-bottle choice drinking paradigm.

Beginning at postnatal day 28, C57BL/6J mice of both sexes were individually housed in temperature and humidity-controlled rooms under a reversed 12-hour light/dark cycle (lights on at 2200 h) with food and water available *ad libitum*. Animal procedures were approved by and conducted in accordance with policies set by the University of California, San Francisco Institutional Animal Care and Use Committee. The intermittent access to 20% alcohol procedure was conducted as previously described (Warnault et al., 2013). Briefly, mice were given 24 hours of access to one bottle of water and one bottle of 20 percent alcohol (v/v in water, diluted from 95% ethanol) concurrently. Concurrent access was given Monday, Wednesday, and Friday, with a 24-hour period alcohol deprivation period between alcohol access sessions (48 hours over the weekend). This paradigm began at P35 and continued for 4 weeks (i.e. 12 drinking sessions). Alcohol intake was monitored for each animal by weighing bottles at the beginning and end of each alcohol session. Animal weight was monitored each week. Alcohol consumption, fluid intake, and alcohol preference were calculated for each mouse. Spill bottles were included in an empty cage on the same rack to account for spill and evaporation.

Restraint stress paradigm.

At P28, at the onset of single-housing, animals were subjected to a restraint stress paradigm. Holes were drilled in 15 mL Falcon tubes to create breathing holes. Each mouse was placed into the Falcon tube head-first and a nitrile glove was placed behind them to prevent the mouse from turning around in the tube. Mice were kept in the tube for one hour and then returned to the home cage. After the twelfth alcohol session, mice were exposed to one more 1 hr bout of restraint stress.

Chronic intermittent exposure paradigm.

Chronic intermittent alcohol exposure was achieved via vapor inhalation as previously described (Becker and Lopez, 2004; Jury et al., 2001). Mice housed in standard mouse cages were placed into Plexiglas vapor chambers (60 x 36 x 60 cm, Plas Labs, Lansing, MI) and exposed to alcohol vapor. Alcohol was vaporized by passage of air through a vaporization stone submerged in 95% ethanol to deliver 19-22 mg ethanol/liter of air at a rate of ~10 L per minute. To ensure all animals reached intoxication and had stable blood alcohol levels, mice in the alcohol group received an intraperitoneal (i.p.) injection of 1.6 g/kg alcohol and 1 mmol/kg pyrazole, an alcohol dehydrogenase inhibitor (Sigma, St. Louis, MO, USA) prior to being placed in the chambers. Mice in the air group also received 1 mmol/kg pyrazole in saline prior to their placement in air exchange chambers. Each alcohol CIE and air exposure session lasted 16 h per day, with animals placed in the chambers at 1700 h, 5 h before the start of the 12 h circadian light phase and removed at 0900 h. Animals received four consecutive days of exposure (Monday through Friday) repeated for a total of two weeks. A longer, 80 h withdrawal occurred from Friday through Monday.

Gramicidin-based perforated patch electrophysiology.

To maintain intracellular chloride concentrations, gramicidin-based perforated patch recordings were performed as described previously (Rinetti-Vargas et al., 2017). Briefly, acute coronal slices (250 µm) containing PFC were collected from P64-70 mice that had undergone the alcohol paradigms described above, in accordance with UCSF IACUC policies. Slices were prepared in high-HEPES and low-sodium solutions as described in Chapter 4.

Gramicidin-based perforated patch recordings were made from PFC Layer 2/3. Pyramidal cells were visualized using Dodt contrast optics and identified based on their shape, laminar position, and the presence of dendritic spines. Gramicidin (final concentration 3 µg/mL) was dissolved in a solution containing 10 mM NaCl, 10 mM K-gluconate, 125 mM KCl, 15 mM HEPES, 1.5 mM $CaCl_2$ and 1 mM $MgCl_2$ and carboxyfluorescein-AM (60 µM, Invitrogen). An aliquot of internal solution lacking gramicidin and carboxyfluorescein-AM was reserved to front-fill recording pipettes (Schott 8250 glass) for 3-6

minutes. Gramicidin-containing internal solution was then used to back-fill the pipette. A Mira 900 laser (800 nm) powered a two-photon microscope that was used to visualize carboxyfluorescein. R9110 photomultiplier tubes were positioned to capture epifluorescence (<660-nm light, no bandpass) and transfluorescence (535/150 bandpass, Semrock) light through a 40x 0.8-NA objective and a 1.4-NA oil-coupled condenser, respectively. An additional photomultiplier tube downstream of a 770-nm longpass filter capture scanning interference contrast images of slice morphology.

After a giga-ohm seal formed, hyperpolarizing current steps (-5 to -50 pA) were applied to monitor the cell's input resistance for 10-30 minutes until appropriate recording conditions were attained (V_m reached steady-state below -80 mV, R_{in} was <400 MΩ, series resistance was 40-80 MΩ). Data were acquired at 20 kHz and filtered at 10 kHz using a Multiclamp 700B amplifier (Molecular Devices) and custom routines written in IgorPro (WaveMetrics).

GABA iontophoresis was performed as described in Chapter 4, with slight modifications: capacitance compensation was not used on the iontophoresis amplifier. Ejection currents ranged from 30-400 nA and retention current was -40 nA. Current duration was 10 ms. Experiments were performed in the presence of CGP55845 (10 µM) to block $GABA_B$ receptors. Experiments were terminated if the cell's membrane ruptured, as determined by sudden increases in IPSP amplitude (due to the high chloride concentration of the perforated patch solution) or if fluorescence redistributed from the cell body into the patch pipette. E_{GABA} was determined using linear interpolation of IPSP amplitude at different membrane potentials.

Statistics.

Alcohol consumption and preference data are reported as means with standard error in figure legends and displayed as mean with standard error. Electrophysiology data is reported and displayed as means with standard deviation in text and figures. For 2BC and CIE experiments, n denotes animals. For electrophysiology experiments, n represents cells. In 2BC experiments, water and alcohol animals were interleaved daily, and an equal number of male and female animals were recorded each week. Data were

assumed to follow a normal distribution and paired and unpaired t-tests were used throughout. Significance level was set for an alpha value of 0.05, and a Holm-Sidak correction was used for multiple comparisons. Statistical analysis was performed using IgorPro 7.0.

5.4 Results

The periadolescent shift in axon initial segment chloride homeostasis is associated with changes in membrane expression and phosphorylation status of the chloride transporters NKCC1 and KCC2 (Rinetti-Vargas et al., 2017). Serine-threonine phosphorylation of these transporters by WNK increases the function of NKCC1 while concomitantly reducing the activity of KCC2, promoting chloride influx into the cell and depolarization of the GABA reversal potential (Alessi et al., 2014). Given the periadolescent shift in E_{GABA} seen in the AIS, which lags far behind the early postnatal switch seen at dendrites in the same neuron, we were curious if the persistence of NKCC1 expression in the AIS in adolescence leads to specific alterations in E_{GABA} at the AIS but not the dendrite following adolescent alcohol intake. Alcohol intake has been shown to upregulate Akt function upstream of the WNK/SPAK pathway (Laguesse et al., 2016), and so to test the effects of adolescent alcohol consumption on the this signaling pathway, we measured the reversal potential of GABA in L2/3 pyramidal neurons in the prefrontal cortex after four weeks of intermittent access to alcohol. To reliably induce high levels of voluntary alcohol consumption in these mice, we used the two-bottle choice paradigm (2BC) (Carnicella et al., 2014; Hwa et al., 2011). During a 24-hour alcohol-access period, animals were given access to two bottles, one containing 20% alcohol (v/v) and the other containing water, presented on alternating sides to control for side preference. Each alcohol access period was interleaved with a 24–48-hour water-only period. Animals received three alcohol-access periods per week, and the experiment had a duration of four weeks, or twelve alcohol sessions total. Alcohol and water consumption were measured by weighing each bottle at the beginning and end of the alcohol-access session. Animals showed robust escalation of alcohol consumption, increasing their drinking from 11.5 g/kg/day during the first week to 16.3 g/kg/day during the fourth (**Fig. 5.1A**).

After four weeks of chronic alcohol exposure, slices containing PFC were prepared from animals who showed a robust escalation in alcohol intake. Because whole-cell recording leads to washout of the intracellular chloride gradient by overpowering endogenous cation chloride transporters, we instead performed gramicidin-based perforated-patch recordings to gain electrical access to recorded neurons

114

without disrupting the intracellular chloride gradient (Rinetti-Vargas et al., 2017). The soma and processes of the recorded neuron were visualized under a two-photon microscope via the addition of carboxyfluorescein-AM to the pipette solution. Once appropriate recording conditions were achieved, an iontophoresis pipette containing 100µM–1M GABA was placed near the AIS or a proximal dendrite. Whenever possible, iontophoresis pipettes were repositioned within the same cell to assess E_{GABA} at both the AIS and a proximal dendrite. Brief (10 ms) pulses of GABA were delivered onto the AIS and the neuron was held at various membrane potentials with constant current injections (**Fig. 5.1B**). E_{GABA} was determined from the linear fit of GABAergic postsynaptic potentials versus membrane potential. In our preliminary cohort of animals, control animals given access to water alone showed hyperpolarized E_{GABA} at the dendrites (average = -83.4 ± 7.2 mV) and at the AIS (-86.1 ± 6.0 mV) (**Fig. 5.1C**). These values, recorded at P62-65, were consistent with the development shift of E_{GABA} at the AIS that occurs during adolescence: E_{GABA} values are typically hyperpolarized at this age. In mice given access to alcohol via the two-bottle choice paradigm, we observed a slight elevation in dendritic E_{GABA} (average = -71.67 ± 2.9 mV). More strikingly, we observed a 30 mV depolarization of E_{GABA} (average = -56 ± 6.9 mV, p = 0.00012 compared to water control AIS) at the AIS in mice that had consumed alcohol starting in adolescence (**Fig. 5.1C**). This elevation resulted in an E_{GABA} that was similar to E_{GABA} levels seen in early adolescence, suggesting that adolescent alcohol exposure may prevent the typical maturation of GABAergic synapses, perhaps through alcohol's actions on the WNK-SPAK signaling cascade.

To confirm these results, we repeated the same two-bottle choice experiments and perforated patch experiments in a new cohort of animals (**Fig. 5.2A**). In the 2BC paradigm, animals escalated their alcohol intake from 14.1 g/kg/day to 20.8 g/kg/day on average, a similar level as seen in the first cohort of animals (**Fig. 5.2B**). They also showed a concomitant increase in their preference for alcohol over water (**Fig. 5.2B**). Homecage control animals showed expected reversal potentials of -83.3 mV (± 8.2) at the dendrite and -77.8 mV (± 10.5) at the AIS (**Fig. 5.2D**) when recorded from P62-68, consistent with previous data (Rinetti-Vargas et al., 2017). Similarly to our pilot data, water controls showed typical hyperpolarized E_{GABA} at both the dendrite and axon (average dendritic E_{GABA} = -78.0 ± 7.2 mV, average AIS E_{GABA} = -70.0 ± 8.2 mV).

However, we were surprised to see that in contrast to pilot data, alcohol-consuming animals showed no elevation in E_{GABA} at the AIS (average = -69.3 ± 12.6 mV) compared to the dendrite (average = -79.3 ± 8.9 mV) (**Fig. 5.2D**).

To understand the discrepancies seen between this data and the pilot data, we examined if sex differences in alcohol consumption or AIS E_{GABA} across groups might explain the lack of alcohol effect. Adolescent female mice have been shown to consume more alcohol in the 2BC paradigm (Joffe et al., 2020). When animals were divided by sex, males and females escalated to similar levels of alcohol consumption (**Fig. 5.3A**) and preference (**Fig. 5.3B**). Consistent with this similarity in behavior, male and female animals showed a similar range of E_{GABA} values across conditions (**Fig. 5.3C-D**). In female homecage controls, E_{GABA} was -82.2 ± 8.9 mV at the dendrite and -76.9 ± 9.9 mV at the AIS; in males, average E_{GABA} was -85.4 ± 9.2 mV at the dendrite and -79.6 ± 15.2 mV at the AIS. Water-drinking controls of both sexes showed slight elevations in E_{GABA} at both locations compared to homecage controls: for female water drinkers, AIS E_{GABA} was -72.9 ± 3.7 mV while dendritic E_{GABA} was -79.2 ± 7.9 mV. For males with access to water alone, AIS E_{GABA} was -67.8 ± 9.9 mV and dendritic E_{GABA} was -77.2 ± 6.9 mV. Finally, females with adolescent alcohol access had a dendritic E_{GABA} of -81.7 ± 7.3 mV and an AIS E_{GABA} of -67 mV ± 12.7 mV. Alcohol-drinking males similarly did not show a change in AIS E_{GABA} with alcohol consumption (AIS E_{GABA} average = -72.8 ± 12.3 mV, dendrite E_{GABA} = -76.2 ± 10.2 mV). Accordingly, these data suggest that changes in E_{GABA} after adolescent alcohol consumption are unaffected by sex. While individual cells showed slightly elevated AIS E_{GABA} relative to dendritic E_{GABA}, none reached the 30 mV shift initially observed in the pilot cohort. We next asked if other factors changed between when the initial pilot data and follow-up data were collected.

One major difference between the pilot cohort and the follow-up cohort was that the pilot cohort was shipped from Jackson Laboratories while the follow-up cohort was bred in-house. Transport can be a stressful experience for rodents (Landi et al., 1982; Olfe et al., 2010; Wallace, 1976), and early-life stress has been shown to downregulate KCC2 expression in the ventral tegmental area, leading to increases in E_{GABA} and an increase in alcohol self-administration (Ostroumov et al., 2016). It is possible that stress and

adolescent alcohol consumption could both be necessary to depolarize AIS E_{GABA} as we had previously observed. To test the role of stress in contributing to E_{GABA} alterations, we exposed animals to two bouts of restraint stress, one occurring one week before the first day they received alcohol, and the other occurring during the last week of alcohol access (**Fig. 5.4A**). Animals who underwent restraint stress did not appear to consume more alcohol than control animals, but this preliminary study is under-powered for this type of statistical analysis (**Fig. 5.4B**). Neither stress alone (water controls) nor stress combined with 2BC alcohol access led to increases in E_{GABA} at either the dendrite or the AIS (**Fig. 5.4C**). These results suggest that KCC2 is regulated differentially by stress in the ventral tegmental area and prefrontal cortex. The data also suggest that transport stress cannot explain the different effects of alcohol in the pilot and follow-up animal cohorts.

Finally, we used another alcohol exposure paradigm to standardize alcohol intake across animals. One difficulty with the 2BC intermittent access paradigm is that animals escalate their alcohol consumption at different rates, and some fail to escalate entirely. It is possible that heterogeneity in alcohol consumption across animals minimized our ability to detect changes in E_{GABA}. While 2BC intermittent access recapitulates the voluntary and binge-like qualities typical of adolescent alcohol intake (Carnicella et al., 2014), using vaporized alcohol in a chronic intermittent exposure (CIE) paradigm provided an opportunity to ensure that all animals received the same amount of alcohol. In this paradigm, animals are placed under reverse light-dark cycle at P28 and exposed to 19-22 mg ethanol/liter of air at a rate of ~10 L per minute vaporized alcohol or air for 16 hours, followed by an 8-hour withdrawal period in the home cage starting at P35. Animals underwent CIE for two weeks, and tissue was collected 24 hours after the last alcohol exposure session to ensure that no alcohol remained in the tissue (**Fig. 5.5A**). As seen with our 2-bottle choice data, dendritic and axonal E_{GABA} continued to be hyperpolarized following alcohol CIE animals (average dendritic E_{GABA} = -80.4 ± 10.3 mV, average AIS E_{GABA} = -75.4 ± 9.6 mV, **Fig. 5.5B-C**). Overall, these data confirm that alcohol delivered during adolescence does not affect E_{GABA} in Layer 2/3 pyramidal neurons in prefrontal cortex.

5.5 Discussion

Adolescent alcohol use has been proposed to lead to changes in prefrontal cortex function that predispose individuals toward alcohol use disorders (Salling et al., 2018; Spear, 2011; Squeglia et al., 2014). In humans, lower age at first drink is associated with an increased risk of alcohol use disorders (Dewit et al., 1991) and as the prefrontal cortex is the last region to develop (Gogtay et al., 2004), alcohol consumption during this period is likely to lead to changes in prefrontal cortex function and even structure (Nixon and Mcclain, 2010). In fact, subjects with alcohol use disorder perform worse on the Wisconsin Card-Sorting Task, a metric of PFC function (Bechara et al., 2001). The maturation of the prefrontal cortex over the course of adolescence is especially noticeable in GABAergic systems, where adolescence is accompanied by changes in postsynaptic GABA receptor subunit composition and excitatory drive onto parvalbumin neurons, which synergistically increase the strength of inhibitory control over PFC function (Caballero and Tseng, 2016). Another remarkable change in GABAergic PFC function occurs specifically at the chandelier-to-pyramidal cell synapse, whose delayed polarity switch (and its functional consequences) has been extensively discussed above (see **Chapter 4**). Based on the incomplete maturation stage of chandelier cell synapses in adolescence, the association between interneuron dysfunction and alcohol use disorder (Joffe et al., 2020), and the malleability of chloride transporters by alcohol-sensitive signaling pathways (Laguesse et al., 2016), we hypothesized that adolescent alcohol would prolong the immature polarity of chandelier cell synapse, with consequences for the ability to generate well-timed AP firing and organize cortical oscillations.

In our pilot data, we found that indeed, adolescent alcohol consumption led to a specific, 30 mV shift in E_{GABA} at the AIS but not the dendrite of Layer 2/3 prefrontal pyramidal neurons (**Fig. 5.1**). However, despite our best efforts, we were unable to replicate these initial observations (**Fig. 5.2**). A multitude of factors may have contributed to the lack of effect we observed, ranging from sex differences in alcohol consumption and E_{GABA} regulation (**Fig. 5.3**), effects of researcher sex on animal behavior (data not shown), stress history of the animals (**Fig. 5.4**), and variability in alcohol consumption across animals (**Fig. 5.5**).

While we explored myriad variables that may have affected the ability to replicate our original data, patch-clamp physiology is an art as well as a science. Inter-researcher variability in cells patched, regional selection, and slice preparation may have been more important in our results that the other factors we investigated, as a postdoctoral scholar in the lab collected the very first data showing an effect of adolescent alcohol on E_{GABA} at the AIS. Similarly, the disruption of the Covid-19 shelter-in-place is hard to quantify and may have altered the environment in the animal facility in such a way that our effects were not replicated. While unsatisfying in terms of understanding how prefrontal function can be altered by adolescent alcohol, these data showing no effect of adolescent alcohol on E_{GABA} in prefrontal cortex are important in ruling out one possible mechanism, allowing alcohol researchers to focus in on other hypotheses with renewed optimism.
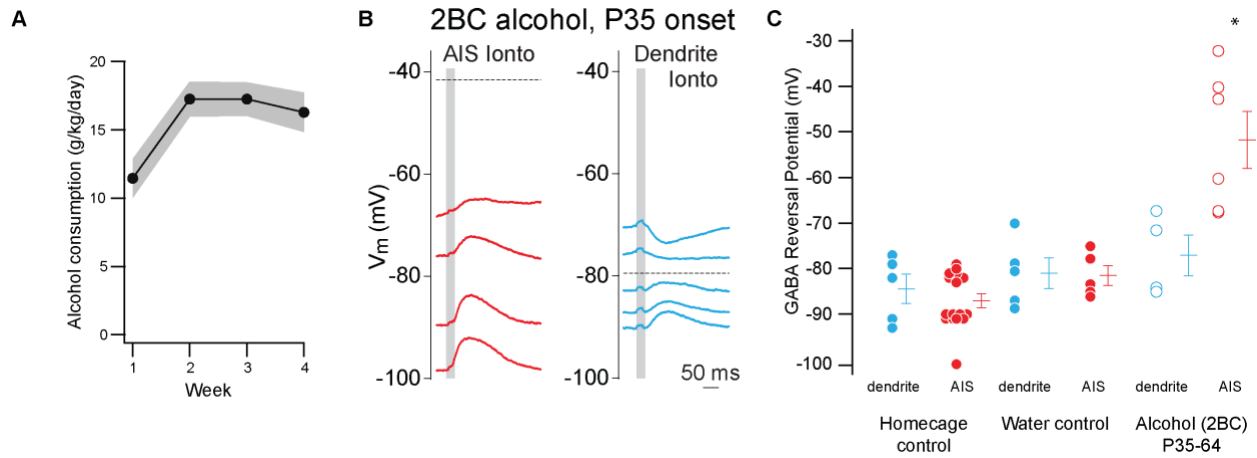
5.6 Figures

Figure 5.1 Preliminary data suggest an effect of adolescent alcohol intake on AIS E_{GABA}

A. Alcohol consumption during two-bottle intermittent access to 20% alcohol.
B. Examples of reversal potentials measured using gramicidin-based perforated patch recordings from an animal given intermittent alcohol access starting at P35. Left (red) shows currents following GABA iontophoresis onto the AIS, right (blue) shows GABA currents following iontophoresis onto the dendrite of the same neuron. Dashed lines indicate the interpolated E_{GABA}. Dark gray bars indicate duration of GABA iontophoresis ejection current.
C. Summary data showing GABA reversal potentials measured in homecage controls, water only animals, and animals given access to alcohol beginning in adolescence. EGABA at the AIS following alcohol access is significantly different than EGABA at the AIS following water access alone (p = 0.00012).
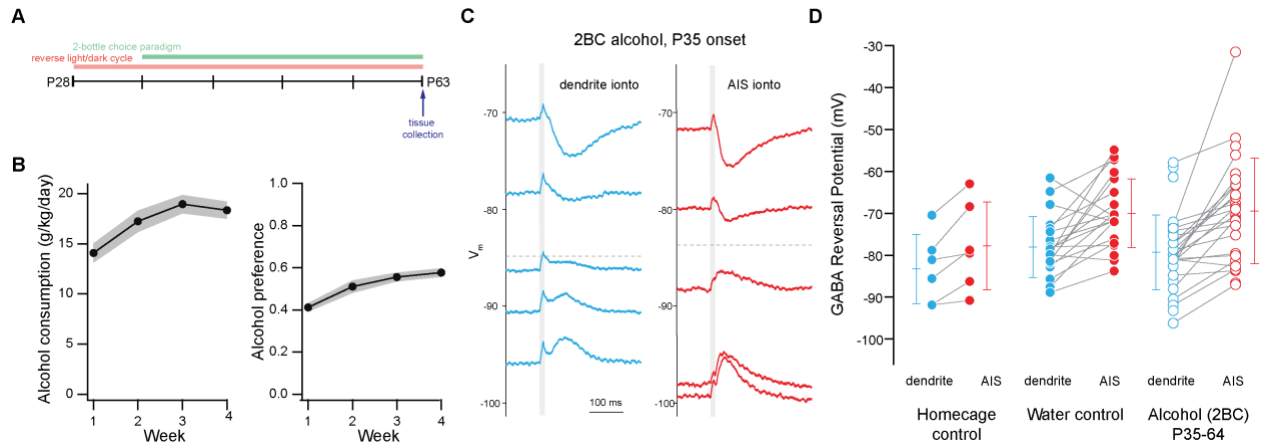
Figure 5.2 Adolescent alcohol intake does not alter E$_{GABA}$ at the AIS

A. Timeline of two-bottle choice intermittent access to 20% alcohol paradigm.
B. Alcohol consumption (left) and preference (right) for animals undergoing the two-bottle choice paradigm.
C. Examples of reversal potentials measured using gramicidin-based perforated patch recordings from an animal given intermittent alcohol access starting at P35. Left (blue) shows currents following GABA iontophoresis onto the dendrite, right (red) shows GABA currents following iontophoresis onto the AIS of the same neuron. Dashed lines indicate the interpolated E$_{GABA}$. Dark gray bars indicate duration of GABA iontophoresis ejection current.
D. Summary of E$_{GABA}$ measurements collected across homecage controls, water controls, and alcohol-access animals. Differences between treatment groups were non-significant.
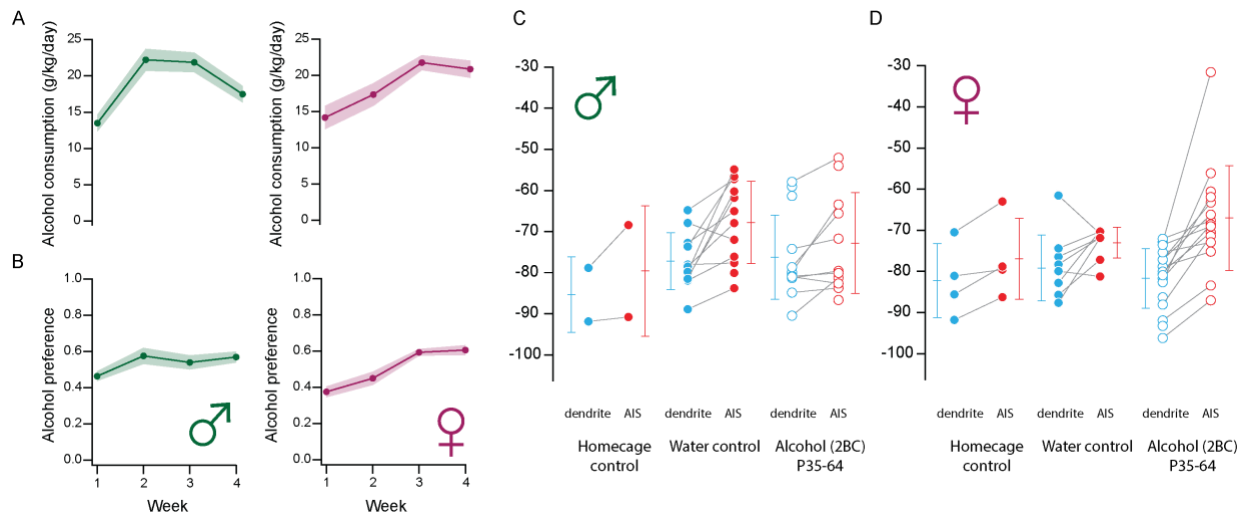
Figure 5.3 Lack of sex differences in E$_{GABA}$ changes at the AIS after adolescent alcohol consumption

A. Alcohol consumption in animals undergoing the two-bottle choice intermittent access to 20% alcohol paradigm split by sex (green: male, magenta: female).
B. Alcohol preference split by sex (colors as in A).
C. Summary of E$_{GABA}$ measurements collected across male homecage controls, water controls, and alcohol-access animals. Differences between treatment groups were non-significant.
D. Summary of E$_{GABA}$ measurements collected across female homecage controls, water controls, and alcohol-access animals. Differences between treatment groups were non-significant.
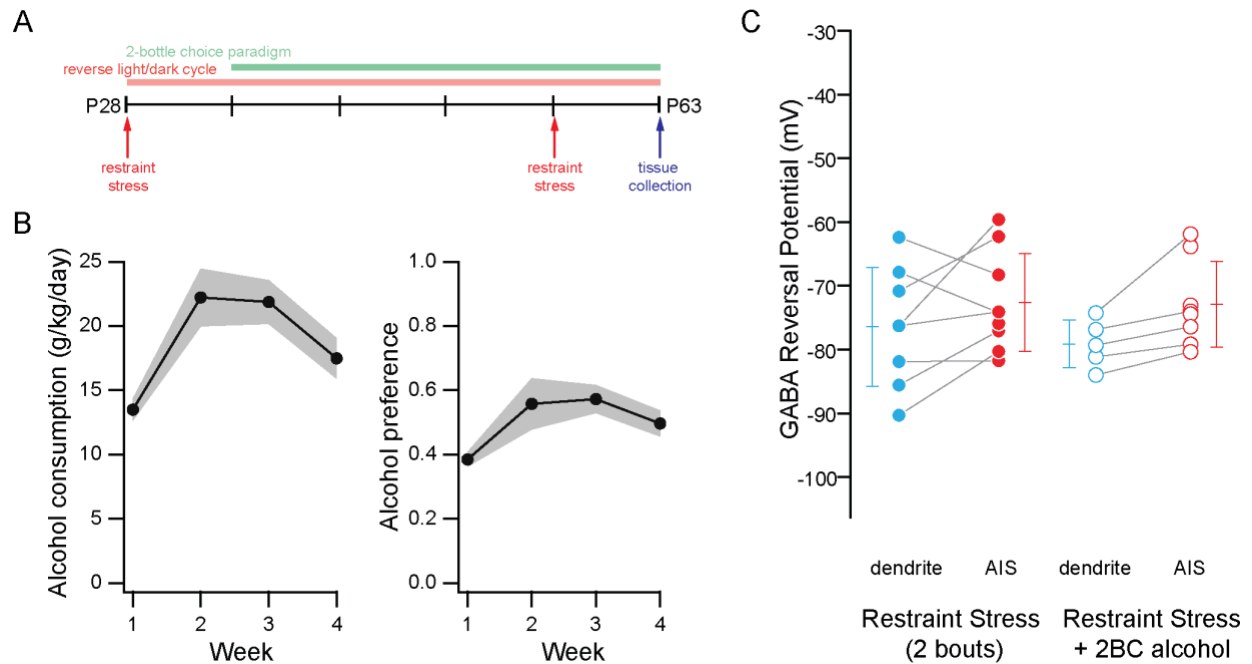
Figure 5.4 Stress does not alter E_GABA at the AIS

A. Timeline of two-bottle choice intermittent access to 20% alcohol paradigm with the addition of a restraint-stress protocol.
B. Alcohol consumption (left) and preference (right) after two-bottle choice and restraint-stress.
C. Summary of E_{GABA} measurements collected across restraint stress + water and restraint stress + alcohol animals. There was no significant difference between treatment groups.
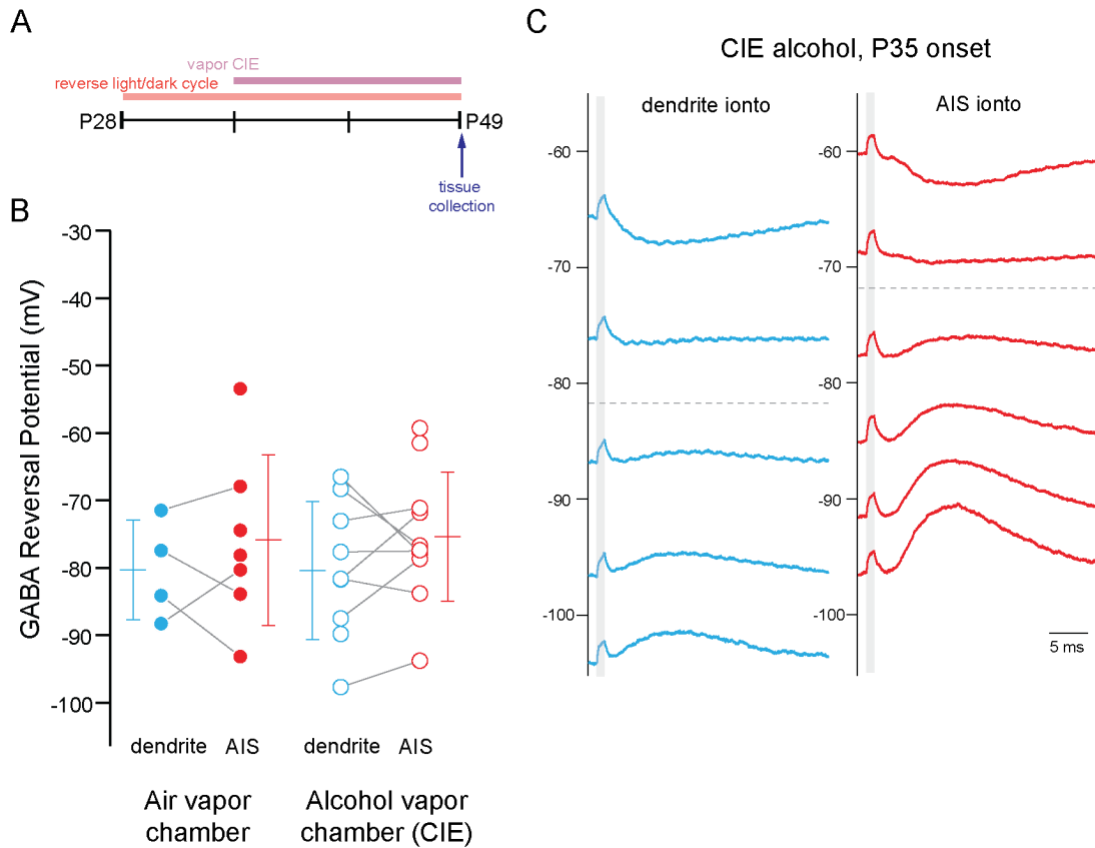
Figure 5.5 Chronic intermittent exposure to vapor alcohol does not alter E_{GABA} at the AIS

A. Timeline of chronic intermittent exposure to vaporized alcohol.
B. Summary of E_{GABA} measurements collected across air and alcohol vapor chamber animals. No significant differences existed between treatment groups.
C. Example reversal potentials from a dendrite (left, blue) and AIS (right, red) recorded from a neuron after CIE vapor treatment. Dashed gray lines represent interpolated EGABA. Dark gray bars indicate GABA iontophoresis current duration.

5.7 References

Alessi, D.R., Zhang, J., Khanna, A., Hochdörfer, T., Shang, Y., and Kahle, K.T. (2014). The WNK-SPAK / OSR1 pathway : Master regulator of cation-chloride cotransporters. Sci. Signal. *7*, 1–11.

Barak, S., Liu, F., Hamida, S. Ben, Yowell, Q. V, Neasta, J., Kharazia, V., Janak, P.H., and Ron, D. (2013). Disruption of alcohol-related memories by mTORC1 inhibition prevents relapse. Nat. Neurosci. *16*, 1111–1117.

Bechara, A., Dolan, S., Denburg, N., Hindes, A., Anderson, S.W., and Nathan, P.E. (2001). Decision-making deficits, linked to a dysfunctional ventromedial prefrontal cortex, revealed in alcohol and stimulant abusers. Neuropsychologia *39*, 376–389.

Becker, H.C., and Lopez, M.F. (2004). Increased ethanol drinking after repeated chronic ethanol exposure and withdrawal experience in C57BL/6 mice. Alcohol. Clin. Exp. Res. *28*, 1829–1838.

Bitzenhofer, S.H., Pöpplau, J.A., and Hanganu-Opatz, I.L. (2020). Gamma activity accelerates during prefrontal development.

Caballero, A., and Tseng, K.Y. (2016). GABAergic function as a limiting factor for prefrontal maturation during adolescence. Trends Neurosci. *39*, 441–448.

Carnicella, S., Ron, D., and Barak, S. (2014). Intermittent ethanol access schedule in rats as a preclinical model of alcohol abuse. Alcohol *48*, 243–252.

Cho, K.K.A., Hoch, R., Rubenstein, J.L.R., and Sohal, V.S. (2015). Gamma rhythms link prefrontal interneuron dysfunction with cognitive inflexibility in Dlx5/6+/- mice. Neuron *85*, 1332–1343.

Dewit, D.J., Adlaf, E.M., Offord, D.R., and Ogborne, A.C. (1991). Age at first alcohol use : A risk factor for the development of alcohol disorders. Am J Psychiatry 745–750.

Gogtay, N., Giedd, J.N., Lusk, L., Hayashi, K.M., Greenstein, D., Vaituzis, a C., Nugent, T.F., Herman, D.H., Clasen, L.S., Toga, A.W., et al. (2004). Dynamic mapping of human cortical development during childhood through early adulthood. Proc. Natl. Acad. Sci. U. S. A. *101*, 8174–8179.

Hwa, L.S., Chu, A., Levinson, S.A., Kayyali, T.M., Debold, J.F., and Miczek, K.A. (2011). Persistent escalation of alcohol drinking in C57BL/6J mice with intermittent access to 20% ethanol. Alcohol.

Clin. Exp. Res. *35*, 1938–1947.

Joffe, M.E., Winder, D.G., and Conn, P.J. (2020). Contrasting sex-dependent adaptations to synaptic physiology and membrane properties of prefrontal cortex interneuron subtypes in a mouse model of binge drinking.

Jury, N.J., DiBerto, J.F., Kash, T.L., and Holmes, A. (2001). Sex differences in the behavioral sequelae of chronic ethanol exposure.

Laguesse, S., Morisot, N., Phamluong, K., and Ron, D. (2016). Region specific activation of the AKT and mTORC1 pathway in response to excessive alcohol intake in rodents. Addict. Biol. *22*, 1856–1869.

Landi, M., Kreider, J., Lang, C., and Bullock, L. (1982). Effects of shipping on the immune function in mice. Am J Vet Res *43*, 1654–1657.

Nishida, H., Sohara, E., Nomura, N., Chiga, M., Alessi, D.R., and Rai, T. (2012). Phosphatidylinositol 3-Kinase/Akt signaling pathway activates the WNK-OSR1/SPAK-NCC phosphorylation cascade in hyperinsulinemic db / db mice. Hypertension 1–5.

Nixon, K., and Mcclain, J.A. (2010). Adolescence as a critical window for developing an alcohol use disorder : current findings in neuroscience. Curr. Opin. Psychiatry *23*, 0–5.

Olfe, J., Domanska, G., Schuett, C., and Kiank, C. (2010). Different stress-related phenotypes of BALB/c mice from in-house or vendor: alterations of the sympathetic and HPA axis responsiveness. BMC Physiol. *10*.

Ostroumov, A., Thomas, A.M., Kimmey, B.A., Karsch, J.S., Doyon, W.M., Dani, J.A., Ostroumov, A., Thomas, A.M., Kimmey, B.A., Karsch, J.S., et al. (2016). Stress Increases Ethanol Self-Administration via a Shift toward Excitatory GABA Signaling in the Ventral Tegmental Area. Neuron *92*, 493–504.

Padmanabhapillai, A., Porjesz, B., Ranganathan, M., Jones, K.A., Chorlian, D.B., Tang, Y., Kamarajan, C., Rangaswamy, M., Stimus, A., and Begleiter, H. (2006). Suppression of early evoked gamma band response in male alcoholics during a visual oddball task. Int. J. Psychophysiol. *60*, 15–26.

Rinetti-Vargas, G., Phamluong, K., Ron, D., and Bender, K.J. (2017). Periadolescent maturation of

GABAergic hyperpolarization at the axon initial segment. Cell Rep. *20*, 21–29.

Salling, M.C., Skelly, M.J., Avegno, E., Regan, S., Nichols, E., and Harrison, N.L. (2018). Alcohol consumption during adolescence in a mouse model of binge drinking alters the intrinsic excitability and function of the prefrontal cortex through a reduction in the hyperpolarization-activated cation current. J. Neurosci.

Sohal, V.S., Zhang, F., Yizhar, O., and Deisseroth, K. (2009). Parvalbumin neurons and gamma rhythms enhance cortical circuit performance. Nature *459*, 698–702.

Spear, L.P. (2011). Adolescent neurobehavioral characteristics, alcohol sensitivities, and intake: Setting the stage for alcohol use disorders? Child Dev Perspect *5*, 231–238.

Squeglia, L.M., Jacobus, J., and Tapert, S.F. (2014). The effect of alcohol use on human adolescent brain structures and systems (Elsevier B.V.).

Wallace, M.E. (1976). Effects of stress due to deprivation and transport in different genotypes of house mouse. Lab. Anim. *10*, 335–347.

Warnault, V., Darcq, E., Levine, A., Barak, S., and Ron, D. (2013). Chromatin remodeling — a novel strategy to control excessive alcohol drinking. Transl. Psychiatry 2013 32 *3*, e231–e231.

Witt, E.D. (2010). Research on alcohol and adolescent brain development : opportunities and future directions. Alcohol *44*, 119–124.

Publishing Agreement

It is the policy of the University to encourage open access and broad distribution of all theses, dissertations, and manuscripts. The Graduate Division will facilitate the distribution of UCSF theses, dissertations, and manuscripts to the UCSF Library for open access and distribution. UCSF will make such theses, dissertations, and manuscripts accessible to the public and will take reasonable steps to preserve these works in perpetuity.

I hereby grant the non-exclusive, perpetual right to The Regents of the University of California to reproduce, publicly display, distribute, preserve, and publish copies of my thesis, dissertation, or manuscript in any form or media, now existing or later derived, including access online for teaching, research, and public service purposes.

DocuSigned by:

Anna Lipkin

3413687848E44B2...   Author Signature

2/16/2023

Date